

THESE POUR OBTENIR LE GRADE DE DOCTEUR DE L'ÉCOLE NATIONALE SUPÉRIEURE DE CHIMIE DE MONTPELLIER

En Chimie et Physico-Chimie des Matériaux
École doctorale 459 – Sciences Chimiques Balard
Institut Charles Gerhardt de Montpellier (ICGM) – UMR5253

Modélisation Théorique Multi-échelle de Catalyseurs à Base de Pt et d'Au en Milieu Réactif

Multi-Scale Theoretical Modeling of Pt- and Au-Based Catalysts Under Reactive Media

Présentée par **Qing WANG** Le 25 octobre 2021, Sous la direction de **Didier TICHIT** et **Hazar GUESMI**

Devant le jury composé de

Dr. Anne HEMERYCK Chargée de Recherche CNRS, LAAS, UPR 8001, Toulouse, France	Rapportrice
Dr. Pr. Jinlan WANG Professeur, Southeast University, Nanjing, Chine	Rapportrice
Dr. François-Xavier COUDERT Directeur de Recherche CNRS, Chimie Paris Tech/ENSCP, France	Examineur
Dr. Tzonka MINEVA Directrice de Recherche CNRS, ICGM, ENSCM, Montpellier, France	Examinatrice (Présidente du jury)
Dr. Beien ZHU Associate Professor, Chinese Academy of Sciences, Shanghai, Chine	Examineur
M. Didier TICHIT Directeur de Recherche CNRS, ICGM, ENSCM, Montpellier, France	Directeur de thèse
Mme. Hazar GUESMI Chargée de Recherche CNRS, ICGM, ENSCM, Montpellier, France	Co-directrice



Acknowledgement

First, I would like to address my deep gratitude to my supervisors, Dr. Didier TICHIT and Dr. Hazar GUESMI, for accepting me as their PhD student and their overwhelming dedication and support during all along the 3 years of PhD.

Certainly, I would like to extend my appreciation to Dr. Frederik TIELENS from Vrije Universiteit Brussel and Dr. Beien ZHU from Chinese Academy of Sciences for their kind internship reception and their scientific advice.

Particularly, thanks to the periodic allocations via GENCI and the faithful collaborations with Dr. David Loffreda from ENS Lyon who has generously let us perform calculations on his in-house machines, we succeeded to run few hundred of picoseconds of AIMD simulations to explore the diverse configurations of our studied systems.

I would like also to address my sincere gratitude to my friends, colleagues: Jun, Sonia, Jonathan, Wassim, Ismail, Phouc, Kasia and Marco who shared with me the good and sometimes “hard” moments and offered me a lot of help in quotidian life and in work during the past 3 years, especially for this difficult period due to the COVID. I will never forget our “soirée”, “Girafe” and “sortie à la plage”...

Most importantly, I’m grateful for the support and unconditional love that my parents provide to me, without them I could never had this chance to come to France and experience the extraordinary 7-years of French life.

TABLE OF CONTENTS

RESUME DE LA THESE EN FRANÇAIS	1
--------------------------------------	---

GENERAL INTRODUCTION	1
----------------------------	---

CHAPTER I : THEORETICAL STUDIES OF TRANSITION-METAL CATALYSTS UNDER REACTIVE GAS CONDITIONS: STATE OF THE ART	6
--	----------

1. INTRODUCTION.....	6
2. MODELING MONOMETALLIC NANOPARTICLE (MNPs) CATALYSTS UNDER REACTIVE MEDIA	7
2.1 CONTEXT AND CURRENT KNOWLEDGE	7
2.2. DFT-BASED WULFF CONSTRUCTIONS	8
2.3 DFT-AIDED THERMODYNAMIC MODELING.....	9
2.4 <i>AB INITIO</i> MOLECULAR DYNAMICS (AIMD).....	12
3. MODELING ALLOY CATALYSTS UNDER REACTIVE MEDIA.....	13
3.1 CONTEXT AND CURRENT KNOWLEDGE	13
3.2 DFT APPROACH.....	14
3.3 DFT-AIDED THERMODYNAMIC MODELING	15
3.4 DFT-BASED CLUSTER EXPANSION (CE) METHOD.....	19
4. CONCLUSION AND PERSPECTIVE.....	21

CHAPTER II: THEORETICAL BACKGROUND	27
---	-----------

1. INTRODUCTION TO QUANTUM CHEMISTRY	27
1.1 HARTREE-FOCK METHOD	28
1.1.1 <i>Born-Oppenheimer approximation</i>	28
1.1.2 <i>Self-consistent field approximation</i>	30
2. DENSITY FUNCTIONAL THEORY METHODS	32
2.1 THOMAS-FERMI MODEL	32
2.2 HOHENBERG-KOHN THEOREMS.....	33

2.3	KOHN-SHAM METHOD.....	34
2.4	EXCHANGE-CORRELATION FUNCTIONALS	36
	2.4.1 <i>Local density approximation</i>	36
	2.4.2 <i>Generalized gradient approximation</i>	36
2.5	PROJECTOR AUGMENTED-WAVE METHOD	37
2.6	BRILLOUIN ZONE SAMPLING.....	37
2.7	DISPERSION CORRECTION.....	37
3.	MOLECULAR DYNAMICS SIMULATIONS	39
3.1	POTENTIALS IN <i>AB INITIO</i> METHODS.....	39
3.2	STATISTICAL MECHANICS.....	40
3.3	MODELING PROPERTIES.....	41
3.3.1	RADIAL DISTRIBUTION FUNCTION	41
3.3.2	PROBABILITY DISTRIBUTION FUNCTION RELATIVE TO CENTER OF MASS	43
4.	THERMODYNAMIC MODEL OF GAS ADSORPTION	43
5.	ENVIRONMENTAL CONSTRUCTION MODEL OF NANOPARTICLES	46
5.1	WULFF CONSTRUCTION UNDER VACUUM	46
5.2	CONSTRUCTION OF ENVIRONMENTAL NANOPARTICLE MODELS	47
5.3	AVERAGE SURFACE COORDINATION NUMBER	48
CHAPTER III: MODELING PT NANOPARTICLES UNDER HYDROGEN MEDIA.....		50
1.	INTRODUCTION.....	50
2.	METHODS AND COMPUTATIONAL DETAILS.....	51
2.1	MULTISCALE STRUCTURE RECONSTRUCTION (MSR) APPROACH	51
2.2	<i>AB INITIO</i> MOLECULAR DYNAMICS APPROACH.....	54
3.	RESULTS.....	56
3.1	MODELING EQUILIBRIUM SHAPE OF PT-NPs UNDER HYDROGEN CONDITION USING MSR MODEL	56
3.2	AIMD SIMULATION OF SMALL PT CLUSTERS IN PRESENCE OF HYDROGEN.....	62
	3.2.1 <i>Pt-NP under vacuum</i>	62
	3.2.2 <i>Pt-NP in presence of hydrogen</i>	65
4.	SUMMARY AND CONCLUSIONS	69
CHAPTER IV: MODELING SMALL AU NANOPARTICLES UNDER HYDROGEN MEDIA		76
1.	INTRODUCTION.....	76

2.	EXPERIMENTAL OBSERVATION	79
3.	THEORETICAL DETAILS	82
3.1	CLUSTER MODEL	82
3.2	AIMD SIMULATIONS AND DFT CALCULATIONS	82
4.	RESULTS AND DISCUSSION	83
4.1	AIMD SIMULATION OF AU NP UNDER VACUUM	83
4.2	AIMD SIMULATION OF AU NP IN PRESENCE OF HYDROGEN	87
4.2.1	<i>Hydrogenated Au-cluster simulation under 300 K</i>	88
4.2.2	<i>Hydrogenated Au-cluster simulation under 500 K</i>	92
5.	SUMMARY AND CONCLUSION	103
 CHAPTER V: MODELING PT BASED ALLOYS UNDER HYDROGEN MEDIA: FROM SINGLE ATOM TO HOST SURFACE		107
1.	INTRODUCTION.....	107
2.	COMPUTATIONAL DETAILS	109
3.	RESULTS AND DISCUSSIONS.....	114
3.A.	SINGLE-ATOM PT DILUTED IN M-HOST SURFACES.....	114
3.A.1	ENVIRONMENTAL SEGREGATION OF SINGLE-ATOM PT DILUTED IN M-HOST SURFACES	114
	<i>Single-atom Pt diluted in coinage group host-metal surfaces</i>	115
	<i>Single-atom Pt diluted in nickel group host-metal surfaces</i>	117
	<i>Single-atom Pt diluted in cobalt group host-metal surfaces</i>	120
3.A.2	BINDING HYDROGEN ENERGIES AND ELECTRONIC DENSITY OF STATES.....	123
3.A.3	SECTION SUMMARY	127
3.B.	SINGLE-ATOM M DILUTED IN PT-HOST SURFACES.....	129
3.B.1	SINGLE-ATOM M DILUTED IN PT-HOST SURFACES.....	129
	<i>M single atoms from coinage group diluted in Pt-host surfaces</i>	130
	<i>M single atoms from nickel group diluted in Pt-host surfaces</i>	132
	<i>M single atoms from cobalt group diluted in Pt-host surfaces</i>	133
3.B.2	BINDING HYDROGEN ENERGY	135
3.B.3	SECTION SUMMARY	137
4.	CONCLUSION	138
 SUMMARY AND GENERAL CONCLUSIONS		143
 SUPPORTING INFORMATION		146
	SI-CHAPTER III.....	146
	SI-III.1 ADSORPTION ENERGIES OF HYDROGEN ON DIFFERENT ADSORPTION SITES OF PT SURFACES.....	146

SI-III.2	FITTED ENTROPY PROFILE OF GAS-PHASE HYDROGEN (H ₂) AS A FUNCTION OF TEMPERATURE	147
SI-CHAPTER V	148
SI-V.1	LIST OF ALL DFT CALCULATED DATA APPLIED IN ENVIRONMENTAL SURFACE SEGREGATION MODEL 148	
SI-V.2	SCATTERS GRAPHS OF THE SEGREGATION TREND.....	151
SI-V.3	BINDING ENERGIES OF HYDROGEN ON PURE METALLIC SURFACES.....	153
SI-V.4	ENVIRONMENTAL SEGREGATION AND HYDROGEN COVERAGE EVOLUTIONS	155
SI-V.5	D-BAND CENTER ANALYSIS FOR DILUTE-Pt/M (1 1 1) BIMETALLIC ALLOYS	156
SI-V.6	D-BAND CENTER ANALYSIS FOR DILUTE-M/Pt(1 1 1) BIMETALLIC ALLOYS.....	157
SI-V.7	HYDROGEN BINDING ENERGIES ON ALLOYED SURFACES.....	157
LIST OF PUBLICATIONS	162

Résumé de la thèse

Dans le domaine de la catalyse hétérogène, les catalyseurs à base de métaux de transition (TMC), formés de nanoparticules monométalliques ou bimétalliques (nano-catalyseurs), suscitent un intérêt croissant grâce à leurs performances exceptionnelles dans de nombreuses réactions [1-2]. La conception rationnelle de ces catalyseurs repose sur une compréhension précise de leurs structures au niveau atomique et de leur mode d'intervention dans les processus catalytiques élémentaires. Dans ce contexte, la théorie de la fonctionnelle de la densité (DFT) est apparue comme une méthode de choix qui permet de déterminer avec précision les propriétés physicochimiques des matériaux, leur état de surface et de prédire la réactivité des sites actifs dans les mécanismes réactionnels [3-5]. Cependant, une des faiblesses de la DFT (et de même que les autres méthodes *ab-initio*) est qu'elle repose sur une analyse de la surface de l'énergie potentielle à 0 K, négligeant donc les effets entropiques des systèmes ainsi que la dynamique structurelle ou de forme. Ainsi, les travaux DFT, développés sur les nanocatalyseurs, se limitent souvent à des modèles cristallins de la surface ou à des clusters dont la structure est figée à 0 K.

Le développement expérimental des méthodes de caractérisations *in situ* et/ou *operando* des catalyseurs a apporté des preuves de changements subits par des catalyseurs dans les conditions de la réaction. En effet, certains TMC subissent des variations significatives de la structure, de la forme, et/ou de la composition de la surface sous conditions de gaz réactif [6-12]. Il se trouve que ces changements complexes ne sont pas décrits par une approche DFT classique. Ainsi, le développement de méthodes qui prennent en compte l'effet de l'environnement du catalyseur avec la précision à l'échelle quantique apportée par la DFT est fondamental. Cela, permet de comprendre et contrôler les modifications intervenant dans les catalyseurs en réponse à la

température et à la pression des réactifs gazeux et d'identifier la « vrai » structure de surface dont dépend la réactivité du TMC.

Dans cette thèse, nous nous concentrons sur deux problématiques importantes des nanoparticules de TMC évoluant sous atmosphère gazeuse :

(i) L'étude de la stabilité et de l'évolution de la structure des nanoparticules (NP) monométalliques. De nombreuses observations expérimentales *in situ* et/ou *operando* rapportent des changements structuraux drastiques de catalyseurs de type NP monométalliques exposés à des environnements gazeux réactifs [6-10]. Il est crucial de comprendre et de contrôler ces changements puisqu'il est maintenant bien établi que les propriétés catalytiques (activité et sélectivité) supérieures des NP monométalliques sont dépendantes de leur structure de la surface, leur taille et leur forme.

(ii) L'étude des systèmes bimétalliques, où une évolution de l'ordre chimique de la surface a été observée en présence de gaz. Elle est généralement induite par un phénomène de ségrégation inversée, c'est-à-dire l'enrichissement de la surface en l'un des composants. Ainsi, de nombreux résultats expérimentaux montrent que la composition chimique de la surface de certains catalyseurs bimétalliques en présence de gaz est très différente de celle observée sous vide ou obtenue avant réaction [11-14].

Pour répondre à ces deux problématiques, j'ai utilisé, au cours de cette thèse, différentes méthodes théoriques qui ont été choisies en fonction du système considéré. Pour étudier les changements de structure et de morphologie dans les NP monométalliques (Pt et Au) exposées à un gaz réactif (hydrogène), deux approches ont été développées :

(i) Un modèle thermodynamique basé sur la DFT et nommé modèle multi-échelle de reconstruction (MSR) [15]. Il combine les paramètres énergétiques issus de

la DFT avec une approche thermodynamique qui applique le théorème d'adsorption de Fowler-Guggenheim pour calculer l'évolution de l'énergie d'interface en fonction du recouvrement du gaz adsorbé. Ensuite, les constructions géométriques des NP sont effectuées en utilisant la méthode de construction de Wulff. Ce modèle MSR permet de prédire les changements des formes d'équilibre des NP monométalliques de grande taille (> 5 nm) dans différentes conditions de gaz réactif avec un coût raisonnable en ressources de calcul tout en gardant une précision suffisante.

- (ii) Une méthode exploratoire qui repose sur les simulations en dynamique moléculaire *ab initio* (AIMD), plus appropriée à l'étude de systèmes de plus petite taille que précédemment. Cette méthode peut fournir des descriptions de processus catalytiques complexes comme les transitions structurales, l'adsorption/désorption, et en particulier les phénomènes de formation et de rupture de liaisons chimiques, etc. à température finie. Plus précisément, grâce aux forces calculées « à la volée » à partir des structures électroniques, cette méthode permet d'accéder à la description de ces phénomènes alors que les méthodes de dynamiques moléculaires classiques, utilisant des champs de forces empiriques, ne le peuvent pas. Ainsi la méthode AIMD a permis d'étudier les changements structuraux et l'effet de l'adsorption de gaz sur des NP monométalliques (Pt et Au) de « petite taille » (contenant moins de quelques centaines d'atomes) évoluant sous hydrogène.

Pour étudier les systèmes d'alliages (plusieurs systèmes d'alliages à base de Pt dans des limites diluées), j'ai développé un modèle thermodynamique basé sur la DFT [16] nommé modèle de l'énergie de ségrégation environnementale (E_{eseg}). Ce modèle fournit une corrélation directe entre l'évolution de l'énergie de ségrégation de l'alliage bimétallique et de l'environnement

gazeux (T, P) dans lequel le système évolue. Comme pour le cas du modèle environnemental précédent où on calcule l'évolution de l'énergie d'interface en fonction du recouvrement, le modèle E_{eseg} permet de calculer l'évolution de l'énergie de ségrégation en fonction du recouvrement de gaz. Ainsi, les paramètres calculés par DFT sont couplés avec la thermodynamique. Ce modèle s'est avéré avantageux pour décrire le comportement d'un grand nombre de surfaces d'alliages et pour prédire le comportement de ségrégation dans des conditions réactives similaires à celles de l'expérience.

Mon manuscrit de thèse est constitué de cinq chapitres qui peuvent être brièvement résumés comme suit :

- Après une introduction générale, le chapitre 1, fournit un état de l'art sur les méthodologies théoriques qui existent dans la littérature et qui sont utilisées pour étudier les deux problématiques importantes mentionnés ci-dessus. Elles concernent l'évolution des nanoparticules de TMC dans des conditions de gaz réactif. Cela me permet de poser la première pierre et de donner le contexte des calculs théoriques que j'ai développé tout au long de la thèse.

-Le chapitre 2 présente une brève description des différents principes théoriques sur lesquels reposent les approches employées dans cette thèse. Ensuite, dans les chapitres 3, 4 et 5 les différentes TMC étudiées sont présentées, et les résultats obtenus sont détaillés et discutés.

- Ainsi, le chapitre 3 est dédié à l'étude des changements de morphologie subis par les nanoparticules de Pt en interaction avec des atomes d'hydrogène. Deux tailles différentes de NP sont considérées sous température et pression d'hydrogène. Pour étudier les NP de Pt de taille supérieure à 5 nm, le modèle MSR a été utilisé alors que pour les NP d'une taille d'environ $\sim 1,8$ nm les simulations AIMD ont été choisies. Comme cela sera détaillé dans ce chapitre, les résultats thermodynamiques montrent des changements évidents de la morphologie d'équilibre

pour les NP de Pt de grande taille en fonction de la température et la pression. A l'inverse, la simulation AIMD à 500 K de petites NP de Pt recouvertes d'adsorbats d'hydrogène ne révèle aucun changement structural. Ces résultats sont discutés en analysant l'adsorption d'hydrogène sur Pt et la structure électronique du système.

- Au chapitre 4, comme pour le cas des petites NP de Pt, la simulation AIMD est développée pour étudier des petites NP d'or monométalliques, également recouvertes d'hydrogène. Fait intéressant, malgré la plus faible énergie d'adsorption de l'hydrogène sur Au que sur Pt, les simulations AIMD prédisent un changement morphologique drastique pour les NP de Au, contrairement au NP de Pt. Grâce à une collaboration avec des collègues expérimentateurs, fournissant des observations de microscopie environnementale, cette étude nous a permis de révéler une transformation structurale dépendante de la taille des NP d'or exposées à l'hydrogène atmosphérique.

- Le chapitre 5 présente les travaux sur les systèmes d'alliages à base de Pt. Les deux états dilués de ces systèmes alliés ont été étudiés : les alliages dilués-Pt/M, où le Pt est considéré comme un atome isolé dilué dans 8 surfaces sélectionnées de métaux de transition (M) (M = Cu, Ag, Au, Ni, Pd, Co, Rh, Ir); et les alliages dilués-M/Pt, où le Pt est considéré comme surface hôte où des atomes isolés M sont dilués. Pour ces systèmes catalytiques, l'évolution du comportement de la ségrégation de M dans Pt et de Pt dans M, ainsi que la stabilité de l'atome isolé sous différentes températures et pressions d'hydrogène sont étudiées. Les résultats montrent des comportements non intuitifs où l'élément qui ségrége n'est pas systématiquement celui qui présente la plus forte affinité avec l'adsorbat gazeux. Une analyse approfondie des énergies de liaison et des effets électroniques régissant la stabilité de ces systèmes d'alliage à un seul atome est présentée.

Enfin, une conclusion générale rappelle tous les résultats clés discutés tout au long de ce travail, suivie par plusieurs annexes fournissant plus de détails concernant les différents calculs obtenus.

Références

1. Rolison, D. R., Catalytic Nanoarchitectures--the Importance of Nothing and the Unimportance of Periodicity. *Science* **2003**, *299*, 1698-1701.
2. Liu, L.; Corma, A., Metal Catalysts for Heterogeneous Catalysis: From Single Atoms to Nanoclusters and Nanoparticles. *Chemical Reviews* **2018**, *118*, 4981-5079.
3. Kurth, S.; Marques, M. A. L.; Gross, E. K. U., Density-Functional Theory. In *Encyclopedia of Condensed Matter Physics*, Bassani, F.; Liedl, G. L.; Wyder, P., Eds. Elsevier: Oxford, 2005; pp 395-402.
4. Norskov, J. K.; Abild-Pedersen, F.; Studt, F.; Bligaard, T., Density Functional Theory in Surface Chemistry and Catalysis. *PNAS* **2011**, *108*, 937-943.
5. Neugebauer, J.; Hickel, T., Density Functional Theory in Materials Science. *Wiley Interdiscip Rev Comput Mol Sci* **2013**, *3*, 438-448.
6. Mistry, H.; Behafarid, F.; Zhou, E.; Ono, L. K.; Zhang, L.; Roldan Cuenya, B., Shape-Dependent Catalytic Oxidation of 2-Butanol over Pt Nanoparticles Supported on Γ -Al₂O₃. *ACS Catalysis* **2014**, *4*, 109-115.
7. Fernandez, S., et al., In Situ Structural Evolution of Single Particle Model Catalysts under Ambient Pressure Reaction Conditions. *Nanoscale* **2018**, *11*, 331-338.
8. Liu, L.; Zakharov, D. N.; Arenal, R.; Concepcion, P.; Stach, E. A.; Corma, A., Evolution and Stabilization of Subnanometric Metal Species in Confined Space by in Situ TEM. *Nature Communications* **2018**, *9*, 574.
9. Bergmann, A.; Roldan Cuenya, B., Operando Insights into Nanoparticle Transformations During Catalysis. *ACS Catalysis* **2019**, *9*, 10020-10043.
10. He, Y.; Liu, J. C.; Luo, L.; Wang, Y. G.; Zhu, J.; Du, Y.; Li, J.; Mao, S. X.; Wang, C., Size-Dependent Dynamic Structures of Supported Gold Nanoparticles in CO Oxidation Reaction Condition. *PNAS* **2018**, *115*, 7700-7705.
11. Lee, S.-Y., et al., Surface-Rearranged Pd₃Au/C Nanocatalysts by Using CO-Induced Segregation for Formic Acid Oxidation Reactions. *ACS Catalysis* **2014**, *4*, 2402-2408.
12. Ahmadi, M.; Behafarid, F.; Cui, C.; Strasser, P.; Cuenya, B. R., Long-Range Segregation Phenomena in Shape-Selected Bimetallic Nanoparticles: Chemical State Effects. *ACS Nano* **2013**, *7*, 9195-9204.
13. Tao, F.; Grass, M. E.; Zhang, Y.; Butcher, D. R.; Renzas, J. R.; Liu, Z.; Chung, J. Y.; Mun, B. S.; Salmeron, M.; Somorjai, G. A., Reaction-Driven Restructuring of Rh-Pd and Pt-Pd Core-Shell Nanoparticles. *Science* **2008**, *322*, 932-934.
14. Mu, R. T.; Guo, X. G.; Fu, Q.; Bao, X. H., Oscillation of Surface Structure and Reactivity of PtNi Bimetallic Catalysts with Redox Treatments at Variable Temperatures. *The Journal of Physical Chemistry C* **2011**, *115*, 20590-20595.
15. Zhu, B.; Meng, J.; Gao, Y., Equilibrium Shape of Metal Nanoparticles under Reactive Gas Conditions. *The Journal of Physical Chemistry C* **2017**, *121*, 5629-5634.
16. Meng, J.; Zhu, B. E.; Gao, Y., Surface Composition Evolution of Bimetallic Alloys under Reaction Conditions. *The Journal of Physical Chemistry C* **2019**, *123*, 28241-28247.

General introduction

In the field of heterogeneous catalysis, transition-metal catalysts (TMC) synthesized in the form of monometallic or alloyed nanoparticles have attracted great interest as they have been shown to be powerful for many important applications [1-2]. From general point of view, the key to the rational design of TMC relies on an atomic-level understanding of catalytic materials and the elementary catalytic processes under realistic conditions. Thereto, density functional theory (DFT) has emerged as an accurate method and has been largely applied to provide experimental guidance and fundamental insights in catalytic reaction mechanisms [3-5]. Since its formulation, DFT method involves calculations of a potential energy surface at 0 K, which provides the “total energy” and the ground state electronic structure of the system. This is referred as zero-temperature method where investigations in heterogeneous catalysis are generally performed on “static” crystal or surface models with minimum number of molecular adsorbates at 0 K. However, recent experimental development has provided more and more evidence about the dynamic nature of catalysts under *in situ* and/or *operando* conditions, among which the TMC are found undergoing constant changes in structures, shapes, surface compositions under reactive gas conditions [6-12]. Obviously, such complex changes cannot be captured by classical DFT approaches, thus moving from 0 K to *operando* models is of great importance for understanding how the structure of catalysts change in response to temperature and reactive gas pressure under working conditions, on which the reactivity of TMC will eventually depend.

In this thesis, we focus on two important issues of TMC nanoparticles evolving under reactive gas condition:

- (i) The first one concerns the study of the stability and the structure evolutions of monometallic nanoparticles (MNP). It is now well established that the catalytic

activity and unique selectivity of MNP are generally surface structure-, size- and shape-dependent. The forecast is the increasing number of recent *in situ* and *operando* experimental observations reporting drastic shape changes of MNP catalysts in several reactive gas environments [6-10].

- (ii) The second issue concerns the evolution of the chemical ordering in alloy systems induced by reversed segregation phenomenon, i.e., the enrichment of one of the components on the surface or bulk of alloys and nanoalloys in presence of reactive gas. Many experimental findings indicate that the presence of adsorbates induce segregation behaviors that are different from the predicted ones under vacuum [13-14]. Moreover, the segregation trends of some alloys can be tuned either in favor of its initial surface/bulk segregation tendency or suppress and even inverted in response to certain specific temperature and gas pressure conditions [11-12].

To address these two issues, I used different theoretical methods, which were chosen depending on the targeted system. To study the structure and morphology changes in MNPs (Pt and Au NPs) exposed to reactive gas (hydrogen), two approaches were developed. The first one is a DFT-based thermodynamic model named multiscale structure reconstruction model (MSR) [15], which combines the energetic parameters issued from DFT with thermodynamics through Fowler-Guggenheim adsorption theorem to calculate the interfacial energy of surfaces interacting with adsorbed gas. Then geometric constructions of the Pt-NPs are obtained using Wulff construction method. This MSR model allows predicting the changes of equilibrium shapes of large sized MNPs (> 5 nm) under different reactive gas conditions with reasonable cost in computational resources while keeping sufficient accuracy. The second approach is the *ab initio* molecular dynamic (AIMD) method, which is more appropriate for smaller sized systems. This method can provide descriptions of complex catalytic processes like the structural transition, adsorption/desorption, and particularly the chemical bond forming/breaking, etc.

under finite-temperature in an accurate way thanks to the forces computed “on the fly” from electronic structure calculations. This cannot be achieved with other classical MDs using empirical force field. The AIMD was thus selected to investigate structural changes and adsorption effects on MNPs with “small size” (containing less than a few hundreds of atoms) under reactive gas media.

To study the alloyed systems (several Pt-based alloy systems in diluted limits), I employed a DFT-based thermodynamic model [16] named as environmental segregation energy (E_{eseg}) model which provides a direct correlation between the segregation energy evolution of bimetallic alloys and their environmental gas (T, P)-condition, wherein the DFT-calculated parameters are coupled with thermodynamics. This model is found to be advantageous to screen and investigate a large number of alloy surfaces and to identify the segregation behaviors in reactive conditions similar to the experimental ones.

The manuscript is built on five chapters that can be briefly summarized as follows: **Chapter 1** provides a state of the art on the theoretical methodologies that exist in the literature and are used to investigate the above-mentioned two important issues of TMC nanoparticles evolving under reactive gas conditions. This allows me to lay the foundation stone and to give the context of the theoretical approaches that I performed throughout the thesis. **Chapter 2** presents brief descriptions of all the theoretical principles employed in this thesis. Then, in Chapters 3, 4 and 5 the different studied TMCs are presented, and the obtained results are detailed and discussed. **Chapter 3** is dedicated to the study of the morphology changes of Pt nanoparticle (Pt-NP) under hydrogen media. Two different sizes of Pt-NP are considered for which the MSR model was employed to study the Pt-NP of size bigger than 5 nm and AIMD simulations for NP with size of about ~1.8 nm. As it will be detailed, while the MSR model predicts changes in the equilibrium morphology for bigger sized Pt-NPs under varied temperature and hydrogen

pressure, the AIMD simulation reveals no structural changes during simulations at 500 K of small Pt-NP covered by hydrogen adsorbates. These results are discussed by analyzing the adsorption of hydrogen on Pt and the electronic structure of the system. In **Chapter 4**, like for the case of small Pt-NP, the AIMD simulation is performed to study small monometallic gold NPs, also covered by hydrogen. Interestingly, despite the weaker adsorption energy of hydrogen on Au compared to Pt, AIMD simulations predict strong morphological changes for Au-NP, in contrast with Pt-NP. Thanks to a through collaboration with colleagues performing experimentations, particularly environmental microscopy observations, this study allowed us to reveal size-dependent structural transformation of Au-NPs exposed to hydrogen atmosphere. **Chapter 5** presents the investigations related to the Pt-based alloy systems. Two diluted states of these alloyed systems were investigated: the named “dilute-Pt/M alloys”, where the Pt is considered as a single-atom diluted in 8 selected transition metal (M) surfaces (M = Cu, Ag, Au, Ni, Pd, Co, Rh, Ir); and the named “dilute-M/Pt alloys”, where the Pt is considered as host surface of M single-atoms. For these catalytic systems, the evolution of segregation behavior and the stability of single atom alloy under various temperatures (T) and hydrogen gas pressures (P) are studied. The results show no intuitive behaviors. Indeed the segregating component does not systematically present the stronger affinity with the gas adsorbates. A profound analysis of the mechanistic and the electronic effects governing the stability of these single atom alloy systems are presented.

Finally, a general conclusion reminds all the key results discussed all along this work, followed by several annexes providing more details concerning the different obtained calculations.

Reference

1. Rolison, D. R., Catalytic Nanoarchitectures--the Importance of Nothing and the Unimportance of Periodicity. *Science* **2003**, *299*, 1698-1701.
2. Liu, L.; Corma, A., Metal Catalysts for Heterogeneous Catalysis: From Single Atoms to Nanoclusters and Nanoparticles. *Chemical Reviews* **2018**, *118*, 4981-5079.
3. Kurth, S.; Marques, M. A. L.; Gross, E. K. U., Density-Functional Theory. In *Encyclopedia of Condensed Matter Physics*, Bassani, F.; Liedl, G. L.; Wyder, P., Eds. Elsevier: Oxford, 2005; pp 395-402.
4. Norskov, J. K.; Abild-Pedersen, F.; Studt, F.; Bligaard, T., Density Functional Theory in Surface Chemistry and Catalysis. *PNAS* **2011**, *108*, 937-943.
5. Neugebauer, J.; Hickel, T., Density Functional Theory in Materials Science. *Wiley Interdiscip Rev Comput Mol Sci* **2013**, *3*, 438-448.
6. Mistry, H.; Behafarid, F.; Zhou, E.; Ono, L. K.; Zhang, L.; Roldan Cuenya, B., Shape-Dependent Catalytic Oxidation of 2-Butanol over Pt Nanoparticles Supported on γ -Al₂O₃. *ACS Catalysis* **2014**, *4*, 109-115.
7. Fernandez, S., et al., In Situ Structural Evolution of Single Particle Model Catalysts under Ambient Pressure Reaction Conditions. *Nanoscale* **2018**, *11*, 331-338.
8. Liu, L.; Zakharov, D. N.; Arenal, R.; Concepcion, P.; Stach, E. A.; Corma, A., Evolution and Stabilization of Subnanometric Metal Species in Confined Space by in Situ TEM. *Nature Communications* **2018**, *9*, 574.
9. Bergmann, A.; Roldan Cuenya, B., Operando Insights into Nanoparticle Transformations During Catalysis. *ACS Catalysis* **2019**, *9*, 10020-10043.
10. He, Y.; Liu, J. C.; Luo, L.; Wang, Y. G.; Zhu, J.; Du, Y.; Li, J.; Mao, S. X.; Wang, C., Size-Dependent Dynamic Structures of Supported Gold Nanoparticles in CO Oxidation Reaction Condition. *PNAS* **2018**, *115*, 7700-7705.
11. Lee, S.-Y., et al., Surface-Rearranged Pd₃Au/C Nanocatalysts by Using CO-Induced Segregation for Formic Acid Oxidation Reactions. *ACS Catalysis* **2014**, *4*, 2402-2408.
12. Ahmadi, M.; Behafarid, F.; Cui, C.; Strasser, P.; Cuenya, B. R., Long-Range Segregation Phenomena in Shape-Selected Bimetallic Nanoparticles: Chemical State Effects. *ACS Nano* **2013**, *7*, 9195-9204.
13. Tao, F.; Grass, M. E.; Zhang, Y.; Butcher, D. R.; Renzas, J. R.; Liu, Z.; Chung, J. Y.; Mun, B. S.; Salmeron, M.; Somorjai, G. A., Reaction-Driven Restructuring of Rh-Pd and Pt-Pd Core-Shell Nanoparticles. *Science* **2008**, *322*, 932-934.
14. Mu, R. T.; Guo, X. G.; Fu, Q.; Bao, X. H., Oscillation of Surface Structure and Reactivity of PtNi Bimetallic Catalysts with Redox Treatments at Variable Temperatures. *The Journal of Physical Chemistry C* **2011**, *115*, 20590-20595.
15. Zhu, B.; Meng, J.; Gao, Y., Equilibrium Shape of Metal Nanoparticles under Reactive Gas Conditions. *The Journal of Physical Chemistry C* **2017**, *121*, 5629-5634.
16. Meng, J.; Zhu, B. E.; Gao, Y., Surface Composition Evolution of Bimetallic Alloys under Reaction Conditions. *The Journal of Physical Chemistry C* **2019**, *123*, 28241-28247.

Chapter I

Theoretical studies of transition-metal catalysts under reactive gas conditions: state of the art

1. Introduction

During the last decades, several theoretical methodologies and approaches have been applied to understand the interaction of solid catalysts with reactive gas molecules and the impact of these latter's on the catalytic properties of the targeted materials [1-9]. Among these methods, density functional theory (DFT) stands as the most matured and widely applied theoretical approach in heterogeneous catalysis [10]. DFT method provides “accurate enough” information on the electronic structures and the “total energy” of systems, which referring to the search or to the identification of potential energy surface (PES) of a given system at 0 K. However, the recent development in experimental instrumentations as the *in situ* microscopy observations provide numerous evidence [11-13] of the dynamic nature of the catalysts under the reaction condition. Indeed, generated by the impact of temperature and pressure, the mobility of the atoms and molecules induces structural reconstructions and stability changes of the nanocatalytic materials. These transformations occurring under working conditions affect the activity and the selectivity as well as the lifetime of the catalysts. Thus, nowadays the theoretical investigations face an urgent need of development to extend the classical 0 K models to more realistic *operando* models aiming to bridge the so-called pressure gap [14].

This chapter aims to present a short overview of the theoretical methodologies used to investigate TMC nanoparticles evolving under realistic reactive gas conditions. The first focus concerns in the studies devoted to the modeling of monometallic nanoparticles, then the problem of alloy systems will be addressed. Thus, after a quick review of the commonly used standard-DFT method for investigating extended TM surfaces under vacuum or in presence of adsorbed isolated molecules at 0 K, a state-of-the-art development of the most commonly developed DFT approaches on *operando* theoretical modeling, including (i) *ab initio* molecular dynamics, (ii) DFT-based cluster expansion method, and (iii) DFT-aided thermodynamic modeling are presented. The purpose of this chapter is not to provide lecture on the fundamental principle of these methods, but to present their applications within some relevant examples and to discuss their limitations. It is the way that I choose to introduce how, my work within this thesis, may bring new acknowledges for investigating these two important issues by employing strategies that should be more “adequate” for describing more “realistic” systems. It will be addressed that based on the complexity of the catalytic process: size, structure, surface composition, gas environment, temperature and pressures, etc., certain approaches are more advantageous than others and combinations of several different approaches may be needed for adapting a specific system.

2. Modeling monometallic nanoparticle (MNPs) catalysts under reactive media

2.1 Context and current knowledge

Monometallic nanoparticle (MNPs) catalysts generated increasing interest due to their high specific surface active sites and particular properties, which lead to optimal performances in many catalytic reactions [15-17]. It is commonly accepted that the specific functionality of

MNPs is intimately related to their stability on the support, their specific size [18-21] and structure [22-23]. Moreover, as emphasized earlier, some recent *in situ* experimental observations have shown that MNPs may undergo structure and shape evolutions under reactive gas conditions. As for example, using the *in situ* environmental transmission electron microscopy (ETEM), the recent work of Yoshida *et al.* [24], reported that the initially stable high-faceted Pt nanoparticles (~3.6 nm) under vacuum became round when exposed to 1 mbar of CO/air at room temperature. In contrast, when the temperature is elevated to 373.15 K, the NPs reshape as partially faceted. This significant CO-induced, temperature-dependent surface restructuring of Pt-NPs leads to changes in the properties of the catalyst. Similarly, time-resolved environmental TEM observations reported by Vendelbo *et al.* [25] show dynamic refaceting of Pt-NPs during the oscillatory CO oxidation reaction at 727 K. In this work, the authors found that the Pt-NPs switch between a more spherical shape and a more faceted morphology during increasing/reducing of CO conversions. These *in situ* observed adsorbate-induced nanoparticle reshaping behaviors show how it is crucial the knowledge of the realistic catalyst surface during working conditions because its catalytic properties are dependent.

2.2. DFT-based Wulff constructions

During the last decade, many theoretical approaches have been applied/developed to predict the shape evolution of nanocatalysts under temperature and pressure. Among all, the DFT-based calculations combined with Wulff construction model [26] have been routinely employed [2, 4, 27-29]. This approach consists of predicting the shape of metallic or oxide NPs under vacuum by calculating the minimum surface energy of several low and high index surface planes that may possibly constitute the larger sized NPs (more details of Wulff construction are provided in **Chapter 2**). In order to account for the presence of adsorbed gas, it is common to compare the binding energies of reactive gas on the different surface planes and to extrapolate this to the

surface energies. For instance, to study the equilibrium shape of gold NPs in presence of CO gas, Barmparis *et al.* [2] used standard DFT to calculate the adsorption energies of single-adsorbed CO on Au(*hkl*) surface models (with $h, k, l \leq 3$), then those values are used to relate with the surface tension values calculated for Au(*hkl*) surface under vacuum leading to a CO revised-surface tension, i.e., interface tension (see **Chapter 2** for the definition). By this way the equilibrium shapes of CO-covered Au-NPs were constructed with the aid of the Wulff model. Using this method, the authors reported that, under vacuum, Au-NPs of size smaller than 16.3 nm are in truncated octahedral shape consisting of mainly (1 1 1) and (1 0 0) surfaces, while bigger NPs, show major (3 3 2) faceting. In contrast, when exposed to CO, the equilibrium shape of Au-NPs are found spherical compared to the ones under vacuum.

It is obvious that this described Wulff construction modeling based on DFT calculations of single atom gas and at 0 K allows to predict the structure of large-scale NPs that are outreach of direct DFT screening. However, this method suffers from what we named above as “static picture” since it only provides predictions of NP shapes based on the calculations of surface tensions and interface tensions at 0 K with very low coverage of adsorbed gas and without any account for the entropy terms, which is far from the experimental conditions.

2.3 DFT-aided thermodynamic modeling

Improvement of the previously described approach can be made using the DFT-aided thermodynamic modeling that accounts for the effects of temperature and gas pressure. The general idea of this approach is to couple the DFT calculated energetic parameters of specific systems (the metal-phase and the molecules from the gas-phase) with appropriate thermodynamic terms, such as the Gibbs free energy [30], by which the thermodynamically most stable configuration of systems is identified as the one that possesses the lowest interface energy at given temperature T and gas pressure P . For example, to predict the equilibrium

surface morphology of iron nanoparticles (Fe-NPs) under different temperature and hydrogen partial pressure, Xu and co-workers [31] firstly carried out systematic DFT calculations of the hydrogen adsorption energies on the most stable sites of seven iron surfaces, which are the (1 0 0), (1 1 0), (1 1 1), (2 1 0), (2 1 1), (3 1 0) and (3 2 1) (as depicted in **Figure I.1-A**) with hydrogen coverage from 0 to saturation. Then the Gibbs free energies of iron surfaces and the chemical potentials of the hydrogen were calculated to predict the evolution of interface energies of iron surfaces with different H-coverage under varied temperature and hydrogen partial pressure. By that way, the equilibrium shapes of Fe-NPs with the most thermostable hydrogen adsorption coverage were predicted and constructed using the Wulff construction model. As represented in **Figure I.1-B**, the stable H-coverage as a function of temperature and hydrogen partial pressure on the Fe(1 1 1) surface was obtained showing that the stable hydrogen coverage decreases from 23 H to 0 H with increasing T and/or decreasing P . And the authors also found that the equilibrium shapes of Fe-NPs under one atmosphere of hydrogen pressure (**Figure I.1-C**) are dominated with (1 1 0) surface at 0 K, while at 425 K, the (3 1 0) surface starts to expose apart from the (1 1 0) surface, then with temperature increasing to 675 K, the (3 1 0) surface increases more, nevertheless the (1 1 0) surface still dominates. These predicted morphology of iron particles are found in agreement with the TEM analysis [32] on the H₂ reduced Fe-NPs under 673 K, wherein the surface proportions of (3 1 0) to (1 1 0) increased after H₂ reduction.

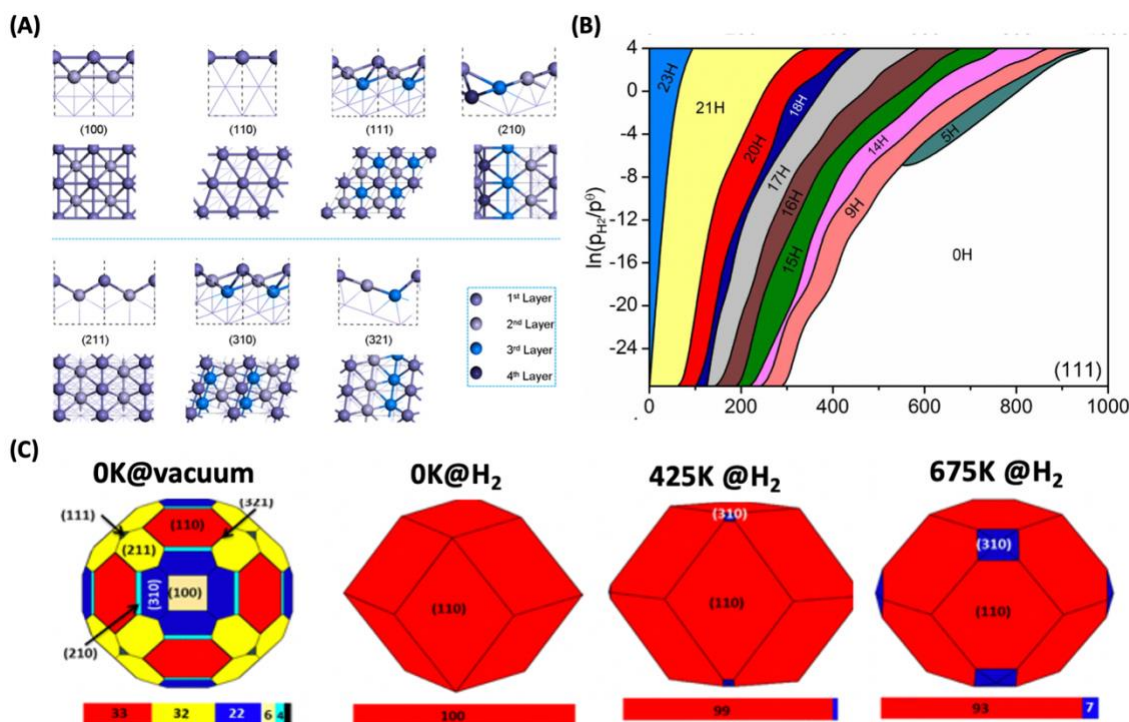


Figure I.1]. Illustration of DFT-aided thermodynamic method applied in hydrogen-Fe catalytic system. (A) Schematic side and top views of seven iron surfaces. (B) Equilibrium phase diagram of H coverage on the (111) surface (C) Wulff shapes of clean iron particles at 0 K under vacuum, and iron particles under one atmosphere of hydrogen pressure at 0 K, 425 K, and 675 K. Figure adapted with permission from [31]. Copyright 2014 American Chemical Society

This method offers a low-cost but enough accurate way to move from 0 K modeling to *operando* (T , P)-conditions for the prediction of equilibrium shapes of metal nanoparticles in reactive gas conditions. This method has proven also quite successful in the studies of the thermal stability [33-38] and surface phase-transition [39-42] of various catalysts (nanoparticles, alloys and surfaces) in reaction condition. However, the main inconvenience of this approach is that its accuracy directly relies on the completeness of the number of adsorption configurations considered. Very recently, Zhu *et al.* [37] proposed an extension of this approach by including the thermodynamic term called Fowler-Guggenheim (F-G) in which the lateral interaction between adsorbates are implicitly accounted for by identifying the number of first-neighboring adsorption sites of each considered surface orientation. Thus, this method, compared to the previous ones, provides a simplified way to estimate the lateral interaction without the necessity

to explicitly create and scan numerous adsorption configuration models. This method has been successfully applied for predicting the equilibrium shapes of MNPs (Cu, Ag, Au, Pt and Pd) under reactive carbon monoxide gas (T, P)-conditions [37]. Although the results obtained using both methods have shown their accuracy in predicting such MNPs under reactive gas condition, the validity using such models is related to the use of Wulff construction which is limited to NPs with “big-sizes” (> 5 nm) since the nanoparticles are constructed using energetic information calculated from extended surface slab models. Therefore, alternative approaches with sufficient accuracy for the investigation of “small-size” MNPs should be selected.

2.4 *Ab initio* molecular dynamics (AIMD)

For small sized MNPs, or alloyed ones elsewhere, containing less than several dozens of atoms, it is logically feasible to scan the stability of several configurations of NP with different gas coverages using DFT energy optimizations. However, this strategy remains unsatisfactory as the selected configurational space remains very constrained compared to the realistic one. A better alternative is to use *ab initio* molecular dynamics (AIMD), especially when it comes to a system with few hundred atoms. In addition, for nanoparticles exposed to reactive media, complex dynamic processes may involve unexpected configurations and transition states that the previous relatively simplistic DFT and DFT-aided thermodynamic modeling approaches are unable to predict. Moreover, AIMD has been shown to be efficient for exploring the conformational three-dimensional complexity of metal NPs in presence of gas adsorbates, which provides dynamic trajectories that links different possible structural changes induced by adsorbates. For instance, to study the structural changes of Au-NPs when exposed to a gas mixture of CO + O₂ under room temperature evidenced by the *in situ* aberration-corrected environmental transmission electron microscopy images, He *et al.* [43] performed AIMD simulations on Au cluster of 19 atoms supported on CeO₂(1 1 1) surface and interacting with

12 CO molecules. Their AIMD simulations performed at 300 K show that the Au₁₉-clusters lost its flat-hexagonal configuration due to the formation of Au-CO bonds that extract the Au atoms out of its original positions and transformed into a 3D cluster. Contrarily, in absence of CO molecules, the Au₁₉-cluster keep its flat-hexagonal configuration under same simulation conditions (300 K).

Although more detailed and precise catalytic properties are expected from AIMD, it is computationally more costly compared to the DFT-based thermodynamic method. And the direct AIMD simulations for long timescales in order to capture the full free energy landscape of realistic catalytic processes are challenging, thus it's more often applied in "small-sized" systems containing less than a few hundred number of atoms.

3. Modeling alloy catalysts under reactive media

3.1 Context and current knowledge

Alloy catalysts are emerging materials that show high performances thanks to the synergistic effects created when combining two different metals. The addition of a second metal induces the change of the surface composition of alloys due to the surface energy competition between two metals, therein the metal with lower/higher surface energy tends to segregate to the surface/bulk of the formed alloys. In addition, the mixing energy, related to the cohesive energy of each component, also plays a role in the ordering tendency of the alloy system either formed in hetero-atomic (i.e., ordered/disordered mixed structures) or in homo-atomic (i.e., core-shell structures) bonds. Other factors as the atomic size of the components leading to elastic strains and electronic structure changes determine the equilibrium structure of the alloyed materials [44].

Extensive theoretical works using either semi-empirical [45-47] or DFT methods [48-49] have been dedicated to predict the segregation phenomena of nanoalloys under vacuum. However, the problem is that many recent experimental findings are providing hard evidence of atomic ordering changes induced by segregation of alloy atoms in response to certain reactive gas (T , P)-conditions. For instance, Zhu *et al.* [50] reported that the DFT calculated results in bimetallic AuPd nanoparticles showed evidence of Pd surface enrichment where both Pd monomers and Pd dimers could exist in presence of adsorbed CO compared to vacuum condition. Moreover, the energetic stability calculations on several alloy configurations indicated that Pd prefers to occupy undercoordinated edge sites under CO gas. Such adsorption-induced different, and even inverse segregation trend was also evidenced for Pt-Ni system. More precisely, using *in situ* X-ray photoelectron spectroscopy (XPS), Ahmadi *et al.* [51] analyzed the atomic evolution in Pt_{0.5}Ni_{0.5} NPs surfaces. The results show surface-segregation of Ni occurring only at low temperature (< 473-543 K) under 1 bar of hydrogen, while Pt was found to segregate to the NP surface only at higher temperature. These authors also pointed out that the chemical state of the NPs play a pivotal role in their surface composition as Ni surface segregation was only observed in H₂, O₂ and under vacuum as long as the PtO_x species were present in systems. The above examples stress the importance to predict the surface structure, composition as well as the adsorption-induced segregation phenomenon in TM alloys under operando (T , P)-condition that may significantly influence the catalytic properties.

3.2 DFT approach

The first accurate calculation using DFT that allowed to systematically scan the segregation preference of TM alloys under vacuum was proposed by Ruban *et al.* [48-49] by defining the segregation energy as the energy required for moving a diluted solute atom from the interior to the surface of the host crystal. Therefore, it is the total energy difference of the system with the

impurity in a surface layer and in the bulk. The calculated surface segregation energy results are found in good quantitative agreement with most of the available experimental data. Thereafter, based on the database of segregation energy of solute (E_{seg}) established by Ruban *et al.* for the TM alloys under vacuum, Greeley *et al.* [6] extended this model to estimate the adsorption-induced segregation trends of several alloy systems. Using DFT, these authors compared E_{seg} to the difference in magnitudes of the adsorption binding energies on the solute and on the host ($|BE_{ads}^{sol} - BE_{ads}^{host}|$). For instance, if the E_{seg} is positive (under vacuum), then it indicates that the solute is more stable in the bulk under vacuum, and if the binding energy of the adsorbed gas on the solute BE_{ads}^{sol} is stronger than the host surface BE_{ads}^{host} , the adsorbed gas will induce the solute segregating to the surface. These extrapolations based on surface models allow to efficiently screen a large number of different pairs of alloys with different compositions and to predict plausible segregation tendencies. This DFT calculation approach was also used to predict the chemical ordering and the electronic structures of several alloy nanoparticles consisting of dozens of atoms [52-54]. However, one of the limitations of this approach is that the segregation behavior is predicted from highly diluted limits of alloy composition i.e., the behavior of one solute, and the adsorption of isolated adsorbates, which neglect both the effect of alloy composition and the effect the adsorbate coverage.

To overcome these limitations and to capture a more realistic segregation behavior in alloys exposed to the reactive gas, other theoretical methods based on DFT calculations were developed.

3.3 DFT-aided thermodynamic modeling

As pointed out several times previously, including a thermodynamic term to DFT calculations is crucial for accurately modelling the effects of gas environment (T, P). On the question of gas-inducing segregation phenomena for alloys, the DFT-aided thermodynamic stands as a

valuable tool. Conventionally, the idea of this method is to identify the most stable structures by minimizing the surface free energy of different systems, where the Gibbs free energy and the chemical potentials of each alloy component as well as the gas species under specific (T , P)-conditions are described. The relevant energetics can be calculated by DFT using surface slab models with fixed surface compositions; therefore, only ordered structures can be predicted. For example, Kitchin and co-workers [55] studied the structure, composition and segregation of $\text{Ag}_3\text{Pd}(1\ 1\ 1)$ surface in contact with oxygen using the DFT-aided thermodynamic framework. To account for possible surface segregations, twenty-five (2×2) unit-cell slabs respecting the “3-Ag and 1-Pd” stoichiometry with compositions of topmost two layers varying from pure-Ag to pure-Pd, and with oxygen coverage varying between 0 to 1 ML were considered. Then for all configurations, the surface free energies of thermodynamically most stable configurations are evaluated as a function of oxygen chemical potentials, which is (T , P)-dependent, yielding at the respective minimal surface free energy, see **Figure I.2**.

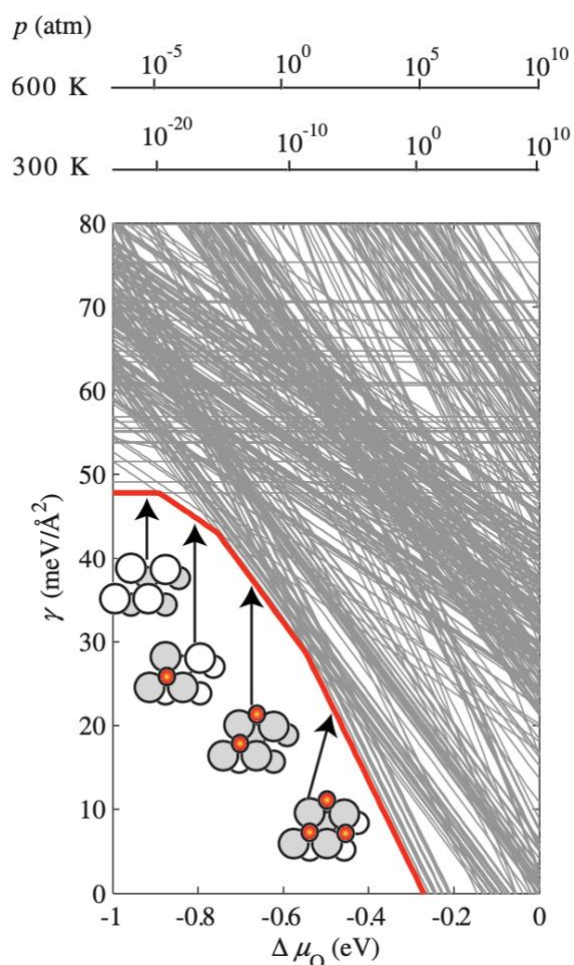


Figure I.2| Surface free energy of Ag₃Pd₁₁₁ in equilibrium with a Pd-rich Ag₃Pd bulk reservoir as a function of oxygen chemical potential. Each line corresponds to one of the tested surface configurations, and only the few configurations that result as most stable for a range of oxygen chemical potential are drawn as dark red lines. Additionally shown as insets are top views of the most stable surface configurations, with adsorbed O atoms shown as dark small circles, Ag atoms as white circles, and Pd atoms as grey circles. The dependence on the oxygen chemical potential is translated into pressure scales for $T=300$ K and $T=600$ K upper x axes. Figure adapted with permission under the terms of the Creative Commons Attribution 3.0 License, from [55].

With this predicted “surface free energy-oxygen chemical potential” correlation profile, the authors revealed that, under temperature of 300 and 600 K and in the oxygen-rich environment, the oxygen induces Pd surface segregation. The reversed segregation of Pd into the bulk was found under vacuum condition. Several other works using above approach to study Ag-Cu

alloys under oxygen atmosphere [56], or in mixture-(O₂, C₂H₄) condition [57] are also reported in the literature.

The above-mentioned works are all based on the description of surface free energy of system linked to thermodynamics, where large number of surface structures and adsorption configurations are needed to be considered. A more elegant DFT-aided thermodynamic method has recently been developed by our collaborators in Shanghai from Gao and Zhu's group. These colleagues have developed an environmental surface segregation energy prediction model [42], which provides a direct correlation between the segregation energy evolution of bimetallic alloys and their environmental gas (T, P)-condition. In this model, the segregation energies in presence of gas are directly revised with the gas-adsorption preference, the gas coverage and the lateral interaction by including the F-G adsorption isotherm. This simplified and “user-friendly” model compared to the previous ones, allows to screen the environmental segregation energy under reactive gas (T, P)-conditions of large number of TM alloy systems. This model has been successfully applied in the study of the surface composition evolution of 72 different bimetallic transition metal alloys (Cu, Ag, Au, Ni, Pd, Co, Rh and Ir) under various carbon monoxide gas pressure (from 1 to 10⁶ Pa) and temperature (from 300 to 1200 K) [42]. This model was then validated by comparing the predicted CO-induced segregation behaviors of several bimetallic TM alloys (Pt/Ni, Pd/Au, CO/Pt and Au/Cu, etc.) with a series of available experimental data which show great consistency. Benefitting from the “Cai Yuanpei Sino-Chinese Hubert Curien Partnership” scientific exchange programme, I spent several weeks in Gao and Zhu's group and learned about the environmental segregation energy model. Then I employed this high-throughput approach in the framework of this thesis to study the hydrogen-induced surface segregation behaviors of Pt-based bimetallic alloys exposed in **Chapter 5**.

Nevertheless, these DFT-aided thermodynamic approaches share the same limitation which is that only ordered alloy structures can be considered. In addition, as small unit cells periodically repeated in space cannot accommodate large deformations that might be induced by the segregation of atoms, size mismatch and stresses in alloyed surfaces cannot be captured.

3.4 DFT-based cluster expansion (CE) method

The DFT-based cluster expansion (CE) method [58-60] has been widely applied for investigating properties including chemical ordering and segregation phenomena of ordered as well as disordered structures [61-68]. The general idea of CE method is to provide a numerically efficient way for mapping the Hamiltonian of practically all numerous configurations of alloys using a remarkably reduced number of DFT-based total energy calculations. The number of configurations in CE can be reduced based on the idea that interactions are negligible beyond a certain distance, especially in metal alloys. Once the CE are constructed, the effect of the finite temperatures and/or gas pressures on the stability and chemical ordering of alloys are generally studied in conjunction with Monte Carlo simulations. For instance, Oguz and co-workers [69] investigated the equilibrium surface composition and the Pd segregation behavior of Au-Pd(1 0 0) system in presence of CO gas. The energetic parameters such as the adsorption evolution of CO on bridge and on top sites as well as the CO-CO interactions were evaluated using a set of DFT calculations to explicitly determine the Ising Hamiltonian. Then the latter was used to perform the Monte Carlo simulations within semi-grand canonical ensemble to reproduce the CO-induced segregation for Au-Pd(1 0 0) surface under different temperatures and CO pressures. As shown in **Figure I-3**, the evolutions of CO-coverage θ_{CO} and the surface Pd concentration C_{Pd}^{surf} are depicted as a function of the bulk Pd concentration C_{Pd}^{bulk} under different CO pressures at 300 and 600 K. These segregation isotherm diagrams indicate the appearance of two exotic stable surface phases depending on the adsorption configurations of

CO at $\theta_{CO} = 0.5$ and $T = 300$ K, where a plateau of surface Pd concentration C_{Pd}^{surf} and the θ_{CO} suggest the existence of an equilibrium ordered phase. When CO are adsorbed on the bridge sites, the ordered phase is formed with Pd-CO ensembles in linear chains separated by Au atoms also in linear chains and free from CO adsorptions (**Figure I-3-A**, at $C_{Pd}^{surf} = 0.5$ and $\theta_{CO} = 0.5$, when $P = 1 \times 10^3$ mbar); whereas when CO are on top sites, the ordered phase became checkerboard-like configuration with half of the surface sites occupied by Pd atoms adsorbed with a CO molecule and other half sites occupied by Au atoms free from CO (**Figure I-3-B**, at $C_{Pd}^{surf} = 0.5$ and $\theta_{CO} = 0.5$, and $P = 1 \times 10^{-4}$ mbar). These two ordered phases (plateau) both disappear when temperature increases to 600 K.

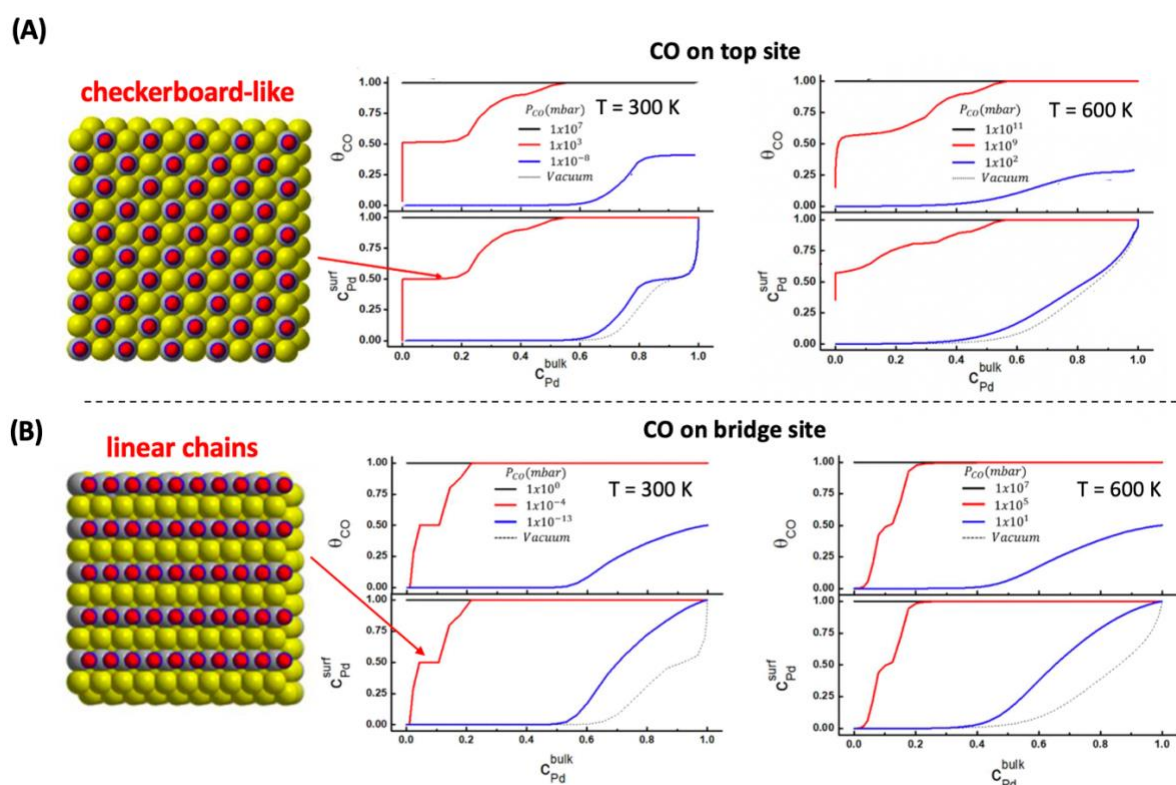


Figure I.3]. Segregation isotherms at 300 K and 600 K representing the evolutions of the CO coverage θ_{CO} (upper subfigure) and surface Pd concentration C_{Pd}^{surf} (inferior subfigure) as a function of the bulk Pd concentration C_{Pd}^{bulk} when (A) CO at top-sites and (B) CO at bridge sites. Figure adapted with permission from [69]. Copyright 2018 American Chemical Society

To sum up, for the study of surface segregation phenomena of alloy nanoparticles in *operando* reactive environment, the CE method is particularly suitable for systems containing large

number of surface configurations and components compared to the direct calculations using DFT or other sufficiently accurate but expensive simulation methods, such as *ab initio* molecular dynamics. However, the CE method is limited to the treatment of structures with a pre-determined lattice topology [70]. Another drawback of this method [65] resides in the fact that, as it is based on extended surface models, the lattice parameters of the surface are determined by the underlying bulk material, whereas, the bulk material is not included in a typical slab cluster expansion. Thus, it remains difficult to generate a cluster expansion for a system in which the bulk material can have different ranges of compositions and lattice parameters.

4. Conclusion and perspective

In this chapter, we presented a non-exhaustive overview of the theoretical methodologies used to investigate TMC nanoparticles evolving under reactive gas conditions. Two focuses were addressed: the study of the stability and the shape evolutions of monometallic NPs and the study of the surface structure/segregation in bimetallic alloys. Reviewing the state of art shows that several DFT-based methods are used to achieve *operando* theoretical modeling. Among them, *ab initio* molecular dynamics, DFT-based cluster expansion method and DFT-aided thermodynamic modeling were introduced, additionally examples of their application were also highlighted.

Advantages and limitations exist in each described approach and the goal of our overview is to realize and to measure the difficulties from theoretical cost and to compare with the needed accuracy of our investigated system. It comes from the fact that the choice of the adequate method is actually a compromise between the accuracy required to simulate the targeting issues, the complexity for building models and the computational costs. For instance, the cluster

expansion method, compared to the more accurate AIMD simulation, is a more appropriate choice in terms of study in surface composition/segregation of multi-component alloys thanks to its formalism. While for the monometallic NPs containing small numbers of atoms, the AIMD simulation may become a better choice owing to its better accuracy and more detailed information that can be provided.

Reference

- Zhang, M.; Fournier, R., Density-Functional-Theory Study of 13-Atom Metal Clusters M_{13} , $M = \text{Ta} - \text{Pt}$. *Physical Review A* **2009**, *79*, 043203.
- Barmparis, G. D.; Remediakis, I. N., Dependence on CO Adsorption of the Shapes of Multifaceted Gold Nanoparticles: A Density Functional Theory. *Physical Review B* **2012**, *86*.
- Zhang, J.; Mao, Y.; Zhang, J.; Tian, J.; Sullivan, M. B.; Cao, X. M.; Zeng, Y.; Li, F.; Hu, P., CO₂ Reforming of Ethanol: Density Functional Theory Calculations, Microkinetic Modeling, and Experimental Studies. *ACS Catalysis* **2020**, *10*, 9624-9633.
- Barmparis, G. D.; Lodziana, Z.; Lopez, N.; Remediakis, I. N., Nanoparticle Shapes by Using Wulff Constructions and First-Principles Calculations. *Beilstein J Nanotechnol* **2015**, *6*, 361-368.
- Cramer, C. J.; Truhlar, D. G., Density Functional Theory for Transition Metals and Transition Metal Chemistry. *Physical Chemistry Chemical Physics* **2009**, *11*, 10757-10816.
- Greeley, J.; Mavrikakis, M., Alloy Catalysts Designed from First Principles. *Nature Materials* **2004**, *3*, 810-815.
- Jennings, P. C.; Aleksandrov, H. A.; Neyman, K. M.; Johnston, R. L., A DFT Study of Oxygen Dissociation on Platinum Based Nanoparticles. *Nanoscale* **2014**, *6*, 1153-1165.
- Kacprzak, K. A.; Akola, J.; Hakkinen, H., First-Principles Simulations of Hydrogen Peroxide Formation Catalyzed by Small Neutral Gold Clusters. *Physical Chemistry Chemical Physics* **2009**, *11*, 6359-6364.
- Jørgensen, M.; Grönbeck, H., First-Principles Microkinetic Modeling of Methane Oxidation over Pd(100) and Pd(111). *ACS Catalysis* **2016**, *6*, 6730-6738.
- Kurth, S.; Marques, M. A. L.; Gross, E. K. U., Density-Functional Theory. In *Encyclopedia of Condensed Matter Physics*, Bassani, F.; Liedl, G. L.; Wyder, P., Eds. Elsevier: Oxford, 2005; pp 395-402.
- Komanicky, V.; Iddir, H.; Chang, K. C.; Menzel, A.; Karapetrov, G.; Hennessy, D.; Zapol, P.; You, H., Shape-Dependent Activity of Platinum Array Catalyst. *Journal of the American Chemical Society* **2009**, *131*, 5732-5733.
- Mistry, H.; Behafarid, F.; Zhou, E.; Ono, L. K.; Zhang, L.; Roldan Cuenya, B., Shape-Dependent Catalytic Oxidation of 2-Butanol over Pt Nanoparticles Supported on γ -Al₂O₃. *ACS Catalysis* **2014**, *4*, 109-115.
- McKibbin, S. R., et al., In Situ Observation of Synthesized Nanoparticles in Ultra-Dilute Aerosols Via X-Ray Scattering. *Nano Research* **2018**, *12*, 25-31.
- Stoltze, P.; Norskov, J. K., Bridging the "Pressure Gap" between Ultrahigh-Vacuum Surface Physics and High-Pressure Catalysis. *Physical Review Letters* **1985**, *55*, 2502-2505.
- Liu, L.; Corma, A., Metal Catalysts for Heterogeneous Catalysis: From Single Atoms to Nanoclusters and Nanoparticles. *Chemical Reviews* **2018**, *118*, 4981-5079.
- Norskov, J. K.; Bligaard, T.; Hvolbaek, B.; Abild-Pedersen, F.; Chorkendorff, I.; Christensen, C. H., The Nature of the Active Site in Heterogeneous Metal Catalysis. *Chemical Society Reviews* **2008**, *37*, 2163-2171.
- Shi, Y.; Lyu, Z.; Zhao, M.; Chen, R.; Nguyen, Q. N.; Xia, Y., Noble-Metal Nanocrystals with Controlled Shapes for Catalytic and Electrocatalytic Applications. *Chemical Reviews* **2021**, *121*, 649-735.
- Haruta, M., Nanoparticulate Gold Catalysts for Low-Temperature CO Oxidation. *ChemInform* **2004**, *35*.
- An, K.; Somorjai, G. A., Size and Shape Control of Metal Nanoparticles for Reaction Selectivity in Catalysis. *Chemical Catalysis Catalytical Chemistry* **2012**, *4*, 1512-1524.

20. Xie, S.; Choi, S.-I.; Xia, X.; Xia, Y., Catalysis on Faceted Noble-Metal Nanocrystals: Both Shape and Size Matter. *Current Opinion in Chemical Engineering* **2013**, *2*, 142-150.
21. Cao, S.; Tao, F. F.; Tang, Y.; Li, Y.; Yu, J., Size- and Shape-Dependent Catalytic Performances of Oxidation and Reduction Reactions on Nanocatalysts. *Chemical Society Reviews* **2016**, *45*, 4747-4765.
22. Zhang, H.; Jin, M.; Xia, Y., Noble-Metal Nanocrystals with Concave Surfaces: Synthesis and Applications. *Angewandte Chemie International Edition* **2012**, *51*, 7656-7673.
23. Wang, H.; Zhou, S.; Gilroy, K. D.; Cai, Z.; Xia, Y., Icosahedral Nanocrystals of Noble Metals: Synthesis and Applications. *Nano Today* **2017**, *15*, 121-144.
24. Yoshida, H.; Matsuura, K.; Kuwauchi, Y.; Kohno, H.; Shimada, S.; Haruta, M.; Takeda, S., Temperature-Dependent Change in Shape of Platinum Nanoparticles Supported on CeO₂ During Catalytic Reactions. *Applied Physics Express* **2011**, *4*, 065001.
25. Vendelbo, S. B., et al., Visualization of Oscillatory Behaviour of Pt Nanoparticles Catalysing CO Oxidation. *Nature Materials* **2014**, *13*, 884-890.
26. Wulff, G., Xxv. Zur Frage Der Geschwindigkeit Des Wachstums Und Der Auflösung Der Krystallflächen. *Zeitschrift für Kristallographie - Crystalline Materials* **1901**, *34*, 449.
27. Shi, Q.; Sun, R., Adsorption Manners of Hydrogen on Pt(1 0 0), (1 1 0) and (1 1 1) Surfaces at High Coverage. *Computational and Theoretical Chemistry* **2017**, *1106*, 43-49.
28. Yan, Z.; Taylor, M. G.; Mascareno, A.; Mpourmpakis, G., Size-, Shape-, and Composition-Dependent Model for Metal Nanoparticle Stability Prediction. *Nano Letters* **2018**, *18*, 2696-2704.
29. Jiang, F.; Yang, L.; Zhou, D.; He, G.; Zhou, J.; Wang, F.; Chen, Z.-G., First-Principles Atomistic Wulff Constructions for an Equilibrium Rutile TiO₂ Shape Modeling. *Applied Surface Science* **2018**, *436*, 989-994.
30. Gibbs, J. W., A Method of Geometrical Representation of the Thermodynamic Properties of Substances by Means of Surfaces. In *Transactions of the Connecticut Academy of Arts and Sciences*, The Academy: 1873; Vol. 2, pp 382-404.
31. Wang, T.; Wang, S.; Luo, Q.; Li, Y.-W.; Wang, J.; Beller, M.; Jiao, H., Hydrogen Adsorption Structures and Energetics on Iron Surfaces at High Coverage. *The Journal of Physical Chemistry C* **2014**, *118*, 4181-4188.
32. Huo, C. F.; Wu, B. S.; Gao, P.; Yang, Y.; Li, Y. W.; Jiao, H., The Mechanism of Potassium Promoter: Enhancing the Stability of Active Surfaces. *Angewandte Chemie International Edition* **2011**, *50*, 7403-7406.
33. Reuter, K.; Scheffler, M., First-Principles Atomistic Thermodynamics for Oxidation Catalysis: Surface Phase Diagrams and Catalytically Interesting Regions. *Physical Review Letters* **2003**, *90*, 046103.
34. Rogal, J.; Reuter, K.; Scheffler, M., First-Principles Statistical Mechanics Study of the Stability of a Subnanometer Thin Surface Oxide in Reactive Environments: CO Oxidation at Pd(100). *Physical Review Letters* **2007**, *98*, 046101.
35. Ouyang, R.; Liu, J. X.; Li, W. X., Atomistic Theory of Ostwald Ripening and Disintegration of Supported Metal Particles under Reaction Conditions. *Journal of the American Chemical Society* **2013**, *135*, 1760-1771.
36. Liu, J. C.; Wang, Y. G.; Li, J., Toward Rational Design of Oxide-Supported Single-Atom Catalysts: Atomic Dispersion of Gold on Ceria. *Journal of the American Chemical Society* **2017**, *139*, 6190-6199.
37. Zhu, B.; Meng, J.; Gao, Y., Equilibrium Shape of Metal Nanoparticles under Reactive Gas Conditions. *The Journal of Physical Chemistry C* **2017**, *121*, 5629-5634.
38. Duan, M.; Yu, J.; Meng, J.; Zhu, B.; Wang, Y.; Gao, Y., Reconstruction of Supported Metal Nanoparticles in Reaction Conditions. *Angewandte Chemie, International Edition in English* **2018**, *57*, 6464-6469.

39. Mayernick, A. D.; Janik, M. J., Ab Initio Thermodynamic Evaluation of Pd Atom Interaction with CeO₂ Surfaces. *The Journal of Chemical Physics* **2009**, *131*, 084701.
40. Liu, S. Y., et al., Oxidation of the Two-Phase Nb/Nb₅Si₃ Composite: The Role of Energetics, Thermodynamics, Segregation, and Interfaces. *The Journal of Chemical Physics* **2013**, *138*, 014708.
41. Liu, S. Y.; Liu, S.; Li, D. J.; Wang, S.; Guo, J.; Shen, Y., Ab Initio Atomistic Thermodynamics Study on the Oxidation Mechanism of Binary and Ternary Alloy Surfaces. *The Journal of Chemical Physics* **2015**, *142*, 064705.
42. Meng, J.; Zhu, B. E.; Gao, Y., Surface Composition Evolution of Bimetallic Alloys under Reaction Conditions. *The Journal of Physical Chemistry C* **2019**, *123*, 28241-28247.
43. He, Y.; Liu, J. C.; Luo, L.; Wang, Y. G.; Zhu, J.; Du, Y.; Li, J.; Mao, S. X.; Wang, C., Size-Dependent Dynamic Structures of Supported Gold Nanoparticles in CO Oxidation Reaction Condition. *PNAS* **2018**, *115*, 7700-7705.
44. Creuze, J.; Guesmi, H.; Mottet, C.; Zhu, B. E.; Legrand, B., Surface Segregation in AuPd Alloys: Ab Initio Analysis of the Driving Forces. *Surface Science* **2015**, *639*, 48-53.
45. Lambin, P.; Gaspard, J. P., Analysis of the Density of States of Binary Alloys. Ii. Surface Segregation. *Journal of Physics F: Metal Physics* **1980**, *10*, 2413-2428.
46. Foiles, S. M.; Baskes, M. I.; Daw, M. S., Embedded-Atom-Method Functions for the Fcc Metals Cu, Ag, Au, Ni, Pd, Pt, and Their Alloys. *Physical Review B* **1986**, *33*, 7983-7991.
47. Brejnak, M.; Modrak, P., Electronic Theory of Surface Segregation for Dilute Transition Metal Alloys: Predictions Based on Rigid-Band-Like Approach. *Surface Science* **1991**, *247*, 215-221.
48. Ruban, A. V.; Skriver, H. L.; Norskov, J. K., Surface Segregation Energies in Transition-Metal Alloys. *Physical Review B* **1999**, *59*, 15990-16000.
49. Nilekar, A. U.; Ruban, A. V.; Mavrikakis, M., Surface Segregation Energies in Low-Index Open Surfaces of Bimetallic Transition Metal Alloys. *Surface Science* **2009**, *603*, 91-96.
50. Zhu, B.; Thirumurthulu, G.; Delannoy, L.; Louis, C.; Mottet, C.; Creuze, J.; Legrand, B.; Guesmi, H., Evidence of Pd Segregation and Stabilization at Edges of AuPd Nano-Clusters in the Presence of CO: A Combined DFT and Drifts Study. *Journal of Catalysis* **2013**, *308*, 272-281.
51. Ahmadi, M.; Behafarid, F.; Cui, C.; Strasser, P.; Cuenya, B. R., Long-Range Segregation Phenomena in Shape-Selected Bimetallic Nanoparticles: Chemical State Effects. *ACS Nano* **2013**, *7*, 9195-9204.
52. Barcaro, G.; Fortunelli, A.; Polak, M.; Rubinovich, L., Patchy Multishell Segregation in Pd-Pt Alloy Nanoparticles. *Nano Letters* **2011**, *11*, 1766-1769.
53. Gould, A. L.; Heard, C. J.; Logsdail, A. J.; Catlow, C. R., Segregation Effects on the Properties of (AuAg)₁(4)(7). *Physical Chemistry Chemical Physics* **2014**, *16*, 21049-21061.
54. Xu, H.; Liu, P.; Zhang, W.; Wang, Q.; Yang, Y., Structure, Stability, Electronic and Magnetic Properties of Monometallic Pd, Pt, and Bimetallic Pd-Pt Core-Shell Nanoparticles. *Chemical Physics* **2020**, *539*.
55. Kitchin, J. R.; Reuter, K.; Scheffler, M., Alloy Surface Segregation in Reactive Environments: First-Principles Atomistic Thermodynamics Study of Ag₃Pd(111) in Oxygen Atmospheres. *Physical Review B* **2008**, *77*.
56. Piccinin, S., et al., Alloy Catalyst in a Reactive Environment: The Example of Ag-Cu Particles for Ethylene Epoxidation. *Phys Rev Lett* **2010**, *104*, 035503.
57. Nguyen, N. L.; Piccinin, S.; de Gironcoli, S., Stability of Intermediate States for Ethylene Epoxidation on Ag-Cu Alloy Catalyst: A First-Principles Investigation. *The Journal of Physical Chemistry C* **2011**, *115*, 10073-10079.
58. Lee, R. J.; Raich, J. C., Cluster Expansion for Solid Orthohydrogen. *Physical Review B* **1972**, *5*, 1591-1604.

59. Ceder, G.; Asta, M.; Carter, W. C.; Kraitichman, M.; de Fontaine, D.; Mann, M. E.; Sluiter, M., Phase Diagram and Low-Temperature Behavior of Oxygen Ordering in $\text{Yba}_2\text{cu}_3\text{oz}$ Using Ab Initio Interactions. *Physical Review B* **1990**, *41*, 8698-8701.
60. Wu, Q.; He, B.; Song, T.; Gao, J.; Shi, S., Cluster Expansion Method and Its Application in Computational Materials Science. *Computational Materials Science* **2016**, *125*, 243-254.
61. Han, B. C.; Van der Ven, A.; Ceder, G.; Hwang, B.-J., Surface Segregation and Ordering of Alloy Surfaces in the Presence of Adsorbates. *Physical Review B* **2005**, *72*.
62. Yuge, K.; Seko, A.; Kuwabara, A.; Oba, F.; Tanaka, I., Ordering and Segregation of a $\text{Cu}_{75}\text{Pt}_{25}(111)$ Surface: A First-Principles Cluster Expansion Study. *Physical Review B* **2007**, *76*.
63. Chen, W.; Schmidt, D.; Schneider, W. F.; Wolverton, C., Ordering and Oxygen Adsorption in Au–Pt/Pt(111) Surface Alloys. *The Journal of Physical Chemistry C* **2011**, *115*, 17915-17924.
64. Chen, W.; Dalach, P.; Schneider, W. F.; Wolverton, C., Interplay between Subsurface Ordering, Surface Segregation, and Adsorption on Pt-Ti(111) near-Surface Alloys. *Langmuir* **2012**, *28*, 4683-4693.
65. Cao, L.; Li, C.; Mueller, T., The Use of Cluster Expansions to Predict the Structures and Properties of Surfaces and Nanostructured Materials. *Journal of Chemical Information and Modeling* **2018**, *58*, 2401-2413.
66. Li, C.; Raciti, D.; Pu, T.; Cao, L.; He, C.; Wang, C.; Mueller, T., Improved Prediction of Nanoalloy Structures by the Explicit Inclusion of Adsorbates in Cluster Expansions. *The Journal of Physical Chemistry C* **2018**, *122*, 18040-18047.
67. Papanikolaou, K. G.; Darby, M. T.; Stamatakis, M., Engineering the Surface Architecture of Highly Dilute Alloys: An Ab Initio Monte Carlo Approach. *ACS Catalysis* **2019**, *10*, 1224-1236.
68. Xue, H. T.; Yu, X. D.; Aarons, J.; Tang, F. L.; Lu, X. F.; Ren, J. Q., Cluster Expansion Monte Carlo Study of Indium-Aluminum Segregation and Homogenization in $\text{Cu}_{\text{InSe}_2}$ - $\text{Cu}_{\text{AlSe}_2}$ Pseudobinary Alloys. *Physical Chemistry Chemical Physics* **2020**, *22*, 14694-14703.
69. Oğuz, I. C.; Mineva, T.; Creuze, J.; Guesmi, H., Equilibrium Au–Pd(100) Surface Structures under CO Pressure: Energetic Stabilities and Phase Diagrams. *The Journal of Physical Chemistry C* **2018**, *122*, 18922-18932.
70. Guesmi, H., Theoretical Insights on the Effect of Reactive Gas on the Chemical Ordering of Gold-Based Alloys. *Gold Bulletin* **2013**, *46*, 213-219.

Chapter II

Theoretical background

The purpose of this chapter is to introduce the principles of theoretical approaches employed and developed in this thesis. Thus, in the first and second sections, the density functional theory (DFT), which is the cornerstone of all multi-scale approaches developed in this thesis, is presented by reviewing the historical background of fundamental theories of quantum chemistry and developments from Hartree-Fock method to classical DFT. In the third section, the molecular dynamics (MD) simulation methods in particular, the *ab initio* molecular dynamics (AIMD) are presented. The final section is dedicated to the introduction of thermodynamic approaches and to recall the principles of environmental construction methods of NPs.

1. Introduction to quantum chemistry

Quantum chemistry strives to predict chemical and physical properties of the materials and molecules. This is achieved through the precise description of their electronic structures in a microscopic level by solving the time-independent Schrödinger equations **(II.1)**.

$$H\Psi_i(r, R) = E_i\Psi_i(r, R) \tag{II.1}$$

where E_i is the eigenvalue representing the quantized energy of the system; $\Psi_i(r, R)$ is the wave function of state of the system, which depends on every factor that influences the system; H is the Hamiltonian corresponding to the energy of the system.

The Hamiltonian of a system with nuclei and electrons can be expressed as the sum of kinetic and potential energies, including explicitly all electronic and nuclear contributions:

$$\begin{aligned}
 H &= -\sum_{i=1}^N \frac{1}{2} \nabla_i^2 - \sum_{A=1}^M \frac{1}{2M_A} \nabla_A^2 - \sum_{i=1}^N \sum_{A=1}^M \frac{Z_A}{r_{iA}} + \sum_{i=1}^N \sum_{j>1}^N \frac{1}{r_{ij}} + \sum_{A=1}^M \sum_{B>A}^M \frac{Z_A Z_B}{R_{AB}} \\
 &= T_e + T_n + V_{ne} + V_{ee} + V_{nn}
 \end{aligned} \tag{II.2}$$

where Z_A and Z_B are masses of nuclei, r_{iA} , r_{iB} and R_{AB} are distance between electron-nuclei, electron-electron and nuclei-nuclei at i^{th} state, respectively.

The Schrödinger equation of atoms or ions with more than one electron (called many-body systems) cannot be solved analytically, because of the computational difficulty imposed by the Coulomb interaction between the electrons. Thus, some approximation approaches, such as the Hartree-Fock method, are proposed in order to solve the Schrödinger equation for many-body systems.

1.1 Hartree-Fock method

The Hartree-Fock (HF) method [1] is a variational method of approximation for the determination of wave function and the energy of a many-body system. It assumes that wave function of the system can be approximated in the form of a single Slater determinant for Fermions and of a single product of wave function (spin-orbitals) for Bosons. To this end, the Born-Oppenheimer (BO) approximation is assumed in HF method and the HF equations are solved using iteration method, namely “Self-Consistent Field” approximation.

1.1.1 Born-Oppenheimer approximation

The Born-Oppenheimer (BO) approximation assumes that the nuclei and electrons have extremely different masses, so that their movements are decoupled. Based on this postulate, one can split the Schrödinger equation into two terms: one electronic term versus the fixed nuclei and one nuclear term for which the electronic energy acts as an effective potential energy. Thus, the nuclei which moves on a potential energy surface (PES) is the solution of the electronic component of the Schrödinger equation.

The electronic Schrödinger equation **(II.3-II.4)** is solved approximately with kinetic energy neglected (is a constant parameter):

$$H^e \Psi^e(r, R) = E^e(R) \Psi^e(r, R) \quad \text{(II.3)}$$

$$H^e = - \sum_{i=1}^N \frac{1}{2} \nabla_i^2 - \sum_{i=1}^N \sum_{A=1}^M \frac{Z_A}{r_{iA}} + \sum_{i=1}^N \sum_{j>1}^N \frac{1}{r_{ij}} \quad \text{(II.4)}$$

with Ψ^e depends on all electronic coordinates r and all nuclear coordinates R ; $E^e(R)$ is a function of (PES) by repeatedly solving the electronic Schrödinger equation in varying the positions R .

The nuclear Schrödinger equation **(II.5-II.6)** is solved as:

$$H^n \Psi^n(R) = E^n(R) \Psi^n(R) \quad \text{(II.5)}$$

$$H^n = - \sum_{A=1}^M \frac{1}{2M_A} \nabla_A^2 + E^e(R) + \sum_{A=1}^M \sum_{B>A}^M \frac{Z_A Z_B}{R_{AB}} \quad \text{(II.6)}$$

Solving the above nuclear term gives access to the molecular rotation and nuclear vibration information.

The BO approximation is expected to be accurate and economic in term of computational resources for most molecules. However, it loses the adequacy if two electronic states (nuclei

and electrons) are no longer separable. As showed in Equation (II.4), it is still a many-body problem, which is hard to solve exactly since the interactions between electrons remain uncertain, but it is often used as a prerequisite for more refined methods, e.g., Hartree-Fock method.

1.1.2 Self-consistent filed approximation

The self-consistent filed approximation was proposed by Hartree [2] in 1927 then developed by Fock [2] in 1930. In this theory, each electron is considered as under an average effect of surrounding electrons (mean field), so that the many-body problem is reduced into effective one-body problem. Thus, instead of solving one Schrödinger equation with N interacting electrons, we solve N Schrödinger equations with one electron (Hartree-Fock equations):

The Hamiltonian of the electron depends on the wave function of other electrons,

$$h_i^{HF} = -\frac{1}{2}\nabla_i^2 - \sum_{A=1}^M \frac{Z_A}{r_{iA}} + V_i^{eff}(j) \quad (\text{II.7})$$

and the effective potential depends on the density of other electrons:

$$V_i^{eff}(j) \propto \sum_{j \neq i} \int \frac{\rho_j}{r_{ij}} dr_i \quad (\text{II.8})$$

where

$$\rho_j = |\varnothing_j|^2$$

The idea of this method is to describe the wave functions as a product of one-electron orbitals. And as electrons are Fermions, the wave function has to be anti-symmetric, which is approximated by a single Slater determinant (II.9) showed as below:

$$\psi(\mathbf{r}_1, \mathbf{r}_2, \dots) = \frac{1}{\sqrt{N!}} \begin{vmatrix} \phi_1(\mathbf{r}_1)\alpha(1) & \phi_1(\mathbf{r}_1)\beta(1) & \phi_1(\mathbf{r}_1)\alpha(1) & \dots \\ \phi_2(\mathbf{r}_2)\alpha(2) & \phi_2(\mathbf{r}_2)\beta(2) & \phi_2(\mathbf{r}_2)\alpha(2) & \dots \\ \phi_3(\mathbf{r}_3)\alpha(3) & \phi_3(\mathbf{r}_3)\beta(3) & \phi_3(\mathbf{r}_3)\alpha(3) & \dots \\ \dots & \dots & \dots & \dots \end{vmatrix} \quad (\text{II.9})$$

where N is the number of electrons in the system; the columns correspond to all spin-orbitals and each electron is represented in rows. A self-consistent procedure is needed for solving above Hartree-Fock equations: it starts with an initial guess for the orbitals to get a trial charge density, which allows to calculate the effective potential energies with those orbitals; solve the set of one-body Schrödinger equations to obtain new corresponding wave functions for electrons; re-calculate the effective potential to solve again the Schrödinger equations; repeat this procedure until reaching the convergence.

The “electron-electron” exchange interaction **(II.10)** (two electrons with parallel spins) in this method is taken into account by using the anti-symmetrized wave function (Slater determinant **(II.9)**), in which the Pauli principle is satisfied. However, the Coulomb correlation **(II.11)** cannot be properly described. Because in the HF mean field approximation, interactions between electrons are treated as an average density of surrounding electrons, there is no explicit correlation of electron movement included.

$$K_{ij} = \langle \phi_i(1)\phi_j(2) | \frac{1}{r_{ij}} | \phi_j(2)\phi_i(1) \rangle \quad (\text{II.10})$$

$$J_{ij} = \langle \phi_i(1)\phi_j(2) | \frac{1}{r_{ij}} | \phi_i(1)\phi_j(2) \rangle \quad (\text{II.11})$$

In brief, HF method provides the best single-determinant wave function which allows to recover approximately 99% energy of many-body systems. However, because of the high computational cost, this method is generally limited to the case of few atoms, molecules and small nanostructures. In addition, HF method suffers from problems of electronic correlation

that may be corrected using the so-called Post-Hartree-Fock methods, such as Configuration Interaction (CI), Møller-Plesset (MP) perturbation theory and Coupled cluster method (CC), as well as several emerging methods [3].

2. Density functional theory methods

The density functional theory (DFT) has been the most widely used method for structure and phase stability predictions, thermodynamics and description of electronic properties in computational quantum chemistry and materials science. The DFT methods are generally quicker than post-HF. They describe the electronic states of atoms, molecules and materials in terms of the 3D electronic density of system, which is a great simplification over wave function theory. Moreover, DFT has been shown to be very effective for metals, especially transition metals [4]. The reason for this added advantage is that DFT includes the electron correlation more efficiently than the HF calculations do.

The DFT was firstly proposed in Thomas-Fermi model, then the formalization of the two Hohenberg-Kohn [5] theorems has built its firm foundation. The practical computational use of DFT was finally established thanks to the development of the Kohn-Sham equations by Kohn and Sham [6].

2.1 Thomas-Fermi model

Thomas-Fermi model provides a functional for the kinetic energy of a non-interacting electron gas system as function of the density:

$$T_{TF}[\rho(r)] = \frac{3}{10} (3\pi^2)^{\frac{2}{3}} \int \rho^{\frac{5}{3}}(r) dr \quad (\text{II.12})$$

and the total Thomas-Fermi energy functional in form of density is the sum of kinetic energy and potential energy between nuclei-electron and electron-electron:

$$\begin{aligned}
 E_{TF}[\rho(r)] &= T_{TF}[\rho(r)] + V_{ne}[\rho(r)] + V_{ee}[\rho(r)] \\
 &= T_{TF}[\rho(r)] + \sum_A^{core} \int \frac{-Z_A}{|r-r_A|} \rho(r) dr + \frac{1}{2} \iint \frac{\rho(r_1)\rho(r_2)}{|r_1-r_2|} dr_1 dr_2
 \end{aligned}
 \tag{II.13}$$

One can find from above equation that the exchange and correlation energies are not included.

The Bloch-Dirac exchange term can be added into the Thomas-Fermi model:

$$E_{ex}[\rho(r)] = -\frac{3}{4} \left(\frac{3}{\pi}\right)^{\frac{1}{3}} \int \rho^{\frac{4}{3}}(r) dr
 \tag{II.14}$$

Although with this exchange term, this model remains inaccurate for most systems since they are considered within the homogeneous electron gas. Indeed, the electronic cloud is so localized that the chemical bonds cannot be accurately described. In any way, this Thomas-Fermi model is viewed as the precursor to DFT development through the transition from wave function theory into electronic density problems.

2.2 Hohenberg-Kohn theorems

Hohenberg and Kohn [5] developed two theorems. The first one states that all the properties of a molecular system are determined uniquely by its ground-state electron density function $\rho(r)$. This means that since the Hamiltonian is fully determined, all properties of the system are determined.

The second theorem states that there exists a functional $F[\rho]$ that describes the ground state energy of the system, which is the lowest energy if and only if the density is the true ground state density $\rho_0(r)$. Thus, by means of lowest energy, the ground state energy E_0 fulfils:

$$E_0 \leq E[\rho] = T[\rho(r)] + V_{ne}[\rho(r)] + V_{ee}[\rho(r)] \quad (\text{II.15})$$

The proof of above relation is lied on the variational principle established for wave functions. Now, if one considers a trial density $\tilde{\rho}(r)$, based on the first theorem, it defines the corresponding Hamiltonian which results its own wave function $\tilde{\psi}$. Thus, with this trial wave function generated from its external potential V_{ext} , we can have:

$$\begin{aligned} \langle \tilde{\psi} | \hat{H} | \tilde{\psi} \rangle &= T[\tilde{\rho}(r)] + \int \tilde{\rho}(r) V_{ext} dr + V_{ee}[\tilde{\rho}(r)] = E[\tilde{\rho}] \geq E_0[\rho_0] \\ &= \langle \Psi_0 | \hat{H} | \Psi_0 \rangle \end{aligned} \quad (\text{II.16})$$

which conforms the result.

In summary, the Hohenberg-Kohn theorems establish the variational principle and proof the existence of unique ground state density $\rho_0(r)$ and ground state energy E_0 . These theorems provide a major theoretical pillar on modern practical computational density functional theory.

2.3 Kohn-Sham method

The Hohenberg-Kohn theorems were further developed by Kohn and Sham in 1965, named as Kohn-Sham equations [7]. Within this approach, a fictitious non-interacting system is constructed in a way that its density is the same as that of any given system of interacting electrons. The total energy of such system is expressed as:

$$E[\rho(r)] = \int v_{ext}(r)\rho(r)dr + \frac{1}{2} \int \int \frac{\rho(r)\rho(r')}{|r-r'|} drdr' + T_k[\rho(r)] + E_{xc}[\rho(r)] \quad (\text{II.17})$$

where T_k is the kinetic energy of the independent particles. All the electron-electron interactions are combined into the single entity exchange-correlation energy functional E_{xc} . The Schrödinger like the Kohn-Sham variational equations are solved in a self-consistent way:

$$\hat{H}_{ks}\varphi_i(r) = \epsilon_i\varphi_i(r) \quad (\text{II.18})$$

where $\varphi_i(r)$ are the corresponding Kohn-Sham orbitals and ϵ_i are their orbital energies. The orbitals are related to the density of respective N-electrons system:

$$\rho(r) = \sum_i^N |\varphi_i(r)|^2 \quad (\text{II.19})$$

where one has the effective Kohn-Sham potential v_{ks} as:

$$v_{ks}(r) = v_{ext}(r) + v_H(r) + v_{xc}(r) \quad (\text{II.20})$$

with v_H representing the Hartree energy.

From a practical point of view, the advantage of this method is the use of independent electronic kinetic energy, which makes the large scale of intensive calculations possible.

2.4 Exchange-correlation functionals

The exchange-correlation functionals E_{xc} in DFT are not known exactly. Different approximations exist, thereto the most widely used ones are the local density approximation (LDA) and the generalized gradient approximation (GGA).

2.4.1 Local density approximation

The local density approximation (LDA) assumes that the density can be treated locally inside of a uniform electron gas system, where the exchange-correlation energy per particle of a homogeneous electron gas of charge density $\rho(r)$ can be written as:

$$E_{xc}^{LDA}[\rho] = \int \rho(r) \epsilon_{xc}^{HEG}(\rho(r)) dr \quad (\text{II.21})$$

The LDA provides accurate results for simple homogeneous systems but is unable to describe molecular and electron-rich systems where the charge density is far from being homogenous. In addition, the LDA generally overestimates the correlation energy and underestimates the exchange energy.

2.4.2 Generalized gradient approximation

The generalized gradient approximation (GGA) improves LDA by taking into consideration the term of gradient of the density that account for the non-homogeneous electron density. In this approximation, the exchange-correlation energy is expressed as:

$$E_{xc}^{GGA} = \int d^3r \epsilon_{xc}^{GGA}[\rho(r), \nabla\rho(r)] \quad (\text{II.22})$$

In this thesis, the GGA proposed by Perdew, Burke and Ernzerhof [8] has been applied for all DFT calculations, due to its good performance in description of geometries and energy of transition metal systems.

2.5 Projector augmented-wave method

Valence wave function in the core regions trends to oscillate rapidly due to the orthogonality. This problematic behavior requires a very fine mesh in order to describe correctly wave functions. The projector augmented-wave (PAW) [9] technique is thus introduced to solve this issue by using pseudopotentials that transform the rapid oscillating wave functions into much smoother wave functions. The PAW method is often combined with frozen core approximation to have further computational convenience.

2.6 Brillouin zone sampling

In DFT, the total energy of targeted system can be described using Kohn-Sham equations in conjunction with Bloch's [10] theorem, which allows to consider only the electron wave functions lying within the first Brillouin zone (BZ) in reciprocal space. This results in considerable reducing of computational resources. Furthermore, it is sufficient to sample only the *irreducible wedge* in the square-lattice BZ if the system possesses point symmetries wherein the symmetric operations can be applied to reduce the number of *k-points*. In this thesis, the Monkhorst-Pack mesh [11] is chosen in order to facilitate the generation of *k-points* for DFT calculations of periodic systems.

2.7 Dispersion correction

The Van der Waals interactions are indispensable part for certain dispersion-dominated materials because of the existence of long-range weak interaction. In standard Kohn-Sham DFT,

these interactions are not properly described. A conventional method to correct this problem is to add a correction term to the Kohn-Sham DFT energy, using available approximations. Among them, the dispersion correction methods referred to as DFT-D methods developed by Grimme *et al.* [12-14] are largely used in molecular and solid-state applications. In the DFT-D1 and DFT-D2 methods, the dispersion term takes the form:

$$E_{disp} = -\frac{1}{2} \sum_{i=1}^{N_{at}} \sum_{j=1}^{N_{at}} \left(f_{d,6}(R_{ij}) \frac{C_{6ij}}{r_{ij}^6} \right) \quad (\text{II.23})$$

where N_{at} is the number of atoms in the system; R_{ij} denotes as the interatomic distance between atom pairs i and j ; C_{nij} is the n -order dispersion coefficients for the atom pair and $f_{d,n}$ are the damping functions. The difference between DFT-D1 and DFT-D2 lies in the values of $f_{d,n}$ and C_{nij} .

While in the DFT-D3 method, higher C_{nij} term (8-order dispersion coefficient) is included, in the form:

$$E_{disp} = -\frac{1}{2} \sum_{i=1}^{N_{at}} \sum_{j=1}^{N_{at}} \left(f_{d,6}(R_{ij}) \frac{C_{6ij}}{r_{ij}^6} + f_{d,8}(R_{ij}) \frac{C_{8ij}}{r_{ij}^8} \right) \quad (\text{II.24})$$

Unlike the DFT-D1 and -D2, the 6- and 8-order dispersion coefficients (C_{6ij} , C_{8ij}) in DFT-D3 are adjustable and geometry-dependent based on the coordination number of each atom pairs i and j . This makes DFT-D3 more accurate than the previous versions which include only 6-order C_{6ij} term that is fixed and independent of the environment. Thus, the DFT-D3 is chosen in this thesis to account for the dispersion energy of studied systems.

3. Molecular dynamics simulations

Molecular Dynamics (MD) simulation method has proven to be a valuable tool for studying the structure of molecular and solid materials during certain period of time. MD simulations are in many aspects similar to real experiments and better yet, thanks to their atomistic resolution. MD simulations are able to reveal interatomic interactions of materials, which generally cannot be adequately described by experimental means.

3.1 Potentials in *ab initio* methods

In MD simulations, for a given system with N particles, the trajectories of these particles are determined by solving Newton's equations of motion (II.25).

$$F = m\ddot{r} \quad (\text{II.25})$$

where F is the force, m is the mass of the particle and \ddot{r} is the acceleration.

Such process consists in calculation of forces between interacting particles and their potential energies. Depending on the targeted levels of accuracy, the description of potential energies can be achieved by classical approaches and molecular mechanics or using quantum mechanics. In this thesis, the potentials are defined based on quantum mechanics. More precisely, DFT is chosen to reach a finer description of electronic structure and chemical reactions, wherein the motion of nucleus is based on Born–Oppenheimer (BO) approximation. This method is named as *ab initio* molecular dynamics (AIMD). It allows to calculate the potential energy of the system on the fly as the trajectory is generated. In addition, as electrons are included, it produces information on chemical bonds (breaking and formation of bonds) and other electronic

properties. However, as the electronic variables are treated as active degrees of freedom in AIMD, it is very expensive to run AIMD simulations for systems of few hundred of atoms.

3.2 Statistical mechanics

The positions and velocities of particles in MD simulation system are described in the level of microscopic states. It is of great importance to convert these microscopic information into observable macroscopic properties, such as temperature (T), pressure (P), energy (E), volume (V), etc. This requires the use of Statistical Mechanics, which connects the microscopic properties with macroscopic thermodynamic observables by the means of probability functions. The thermodynamic ensemble conception from statistical mechanics is thus introduced. Several important ensembles depending on parameters N (number of atoms), P , T , V and E are listed below:

- (i) **Microcanonical Ensemble (NVE)**: the system is isolated from changes in N , E and V ;
- (ii) **Canonical Ensemble (NVT)**: N , V and T are fixed. In NVT, the energy of endothermic and exothermic processes are exchanged with a thermostat. There are different thermostat algorithms available embedded in VASP to control temperatures such as the Nosé-Hoover Thermostat, Andersen Thermostat, Langevin Thermostat and Multiple Andersen Thermostat;
- (iii) **Isobaric-Isothermal Ensemble (NPT)**: N , P and T are conserved.

In statistical mechanics, averages observables are defined as ensemble averages $\langle \Omega \rangle$:

$$\langle \Omega \rangle = \int \int dp^N dr^N \Omega(p^N, r^N) \rho(p^N, r^N) \quad (\text{II.26})$$

$$\rho(p^N, r^N) = \frac{1}{Z} \exp[-H(p^N, r^N)/k_B T] \quad (\text{II.27})$$

where the integration is over all possible variables of positions r and momenta p of particles in system. The probability density of the ensemble is described as below:

where k_B is Boltzmann's constant, T is the temperature, H is the Hamiltonian and Z is the sum of all possible microscopic properties of the corresponding ensemble, called partition function.

$$Z = \int \int dp^N dr^N \exp[-H(p^N, r^N)/k_B T] \quad (\text{II.28})$$

All possible states of the system must be calculated in order to solve above integral. In molecular dynamic simulations, it is essential to invoke ergodic hypothesis which states that ensemble averages equal to time averages. This allows MD simulation to determine the time average of ensemble:

$$\langle \Omega \rangle_t = \frac{1}{M} \sum_{t=1}^M \Omega(p^N, r^N) \quad (\text{II.29})$$

where t is the MD simulation time, M is the number of time steps in a simulation.

3.3 Modeling properties

3.3.1 Radial distribution function

The radial distribution function is an important statistic to characterize the local structure of simulated system by measuring the probability of finding a particle at a distance of r away from a given reference distance (or particle).

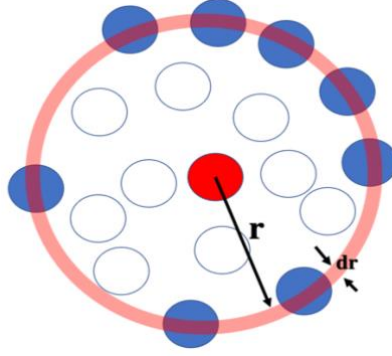


Figure II.1]. Space discretization for the evaluation of the radial distribution function.

Considering a homogeneous atomic system as illustrated in **Figure II.1**, where the red particle is the reference, and the blue particles on the orange circular sampling shell are the particles resided within the sampling shell. The number of particle pairs at a distance between r and $r + dr$ is thus obtained:

$$n(r) = \frac{N(N-1)}{V} dV \quad (\text{II.30})$$

where $\frac{N(N-1)}{V}$ is the number of particle pairs per system volume; dV is the volume of the sampling shell:

$$dV = \frac{4}{3}\pi(r+dr)^3 - \frac{4}{3}\pi r^3 = 4\pi r^2 dr \quad (\text{II.31})$$

Therefore, in the context of AIMD simulation, for a number of trajectories interested, the radial distribution function for each trajectory is calculated and then averaged:

$$g(r) = \frac{\sum_{traj} d(r)}{N_{traj} n(r)} = \frac{V}{4\pi N_{traj} N(N-1) r^2 dr} \sum_{traj} \sum_i \sum_{j \neq i} d(r - r_{ij}) \quad (\text{II.32})$$

where N_{traj} is the number of trajectory and r_{ij} is the distance between atom i and j at the given trajectory.

3.3.2 Probability distribution function relative to center of mass

In this thesis, to provide structural information (e.g., geometric arrangements) of trajectories extracted from different AIMD simulation frames, we constructed a probability distribution function by counting the number of atoms (occurrences) whose distances relative to the mass center of the studied system fall inside the infinitesimal interval $[r, r + dr]$:

$$P(r_i) = \frac{\sum N_{r_i}}{N}, \text{ with } r_i = \begin{cases} 1, & \text{if } r = dr \\ 0, & \text{otherwise} \end{cases} \quad (\text{II.33})$$

where N is the total number of atoms in the system and r_i is the distance of atom i related to the mass center of the system.

4. Thermodynamic model of gas adsorption

When the nanoparticle is under reactive gas environment, the adsorption behavior of gas on the nanoparticle surfaces is usually described by isotherms, which are a function of the gas pressure at given temperature. Among them, the Langmuir adsorption model [15] is the most important theory which assumes that adsorbates behave as ideal gas adsorbed on a homogeneous surface, therefore the interparticle interactions of gas are neglected and adsorbed on a perfect flat plane where all adsorption sites are energetically identical, and each site can only adsorb one atom or molecule (mono-layer coverage only). This famous Langmuir adsorption isotherm is given by:

$$\theta = \frac{KP}{1+KP} \text{ (or } PK = \frac{\theta}{1-\theta}) \quad \text{with } K = \exp\left(-\frac{\Delta G}{k_b T}\right) \quad (\text{II.34})$$

where the θ is the coverage of adsorbates on surfaces sites, P is the partial pressure of adsorbates and K is the Langmuir isotherm constant. The ΔG is the heat adsorption, k_b is the Boltzmann constant and T is the temperature. The Langmuir isotherm established the fundamental equation

for describing the adsorption and has been applied in many studies of adsorption thermodynamics. However, the lateral interaction between adsorbates which may greatly influence the overall adsorption behaviors is not taken into consideration in this model. In this thesis, an extended model of Langmuir called Fowler-Guggenheim (F-G) adsorption model [16] is thus selected to incorporate the lateral interactions:

$$PK = \frac{\theta}{1-\theta} e^{-c\theta} \quad \text{where: } c = \frac{zw}{RT} \quad (\text{II.35})$$

where R is the gas constant, z is the number of the nearest neighbors of each adsorption site of surface layer (the gas is assumed not to penetrate into the sublayers), and w is lateral interaction between adsorbed molecules. K is the F-G equilibrium constant:

$$K = \exp\left(-\frac{\Delta G}{RT}\right) = \exp\left(-\frac{E_{ads} - T(S_{ads} - S_{gas})}{RT}\right) \quad (\text{II.36})$$

where S_{ads} is the entropy of adsorbed gas molecule, and S_{gas} is the entropy of gas-phase molecule, which is expressed as:

$$S_{gas} = S_{gas}(T, P^0) - R \ln\left(\frac{P}{P^0}\right) \quad (\text{II.37})$$

where the $S_{gas}(T, P^0)$ is the gas entropy at 1 atmosphere pressure P^0 as function of temperature T , which is fitted based on the *NIST-JANAF Thermochemical Tables* [17] database.

Lateral Interaction (zw)

The F-G isotherm assumes the gas adsorption linearly varies with gas coverage (θ) on surface, thus the effective adsorption energy (E_{ads}^{eff}) with gas coverage θ is expressed as:

$$E_{ads}^{eff} = E_{ads}^{hkl} - zw \cdot \theta \quad (\text{II.38})$$

and the lateral interaction term (zw), in this thesis, is evaluated as the adsorption energy difference between full adsorbates coverage ($\theta=1$) and extremely low adsorbates coverage where the lateral interaction between adsorbates is negligible ($\theta=0$):

$$zw = E_{ads(\theta=0)}^{eff} - E_{ads(\theta=1)}^{eff} \quad (\text{II.39})$$

$E_{ads(\theta=0)}^{eff}$ is adsorption energy calculated with the adsorbates isolated on the surface and far enough from each other, and $E_{ads(\theta=1)}^{eff}$ is calculated with one monolayer of adsorbate coverage on surface. Thus, a positive zw represents attractive interaction between adsorbed molecules and negative value indicates repulsive interaction.

To notice that the adsorption energies calculated in this thesis are computed with respect of following expression:

$$E_{ads}^{hkl} = E_{slab+adsorbate}^{hkl} - E_{hkl}^{slab} - E_{adsorbate} \quad (\text{II.40})$$

where $E_{slab+adsorbate}^{hkl}$ is energy of the adsorbates, E_{hkl}^{slab} is energy of the slab model, $E_{adsorbate}$ is energy of free gas molecule and hkl is the corresponding plane facet. According to this equation, a positive value represents unfavorable gas adsorption on the surface and negative value means favorable adsorption.

5. Environmental construction model of nanoparticles

In general, the size of active nanoparticles in catalysis ranges between 1 to 100 nm containing between few atoms to several ten thousand of atoms. Despite the recent huge improvement of modern computational quantum mechanical modelling methods, the quantum simulation of systems with more than few hundred of atoms remains infeasible. One way to overcome this obstacle is to use DFT-based Wulff construction method. Indeed, based on one of the most popular models to construct nanoparticles of thousands of atoms, this approach provides fast and reliable way to predict the shape of larger sized nanoparticles without solving complex mathematical problems.

5.1 Wulff construction under vacuum

The Wulff theorem [18] states that the distance (d_{hkl}) from the center of crystal to the plane facet (hkl) is proportional to its respective surface energy (γ_{hkl}). Based on this principle, the shape of an equilibrium crystal under vacuum can be constructed by searching the minimum surface energy of each surface:

$$d_{hkl} = \lambda \gamma_{hkl} \quad (\text{II.41})$$

The general procedure to construct the equilibrium shape of nanoparticle under vacuum is as follows: (i) chose a center point, O; (ii) draw a plane that is normal to the γ_{hkl} from this center point at the distance of $d_{hkl} = \lambda \gamma_{hkl}$, where λ is a given constant; (iii) repeat for all planes; (iv) the space confined inside of all the planes is the equilibrium shape of the nanoparticle. (See **Figure II.2**)

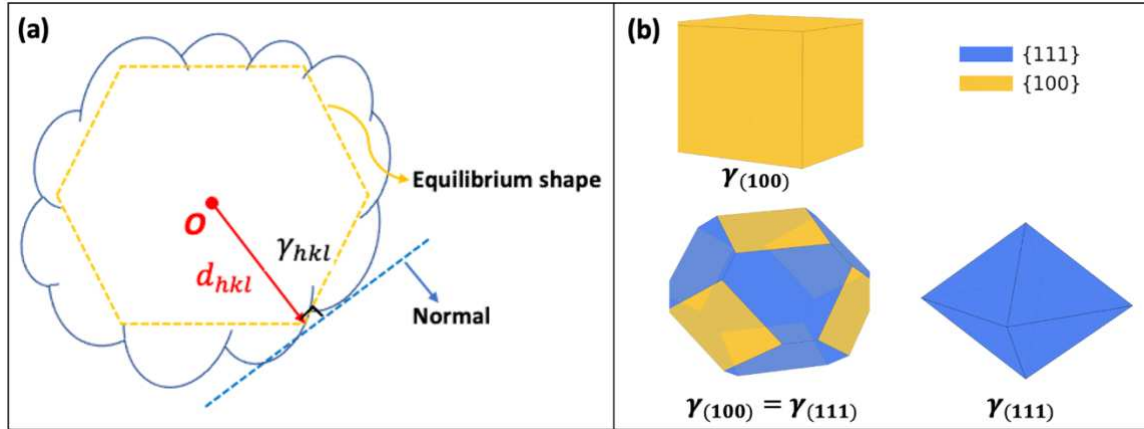


Figure II.2]. Wulff Construction Scheme. (a) Schematic illustrations of Wulff construction. (b) Examples of equilibrium shapes constructed from Wulff theorem.

5.2 Construction of environmental nanoparticle models

When crystal interacts with a reactive gas environment, its surface energy can be corrected into interface tension, γ_{hkl}^{int} , that includes the term of the coverage of adsorbates (θ):

$$\gamma_{hkl}^{int} = \gamma_{hkl} + \theta \left(\frac{E_{ads}^{hkl}}{A} \right) \quad (\text{II.42})$$

where A is the surface area per atom, and E_{ads}^{hkl} is the gas adsorption energy on the surface. If coupled with the F-G isotherm, that account for the lateral interaction, the interface tension is then revised as:

$$\gamma_{hkl}^{int} = \gamma_{hkl} + \theta \left(\frac{E_{ads}^{hkl} - zw\theta}{A} \right) \quad (\text{II.43})$$

Conventionally, the γ_{hkl} can be determined with following expression by establishing slab models of targeting facet (hkl):

$$\gamma_{hkl} = \frac{E_{hkl}^{slab} - N \cdot E_{bulk}}{2A} \quad (\text{II.44})$$

where the E_{hkl}^{slab} is the total energy of the slab of respective facets (hkl), E_{bulk} is the energy per atom of the bulk, N is the number of atoms of the slab, and the factor of 2 in the denominator accounts for the two surface sides in this slab model.

5.3 Average surface coordination number

In crystallography, the coordination number (CN) of an atom is defined as the number of its immediate surrounding neighbors. In this manuscript, in order to identify the different shapes of NP constructed, we define a new descriptor named average coordination number (\overline{CN}) which is obtained by calculating the total CN of all the atoms that located on surface then takes its average value:

$$\overline{CN} = \frac{\sum_{i=1}^{N_{surf}} CN_i}{N_{surf}} \quad (\text{II.45})$$

where CN_i is the surface coordination number of i^{th} atom, and N_{surf} is the number of atoms located on the surface of constructed nanoparticles. Each \overline{CN} value that satisfies $\overline{CN} > 0.1$ represents a new NP shape.

Reference

1. Hartree, D. R., The Wave Mechanics of an Atom with a Non-Coulomb Central Field. Part II. Some Results and Discussion. *Mathematical Proceedings of the Cambridge Philosophical Society* **2008**, *24*, 111-132.
2. Fock, V. A., Näherungsmethode Zur Lösung Des Quantenmechanischen Mehrkörperproblems. *Zeitschrift für Physik* **1930**, *61*, 126-148.
3. Shikano, Y.; Watanabe, H. C.; Nakanishi, K. M.; Ohnishi, Y.-y., Post-Hartree–Fock Method in Quantum Chemistry for Quantum Computer. *The European Physical Journal Special Topics* **2021**, *230*, 1037-1051.
4. Cramer, C. J.; Truhlar, D. G., Density Functional Theory for Transition Metals and Transition Metal Chemistry. *Physical Chemistry Chemical Physics* **2009**, *11*, 10757-10816.
5. Hohenberg, P.; Kohn, W., Inhomogeneous Electron Gas. *Physical Review* **1964**, *136*, B864-B871.
6. Hohenberg, P.; Kohn, W., Inhomogeneous Electron Gas. *Physical Review* **1964**, *136*, 864-871.
7. Kohn, W.; Sham, L. J., Self-Consistent Equations Including Exchange and Correlation Effects. *Physical Review* **1965**, *140*, 1133-&.
8. John, P. P. a. Y. W., Accurate and Simple Analytic Representation of the Electron-Gas Correlation Energy. *Physical Review B* **1992**, *45*, 13244-13249.
9. Peter, E. B. a. O. J. a. O. K. A., Improved Tetrahedron Method Far Brillouin-Zone Integrations. *Physical Review B* **1994**, *49*, 16223-16233.
10. Bloch, F., Über Die Quantenmechanik Der Elektronen in Kristallgittern. *Zeitschrift für Physik* **1929**, *52*, 555-600.
11. Monkhorst, H. J.; Pack, J. D., Special Points for Brillouin-Zone Integrations. *Physical Review B* **1976**, *13*, 5188-5192.
12. Grimme, S., Accurate Description of Van Der Waals Complexes by Density Functional Theory Including Empirical Corrections. *Journal of Computational Chemistry* **2004**, *25*, 1463-1473.
13. Zimmerli, U.; Parrinello, M.; Koumoutsakos, P., Dispersion Corrections to Density Functionals for Water Aromatic Interactions. *The Journal of Chemical Physics* **2004**, *120*, 2693-2699.
14. Von Lilienfeld, O. A.; Tavernelli, I.; Rothlisberger, U.; Sebastiani, D., Optimization of Effective Atom Centered Potentials for London Dispersion Forces in Density Functional Theory. *Physical Review Letters* **2004**, *93*, 153004.
15. Langmuir, I., The Adsorption of Gases on Plane Surfaces of Glass, Mica and Platinum. *Journal of the American Chemical Society* **1918**, *40*, 1361-1403.
16. Fowler, R. H.; Guggenheim, E. A., Statistical Thermodynamics. Cambridge University Press: Cambridge: 1939.
17. Chase, M. W.; Davies, C. A.; R., D. J.; Frurip, D. J.; McDonald, R. A.; Syverud, A. N., Nist-Janaf Thermochemical Tables. In <https://janaf.nist.gov/>, 1999.
18. Wulff, G., Xxv. Zur Frage Der Geschwindigkeit Des Wachstums Und Der Auflösung Der Krystallflächen. *Zeitschrift für Kristallographie - Crystalline Materials* **1901**, *34*, 449.

Chapter III

Modeling Pt nanoparticles under hydrogen media

1. Introduction

Platinum nano-sized metal particles (Pt-NPs) have diverse applications, especially in heterogeneous catalysis and electro-catalysis [1-4]. In the last decade, several theoretical works have been devoted to the characterization and the understanding of the unique catalytic properties of this material [5-8]. Among known features, it appears that the high activity and unique selectivity of Pt catalysts are generally size- and shape-dependent [9-13]. Moreover, several *in-situ* experimental observations provide evidence for drastic shape evolutions of Pt-NP catalysts in reactive gas environment [14-17]. For example, Roldan Cuenya *et al.*[14] reported that differences in the catalytic performance of Pt nanoparticles toward the oxidation reaction of 2-propanol are observed for samples with similar average TEM diameter but exhibiting different shapes. This difference was explained as the result of the so-called geometric effects, where under-coordinated Pt atoms at the NP surface are the operating active catalytic sites [18-20]. This exemplary result shows how the identification of the precise shape of Pt-NPs at a given temperature and pressure is a crucial step as the catalytic properties may be dependent [14, 21].

The present chapter reviews the above-mentioned problematic of shape evolution and the approaches to predict those of Pt-NPs by using accurate theoretical methods that might account

for the effect of the adsorption of hydrogen gas. We choose the hydrogen as it is ubiquitous in many reactions catalyzed by Pt nanocatalysts. Regarding the theoretical approach, and as discussed in the first chapter, the choice is dictated by the targeted properties and always depends on the size limitation. In this work, two different theoretical approaches are applied to investigate the structure evolutions of Pt-NPs under hydrogen pressure at different temperatures and for different sizes. For “large sized Pt-NPs” (larger than 5 nm), a multiscale structure reconstruction model (MSR) combines the energetic parameters issued from density functional theory (DFT) with thermodynamics using Fowler-Guggenheim adsorption theorem. Then geometric construction of the Pt-NPs is obtained using Wulff construction method (see detailed methodology in **Chapter 2**). The results provide equilibrium Pt-NP shapes for large range of temperature and hydrogen pressure and show shape evolutions well consistent with the experimental ones. Moreover, the governing factors responsible for morphology changes are discussed. Then, to study the dynamic changes of “small sized Pt-NPs” (~1.8 nm) covered by hydrogen atoms, we used *ab-initio* molecular dynamics simulations (AIMD). The Pt and hydrogen motions and diffusions are explored under $T = 500\text{ K}$. Finally, comparison between the two theoretical methods, a discussion of the limitation of the respective approaches and perspectives are proposed.

2. Methods and computational details

2.1 Multiscale structure reconstruction (MSR) approach

DFT calculations

As explained in **Chapter 2**, to construct the equilibrium nanoparticle shape in hydrogen environment by combining environmental Wulff model and F-G isotherm, the surface energy γ_{hkl} , the lateral interaction w and the hydrogen coverage-dependent adsorption energy E_{ads}^{hkl} are

prerequisite parameters. All those parameters are calculated using spin-unrestricted density functional theory (DFT) implemented in the Vienna Ab-initio Simulation Package (VASP) and the Perdew, Burke, and Ernzerhof (PBE) functional [22]. The valence electrons were treated explicitly, and their interactions with the ionic cores were described by the projector augmented-wave method, which allows the use of a low cut-off energy equals to 400 eV for the plane-wave basis.

Slab construction

To construct Pt-NP, three low index surfaces: Pt(1 1 1), Pt(1 0 0) and Pt(1 1 0) were considered, as they represent the most dominant surfaces of stable metallic nanoparticles. Two sizes of Pt unit cells for selected facets (*hkl*) were constructed: (3 × 3) and (1 × 1) unit cells, which are both separated by 15 Å of vacuum space containing 6 atomic layers from which the bottom two layers are fixed on the bulk atom positions. The Brillouin zone integrations are performed with a Monkhorst-Pack (3 × 3 × 1) *k*-point mesh for the (3 × 3) unit cells and (6 × 6 × 1) *k*-point mesh for the (1 × 1) unit cells. The *k*-point mesh for the Pt-bulk metal optimization is (11 × 11 × 11). To calculate the adsorption energy on each surface facet E_{ads}^{hkl} , the hydrogen may show different stabilities at different adsorption sites. Consequently, all possible adsorption sites (top site, bridge site, hollow site and fcc site, etc. (see **Figure III.1**)) of hydrogen have been considered using DFT geometry optimizations on (3 × 3) slab models. The stable configurations considered in this work correspond to the configurations with the most favorable adsorption sites which are the FCC site for Pt(1 1 1), and bridge site for Pt(1 0 0) and Pt(1 1 0), (see **Table SI-III.1**).

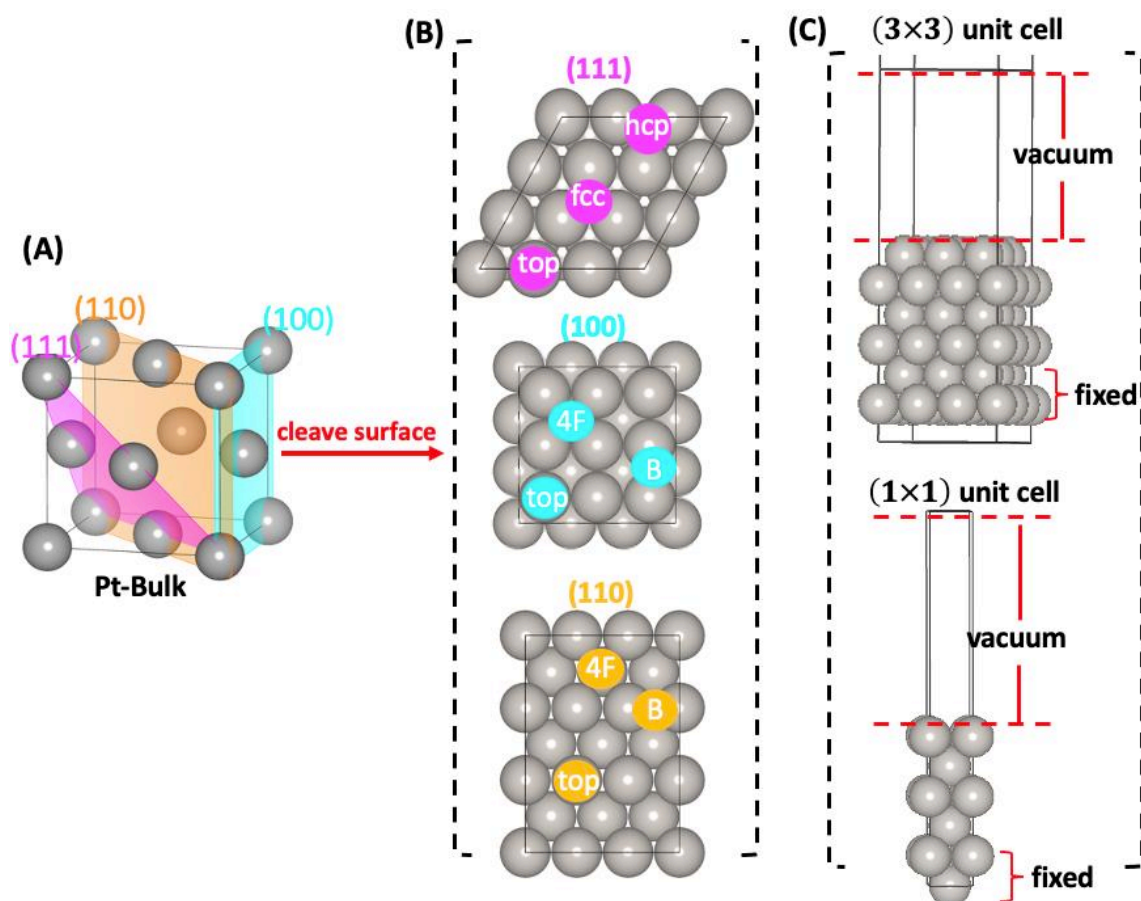


Figure III.1 Constructed slab models in MSR model. (A) Face centered cubic (FCC) structure of Pt-bulk. (B) Top view of (3×3) unit cell slab models for $(1\ 1\ 1)$, $(1\ 0\ 0)$ and $(1\ 1\ 0)$ cleaved from Pt-bulk structure and illustrations of different adsorption sites of hydrogen on different facets calculated in this work. 4F means 4-fold hollow adsorption site, B means bridge adsorption site. (C) Side view of (3×3) unit cell slab model and (1×1) unit cell slab model, the atoms located in bottom two layers are fixed, unit cells are separated by a $15\ \text{\AA}$ vacuum.

Descriptors for the identification of Constructed Pt-NPs

The surface average coordination number \overline{CN} (see detailed explanation in **Chapter 2**) is used as descriptor for identifying the different constructed Pt-NPs. We denote Pt-NP_ \overline{CN}_n as the average coordination number of each Pt-NP with n corresponding to the calculated surface average coordination number. For example, Pt-NP_ \overline{CN}_9 represents a NP which is mainly

formed by (1 1 1) facets. Knowing that \overline{CN} for (1 1 1) is 9, and Pt-NP_ \overline{CN}_8 will be a NP with mainly (1 0 0) facet.

2.2 *Ab initio* molecular dynamics approach

Pt-nanoparticle model

Platinum is an fcc (face-centred cubic) metal, for which the relaxed surface energies are generally found in the order of $\gamma_{(111)} < \gamma_{(100)} < \gamma_{(110)}$ [23]. This order being that for Pt-NP in its thermodynamically stable structure, the surfaces are mainly composed by the most stable compact facets (1 1 1) and (1 0 0), which results in a stable fcc structure called “truncated octahedral (TOh). Such TOh shape has been reported by many experimental and theoretical works as the most typical shape of fcc-metallic nanoparticles under vacuum [24-27]. In addition, our results from MSR simulations (see Results section) also confirm that the equilibrium shape for Pt-NP under vacuum is in a TOh shape.

Under the above considerations, a TOh Pt nanoparticle model of 1.8 nm size cut from its fcc bulk metal containing 201 atoms (denoted as TOh_Pt₂₀₁) is chosen for running AIMD simulations of the “small-sized Pt-NP”. The selected size offers a good compromise between computational time and theoretical level of accuracy for both DFT geometry optimizations and AIMD simulations. As shown in **Figure III.2**, the constructed TOh Pt-NP is composed of (1 1 1) facets in hexagon and (1 0 0) facets in cube, with a total of 122 atoms exposed to the surface. Then, to study the hydrogen adsorption behavior on TOh_Pt₂₀₁, 122 hydrogen atoms were adsorbed on the surface which represents a hydrogen coverage of 1 ML. The adsorption sites of hydrogen were selected to be the fcc site on the (1 1 1) facet and the bridge site on the (1 0 0) facet. These adsorption sites are found to be the most stable on these surfaces (see **Table SI-III.1**). The fully hydrogen covered Pt-NP is named hereafter as TOh_Pt₂₀₁H₁₂₂. To start, both

models were pre-optimized using DFT at 0 K to reach their local minimum energies, then were used as initial stable Pt-NPs configurations for AIMD simulations at 500 K for at least 30-ps simulation time to assure reaching the equilibrium configurations.

Ab-Initio Molecular Dynamics Simulations

Ab-initio molecular dynamic simulations (AIMD) invoking Born-Oppenheimer approximation were carried out in the canonical (NVT) ensemble employing Nosé-Hoover thermostats with a time step of 1.5-fs at 500 K. This temperature is chosen as it is the most common used to investigate catalytic systems. The hydrogen free and hydrogen covered Pt TOh NPs were modelled using an orthorhombic periodic cell of dimensions $30\text{\AA} \times 30\text{\AA} \times 30\text{\AA}$, which is big enough to avoid interactions between neighboring periodic images. All AIMD simulations were conducted using Vienna Ab-initio Simulation Package (VASP). Atomic forces were estimated using DFT calculations with the Perdew, Burke, and Ernzerhof (PBE) [22] exchange-correlation functional. The valence electrons were treated explicitly, and their interactions with the ionic cores were described by the projector augmented-wave method, which allows the use of a low cut-off energy equals to 400 eV for the plane-wave basis. The convergence criterion for optimization of the wave function was set to 10^{-4} .

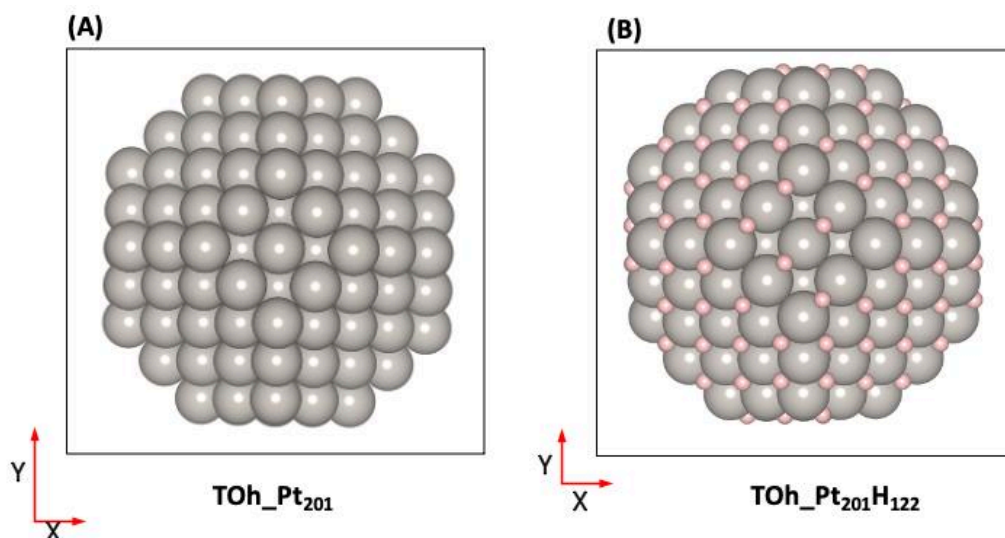


Figure III.2]. Ab-initio molecular dynamics (AIMD) simulations configurations projecting on xy -plane: (A) Pt-NPs under vacuum (TOh_Pt₂₀₁); (B) Pt-NPs with 122 hydrogen atoms adsorbed on surface (TOh_Pt₂₀₁H₁₂₂). (grey, platinum atoms; pink, hydrogen atoms). The adsorption sites of hydrogen are the fcc sites on the (1 1 1) facet and the bridge site of the (1 0 0) facet. These sites are the most favorable adsorption sites of hydrogen on each facet.

3. Results

3.1 Modeling equilibrium shape of Pt-NPs under hydrogen condition using MSR model

Table III.1 represents all DFT calculated parameters needed for the MSR construction. As expected, under vacuum, the calculated surface energies of Pt surfaces are found to respect the order of $\gamma_{(111)} < \gamma_{(100)} < \gamma_{(110)}$, which is in full agreement with the literature [28-29]. The most stable calculated hydrogen adsorption energies show that hydrogen strongly adsorbs on the (1 0 0) facet and then on the (1 1 0) and (1 1 1) facets. For the (1 1 1) surface, the fcc site is the most favorable adsorption site (-0.70 eV) and on the (1 0 0) and the (1 1 0) facets it is the bridge site (-0.84 eV and -0.75 eV, respectively). The difference in adsorption energies between the bridge and the fcc sites varies from 0.05 eV to 0.14 eV. This preference order of hydrogen to Pt facets are also in good agreement with many previously reported studies [30-32]. To study

the lateral interaction between adsorbates (hydrogen), we computed the evolution of the adsorption energy with increasing coverage on each Pt surface. The results show the much stronger repulsive H-H lateral interaction (negative values represent for repulsive-interaction, see detailed explanation in **Chapter 2**) on facet Pt(1 1 1) (-0.13 eV) than on Pt(1 0 0) (-0.063 eV). On Pt(1 1 0) the lateral interaction is found to be negligible, which is in agreement with the literature [33].

Table III.1 | All DFT calculated pre-requisite parameters for MSR construction. Adsorption energies E_{ads}^{hkl} , surface energy γ_{hkl} , lateral interaction z^w and atomic area A of Pt calculated by DFT.

Pt	(a) E_{ads}^{hkl} (eV)	z^w (eV)	γ_{hkl} (eV/Å ²)	A (Å ²)
(111)	-0.70	-0.13	0.098	6.85
(100)	-0.84	-0.063	0.12	7.91
(110)	-0.758	0	0.13	11.18

(a) The E_{ads}^{hkl} represents the adsorption energies over the most stable hydrogen adsorption site for each facet.

With the pre-requisite parameters ready-in-hand, we modeled, the shape evolutions of Pt-NPs of size around 5 nm containing about 24000 Pt atoms for temperature changing between 200 and 1200 K, while the hydrogen pressure varies from 1 to 10⁵ Pa (1 bar). These temperature and gas pressure ranges may cover most experimental conditions. The individual modeled structures are denoted as Pt-NP_ \overline{CN}_n (see definition of \overline{CN} in method section).

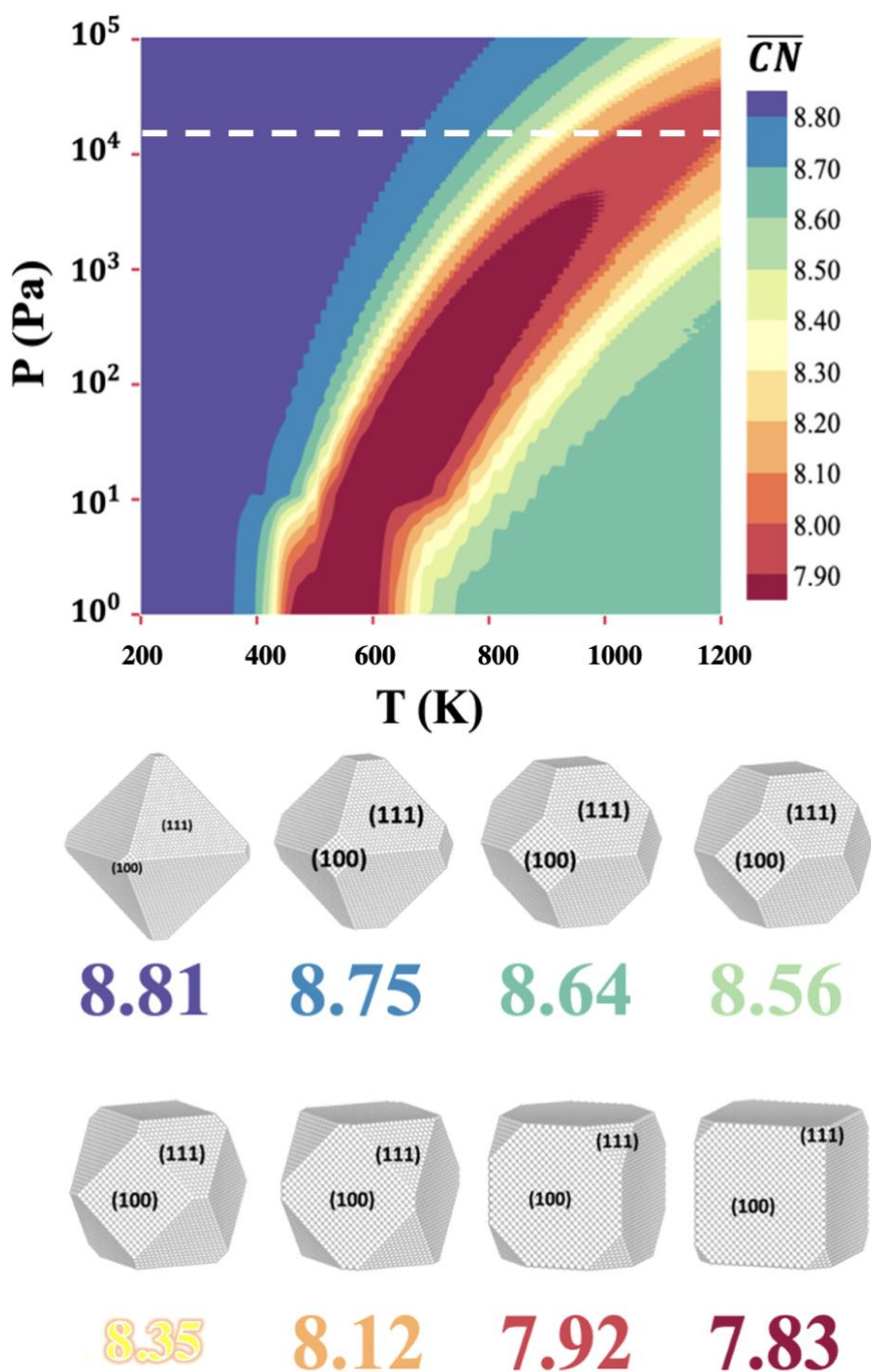


Figure III.3 Multiscale Structure Reconstruction (MSR) constructed Pt-NP $_{\overline{CN}_n}$ under hydrogen environment. The Pt-NP shapes with size of 5 nm as functions of temperatures and hydrogen pressures (left subfigure), wherein each color represents one different \overline{CN} value which is labeled with different colors. Subfigure on the right shows the full sets of color-coded Pt-NP $_{\overline{CN}_n}$ structures constructed.

In **Figure III.3**, the contour plot shows the different Pt-NP structures constructed with MSR model as a function of temperature and hydrogen pressures identified by the different \overline{CN} values and coded with different colors. Thus, the dark red represents the smallest average coordination number and the purple color indicates the highest average coordination number. In the whole modeling (T, p)-range, the Pt-NP shape (\overline{CN} values) is found to change between Pt-NP_ $\overline{CN}_{7.83}$ (cube-like) and Pt-NP_ $\overline{CN}_{8.81}$ (octahedron-like), reflecting the increase/decrease of the fraction of (1 1 1)/(1 0 0) facet on the Pt-NP surface, respectively. Based on the contour plot, the evolution manner of Pt-NP shapes can be summarized into two modes:

(i) For hydrogen pressure above 10^4 Pa (marked in white dashed line, **Figure III.3**), the Pt-NP shape evolves progressively from near-perfect octahedron shape (Pt-NP_ $\overline{CN}_{8.81}$) to the near-perfect cube (truncated cube) shape (Pt-NP_ $\overline{CN}_{7.92}$) when increasing the temperature. In this domain, the fraction of (1 0 0) facet increases from 5.5% to 90.7% and the fraction of (1 1 1) facet decreases from 94.2% to 9.3%, respectively.

(ii) Bellow hydrogen pressure of 10^4 Pa, the Pt-NPs are predicted to undergo reversible shape changes with increasing temperature. Indeed, firstly the Pt-NPs changes from near-perfect octahedron to the near-perfect cube shape, then the shapes start to reverse back and stabilize in the form of a truncated octahedral shape, Pt-NP_ $\overline{CN}_{8.64}$.

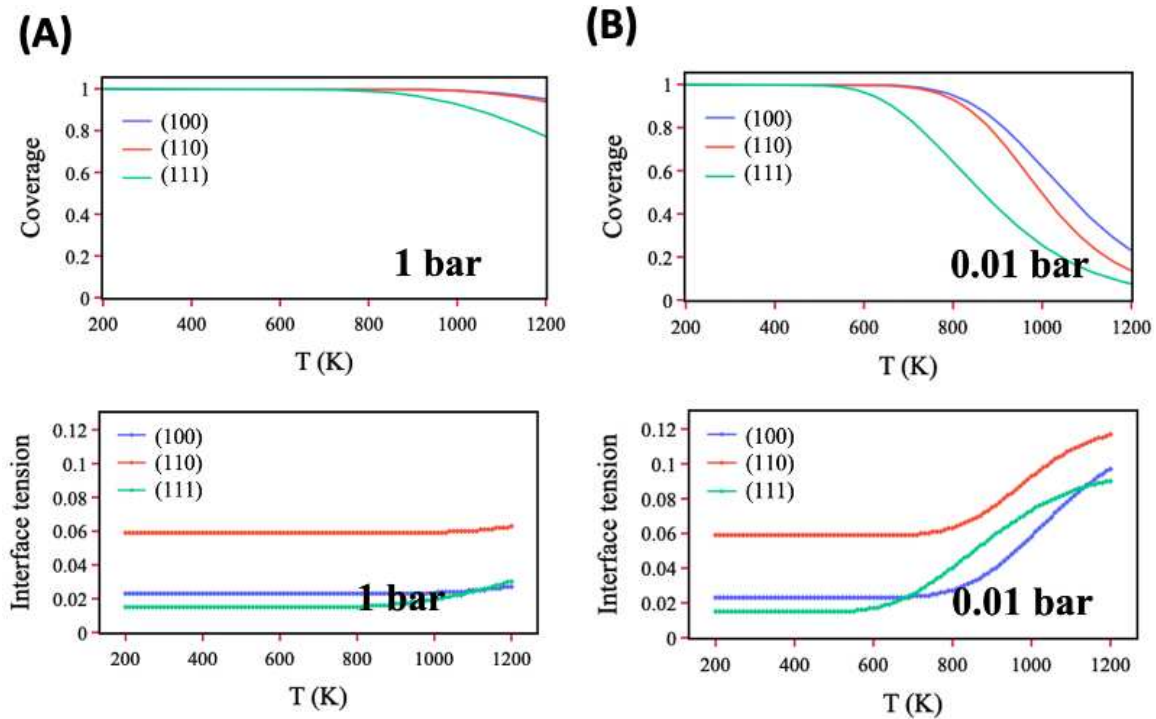


Figure III.4 | Hydrogen coverage and interface tension profiles of (1 1 1), (1 1 0) and (1 0 0) Pt-NP surfaces predicted by MSR model as functions of temperature (A) under 1 bar of hydrogen pressure. (B) under 0.01 bar of hydrogen pressure.

To understand the above dynamic changes especially the shape reversibility in the lower pressure area, the evolution of hydrogen coverage and the interface tension on each surface facet are computed as a function of temperature. In **Figure III.4** the results for two different hydrogen pressures, 1 and 0,01 bar are reported. As the morphology changes of NPs are governed by the interface stability of facets and their affinity with the gas environment, the analysis of the evolution of interface energies may provide information on the preferable equilibrium shape. To remind readers, the interface tension (**Chapter 2, equation II.43**) is the F-G adsorption isotherm-revised surface energy when NP is interacting with adsorbed hydrogen atoms, and thus this observable is (T, P, θ) -dependent. In **Figure III.4-A**, for Pt-NPs under 1 bar (10^5 Pa) of hydrogen pressure, the hydrogen coverage on (1 1 1), (1 1 0), and (1 0 0) facets are equally high at low temperature. This indicates that the surface (1 1 1) which has the lowest

interface tension will remain as the dominant facet of equilibrium Pt-NPs in this temperature region. Then with the increase of temperature above 1000 K, the H coverage on (1 1 1) facet starts to decrease while on the (1 0 0) and the (1 1 0) facets, the coverage barely decreases. This result is in line with the lower adsorption energy of hydrogen on (1 1 1) surface compared to the (1 0 0) and (1 1 0) ones. Consequently, the interface tension of (1 1 1) facet increases faster than that of (1 0 0) facet until it becomes higher, which results in the increase of the proportion of the (1 0 0) facet at the expense of the (1 1 1) facet. Under 0.01 bar (10^3 Pa) of hydrogen pressure (**Figure III.4-B**), the fraction of facet (1 1 1) is found to rapidly decrease for T above 600 K and reaches the range of 0.3-0.1 ML for T higher than 1100 K. In that range, the coverage of hydrogen on the three facets is almost equal. Considering the evolution of interface tension, the results show that the (1 0 0) facet becomes more stable than the (1 1 1) facet for temperature between 700 and 1100 K. This results in the re-enlargement of facet (1 0 0) and the diminution of facet (1 1 1). For temperature higher than 1100 K, a shape reversing of Pt-NP is observed.

To validate the above MSR predicted results on Pt-NP shapes in hydrogen condition, we searched for recent experimental results that may confirm these predicted shapes. It appears that the most common Pt-NPs structures observed/synthesized in the literature are composed of (1 1 1) and (1 0 0) facets manifesting in cubic, octahedral, truncated octahedral and tetrahedral shapes, etc. [34-37]. El-Sayed *et al.* [34-35] were the first that reported the synthesis of Pt-NPs in the shape of cube, tetrahedron and truncated octahedron through the H_2 gas flow as a reducing agent of K_2PtCl_4 in aqueous solutions wherein the shape of NPs is controlled by regulating the concentration of the capping agents. Moreover, dynamic changes of Pt-NP under hydrogen condition have been also observed in some experimental works [38-39]. For example, Duan *et al.* [38] have reported the *in-situ* Cs-corrected TEM images on the supported Pt-NPs with a diameter of approximately 5 nm and have shown that Pt-NP are mainly composed of (1 1 1)

and (1 0 0) planes. These authors also reported that at 473.15 K and hydrogen pressure of few mbar, the (1 1 1) surface is the main facet, while with temperature increasing to 773.15 K, a higher fraction of (1 0 0) facet was observed. All these observations are consistent with the MSR prediction results.

Let us note that for Pt-NP_ $\overline{CN}_{8.64}$ the structure is mainly composed of (1 1 1) and (1 0 0) surfaces. This TOh structure is found in the most high-temperature and low-pressure area (green region) which represents the equilibrium shape under vacuum. This stable truncated octahedral shape (TOH) was used as the nanoparticle model shape of our “small-sized Pt-NP modeling” using AIMD simulations.

3.2 AIMD simulation of small Pt clusters in presence of hydrogen

3.2.1 Pt-NP under vacuum

Our first AIMD simulation consisted of following the configurational trajectory of the bare TOh_Pt₂₀₁ NP at the temperature of 500 K. In **Figure III.5** are presented the potential energy evolving as a function of the simulation time as well as the temperature profile at NVT-ensemble. This figure shows that the TOh_Pt₂₀₁ system rapidly reaches its equilibration stage after 3-ps with stabilized potential energy and temperature varying around 500 ± 50 K. This stabilization is maintained until the end of the simulation. It can also be noticed that in the very beginning, during the first ~ 3 -ps simulation time, there is a sudden increase of the relative potential energy from 0 to over 20 eV. This observed artifact is an expected thermalization process for the initial configuration of TOH_Pt₂₀₁ (0 K) searching for its thermodynamically stable state (500 K). Such process is also accordingly manifested on the temperature profile (0-ps to ~ 3 -ps).

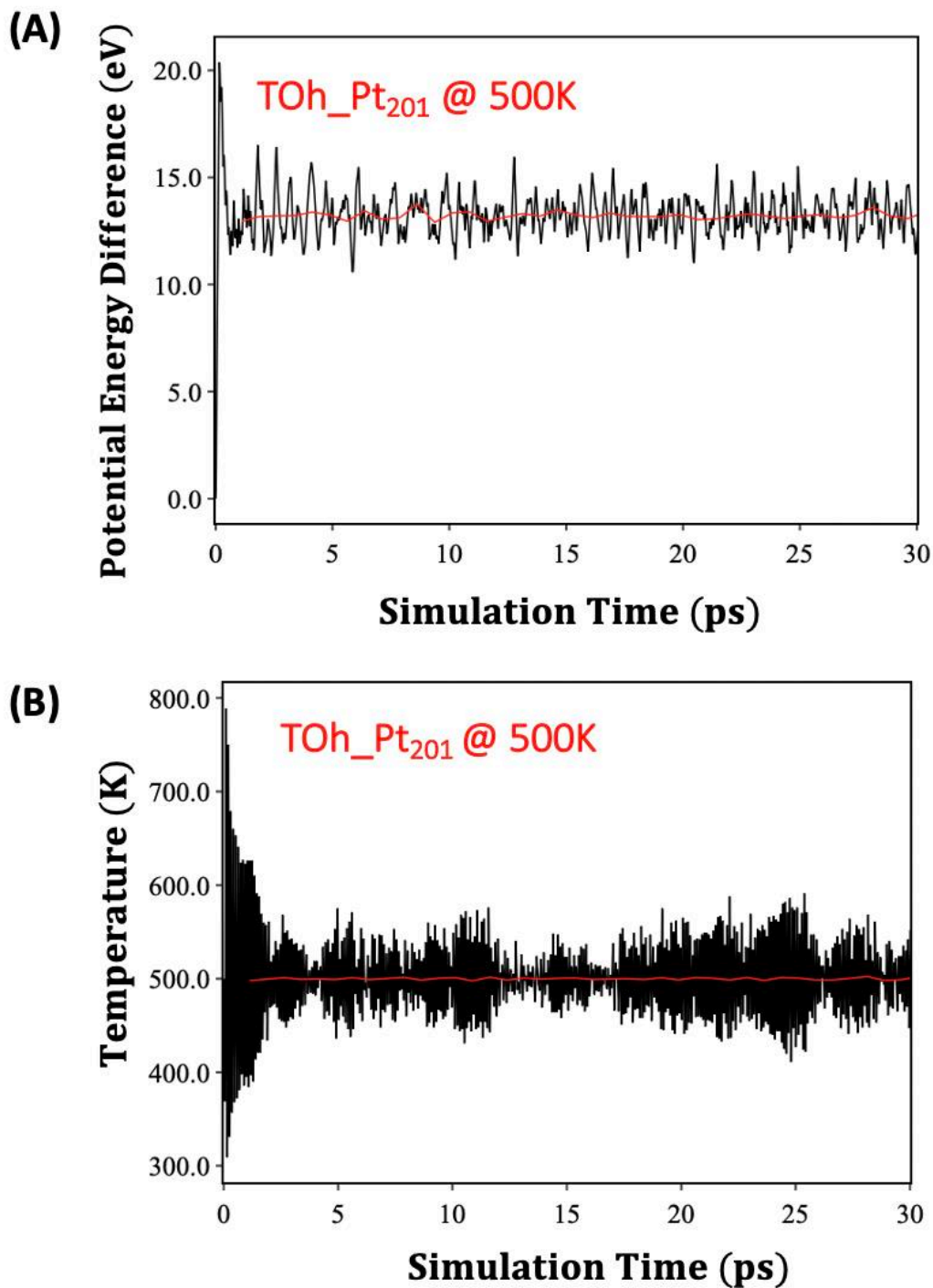


Figure III.5]. *Ab-initio* molecular dynamics (AIMD) simulations of TOh_Pt₂₀₁ (under vacuum) at 500 K. (A) Potential energy profiles of TOh_Pt₂₀₁ relating to the initial state for AIMD simulations at 500 K. (B) Temperature profile of TOh_Pt₂₀₁ during AIMD simulations at 500 K. The red curves are the fitted average values taken at each 0.5-ps of simulation time.

After 30-ps simulation time span, the final configuration (TOh_Pt₂₀₁@500 K) extracted from the last trajectory of AIMD simulations is compared with the initial TOh_Pt₂₀₁ structure (denoted as TOh_Pt₂₀₁@0 K). As illustrated in **Figure III.6**, the two configurations are identical.

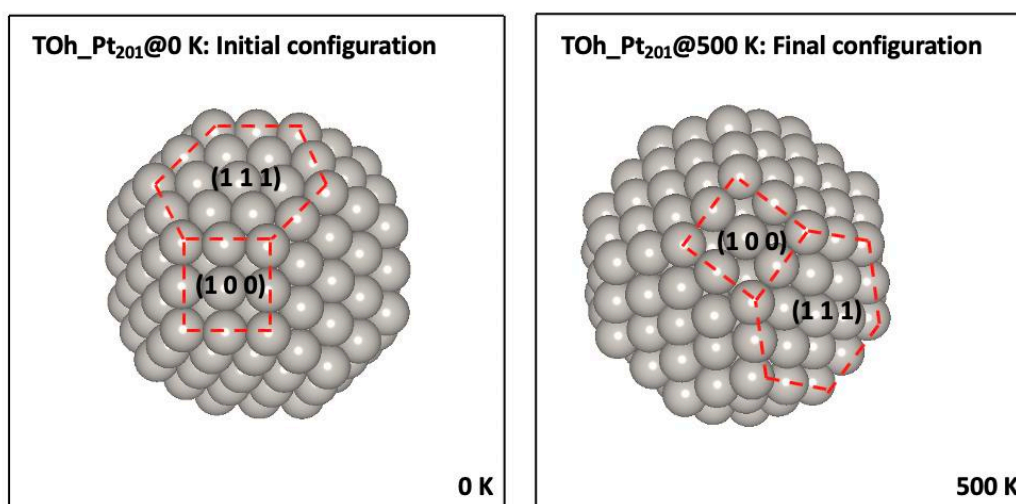


Figure III.6 | Illustration of (left side subfigure) the initial (DFT pre-optimized) Pt-NP shape under vacuum (TOh_Pt₂₀₁@0 K) and the final shape (right side subfigure) after AIMD simulations (TOh_Pt₂₀₁@500 K) under 500 K.

The well-preserved TOh shape structure during dynamics at 500 K is further confirmed by the analysis of the radial distribution function comparing the first-neighbor peaks between initial and final configurations. As it can be seen in **Figure III.7-A**, the first-neighbor peaks of “Pt-Pt” distance for both configurations are identically located at 2.75 Å. The second- and third-neighbor peaks of the two configurations are well overlapped.

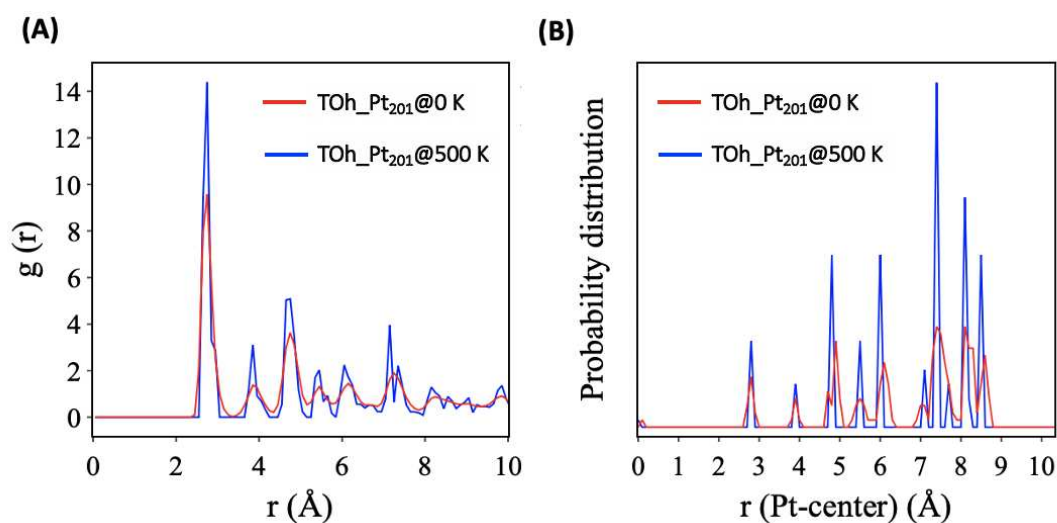


Figure III.7]. *Ab-initio* molecular dynamics (AIMD) simulations of TOh_Pt201 (under vacuum) at 500 K. (A) Radial distribution functions of initial TOh_Pt₂₀₁ structure (blue line) and the final structure (red line) between Pt-Pt pairs. (B) The probability distribution functions of the Pt atoms relative to the center of mass between the initial structure (blue line), and the final structure (red line). The well-defined peaks are signatures of fcc structure of a bare truncated octahedron Pt-NP. After AIMD simulations at 500 K, the Pt-NP shape is slightly disturbed but still maintains its fcc structure.

To complete the analysis, the calculation of distance distribution of Pt atoms relative to the mass center of the NP is depicted in **Figure III.7-B**. Except slight-disturbance on the long-range distances above 7 Å, the 3 peaks located at 2.8 Å, 3.9 ~ 6 Å and 7.1 ~ 8.5 Å signature of the well-defined fcc structure of the truncated octahedral-Pt-NP are found to remain well preserved comparing to the initial configuration.

3.2.2 Pt-NP in presence of hydrogen

After the simulation of bare TOh₂₀₁ Pt-NP, we considered the hydrogen covered Pt-NP (TOh_Pt₂₀₁H₁₂₂) and we performed AIMD simulations. Before that, the hydrogenated Pt-NP was pre-optimized by DFT and the optimized Pt-NP (denoted as TOh_Pt₂₀₁H₁₂₂@0 K) shows that the TOh shape is fully preserved, see **Figure III.8**. The hydrogen adsorption energy is -0.49 eV

indicating a strong H-Pt binding. This value is in agreement with the experimentally calculated heat of chemisorption, generally reported to be between 30 and 60 $\text{kJ}\cdot\text{mol}^{-1}$ [40]. The time evolutions of relative-potential energy and temperature stabilization of TOh_Pt₂₀₁H₁₂₂, are presented in **Figure III.9**. It can be seen that the thermal equilibration is quickly reached only after ~ 3 -ps of simulation time, similarly as the simulations on the TOh_Pt₂₀₁ under vacuum.

There are no noticeable changes observed following the configurational evolution of AIMD simulation of TOh_Pt₂₀₁H₁₂₂ under 500 K during the 30-ps of simulating time. Indeed, the final structure (TOh_Pt₂₀₁H₁₂₂@500 K, see **Figure III.8**) of Pt-NP keeps its TOh shape where hydrogens moving over the surface are mainly located on the bridge sites of (1 0 0) facets, partially on the top and on the fcc sites of (1 1 1) facets and on the edges.

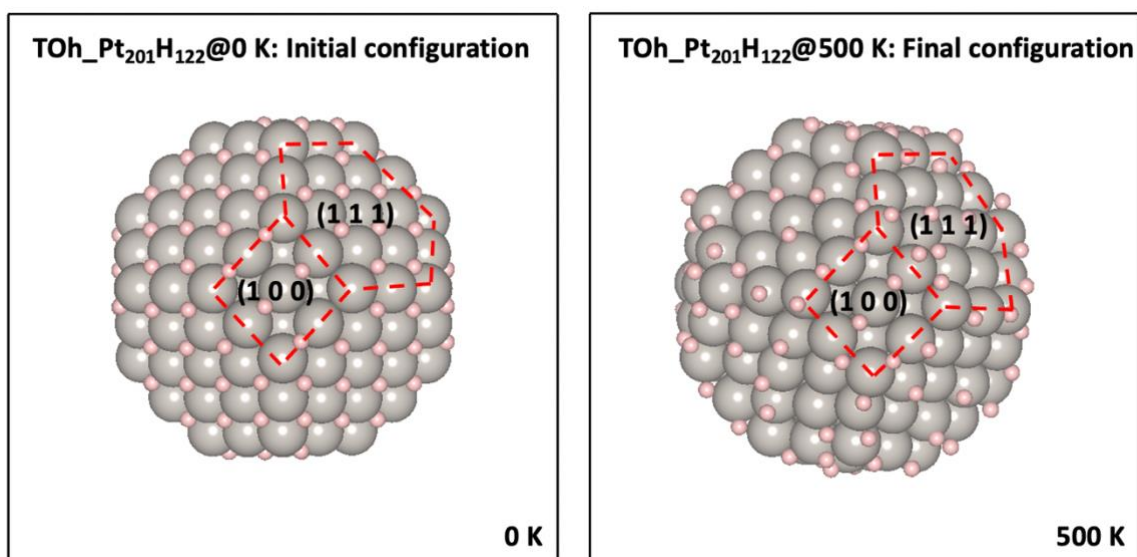


Figure III.8 | Illustration of (left side subfigure) the initial (DFT pre-optimized) Pt-NP shape with 1 ML of atomic hydrogen coverage (TOh_Pt₂₀₁H₁₂₂@0 K) and the final shape (right side subfigure) after AIMD simulations (TOh_Pt₂₀₁H₁₂₂@500K) under 500 K.

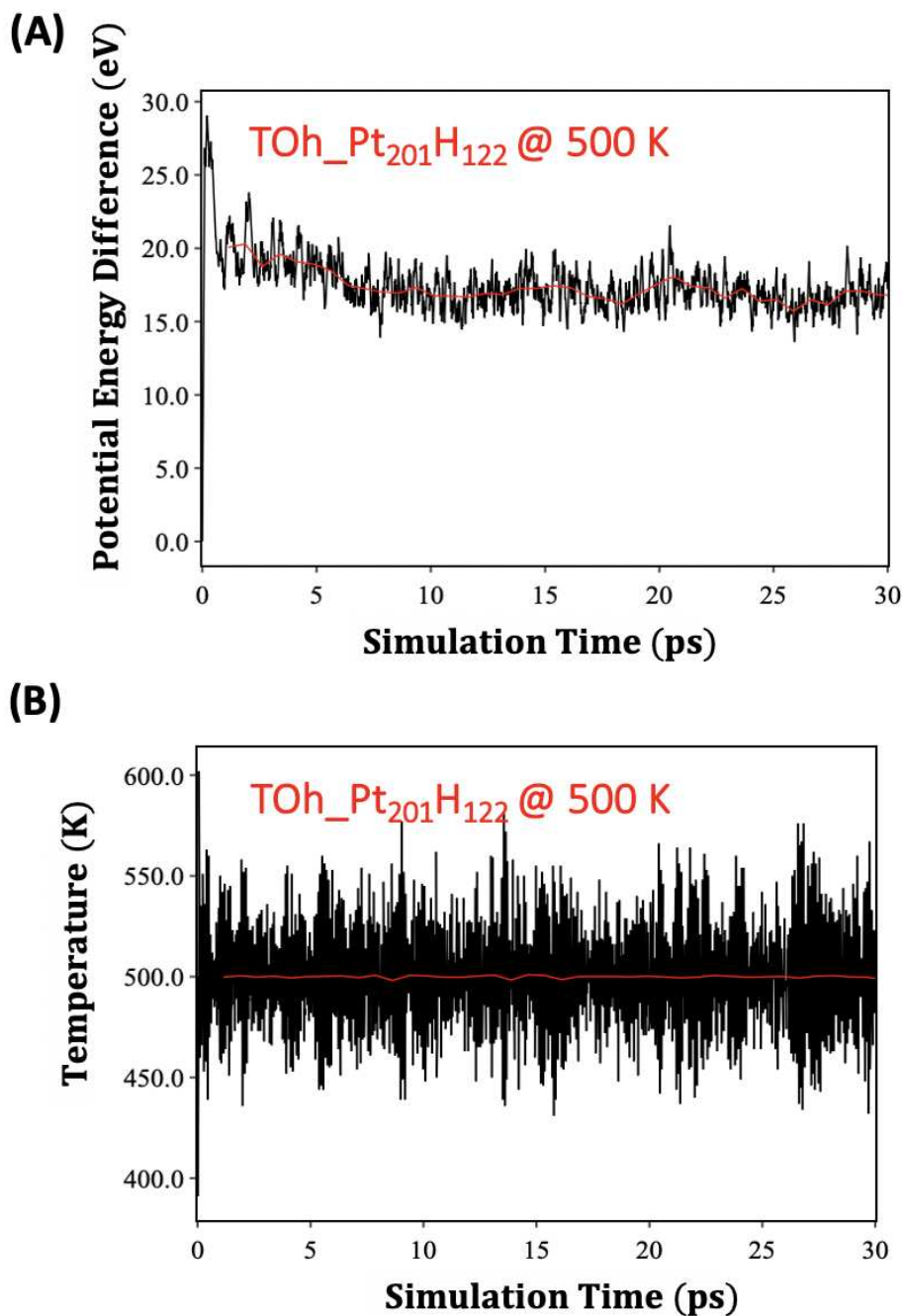


Figure III.9 | *Ab-initio* molecular dynamics (AIMD) simulations of model Pt-NP (TOh_Pt₂₀₁H₁₂₂) in presence of hydrogen at 500 K. (A) Potential energy profiles of TOh_Pt₂₀₁H₁₂₂ relating to the initial state for AIMD simulations at 500 K. (B) Temperature profile of TOh_Pt₂₀₁H₁₂₂ during AIMD simulations at 500 K.

The analysis of the radial distribution functions (**Figure III.10-A**) shows that the peaks relative to the first-neighbor in the TOh_Pt₂₀₁H₁₂₂@500 K are preserved compared to the initial DFT optimized TOh_Pt₂₀₁H₁₂₂@0 K. The “Pt-Pt” first-neighbor peak is located at 2.75 Å in both

structures and also for the bare TOh_Pt_{201} predicted under vacuum. The unique change is observed for the first-neighbor peak of “H-Pt” distance located at 1.75 Å for $\text{TOh_Pt}_{201}\text{H}_{122}@500\text{ K}$ (**Figure III.10-B**). This value is slightly shorter than the initial configuration (the DFT optimized structure) where Pt-H distance is calculated at 1.85 Å. This difference is probably due to the change in the surface hydrogen distribution over the surface where several H atoms initially located on the fcc sites of (1 1 1) facets have moved to the top sites of the (1 1 1) facet and on the edges of Pt-NP.

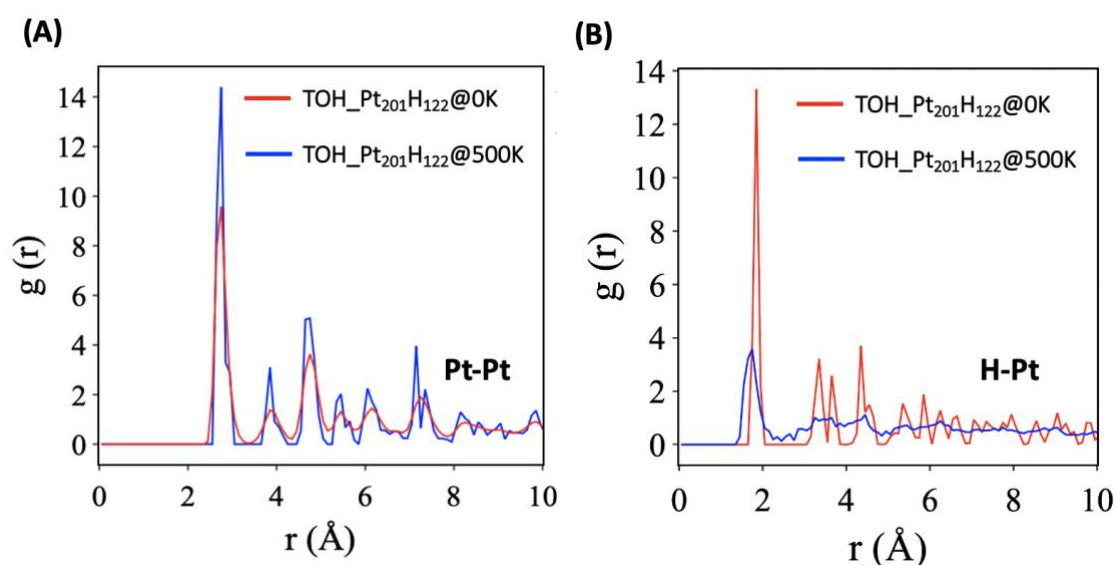


Figure III.10 | Radial distribution functions of initial and final configurations of Pt-NP in presence of hydrogen. (A) between Pt-Pt pairs. (B) between H-Pt pairs.

Finally, the calculation of distance distribution of Pt atoms relative to the mass center of the Pt-NP (**Figure III.11**) shows that the hydrogen adsorption has little effects on the structure of Pt-NP. The hydrogenated final configuration $\text{TOh_Pt}_{201}\text{H}_{122}@500\text{ K}$ is found to maintain its fcc structure as manifested by the three groups of well-defined peaks signature of the fcc symmetry structure.

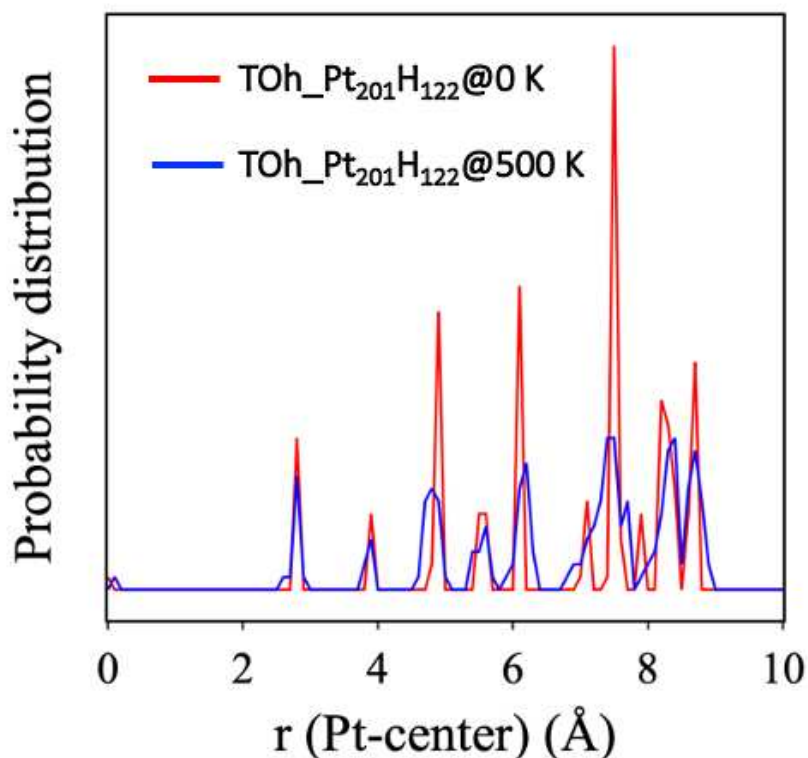


Figure III.11|. The probability distribution functions of the Pt atoms relative to the center of mass between the initial structure (blue line), and the final structure (red line) for Pt-NP in presence of hydrogen at 500 K. The well-defined peaks are signatures of fcc structure of a bare truncated octahedron Pt-NP. After AIMD simulations at 500 K, the Pt-NP shape is slightly disturbed but still maintains its fcc structure.

4. Summary and conclusions

In this chapter, we present our study in the prediction of the equilibrium shapes of Pt-NPs as a function of varied temperature and hydrogen pressure. Two different theoretical approaches depending on the size of the NP are applied:

i) The multi-scale reconstruction approach called MSR model used to predict the shape evolution of the “large-sized Pt-NP” (~5 nm). This method combines the DFT method and the thermodynamics of hydrogen adsorption to calculate the evolution of interface energies as a

function of hydrogen coverage. Then, the Wulff construction theorem is applied to predict the thermodynamic equilibrium shapes of Pt-NPs under hydrogen pressures in the range of $1 \text{ Pa} - 10^5 \text{ Pa}$ and temperature range of $200 \text{ K} - 1200 \text{ K}$;

ii) The AIMD method chosen to study the structure evolution of “small-sized” Pt-NPs. The selected initial model NP is a Truncated Octahedron (TOh) of 201 atoms, ($\sim 1.8 \text{ nm}$). The AIMD method is also based on DFT method and allows exploring the conformational three-dimensional complexity of metal nanoparticles in presence of gas adsorbates, providing structural information with dynamic trajectories that links different possible topological changes. To account for the hydrogen, the Pt-NP is covered by 122 hydrogen atoms, which is equivalent to one monolayer (ML) coverage and pre-optimized by DFT at 0 K . Then AIMD simulations are performed on both bare Pt-NP (TOh_Pt₂₀₁) and hydrogen covered Pt-NP (TOh_Pt₂₀₁H₁₂₂) at finite temperature of 500 K .

The results of our study in exploring the shape evolution of large sized NP under hydrogen pressure show two main regimes:

(i) For hydrogen pressure above 10^4 Pa and temperature varying from 200 to 1200 K , the Pt-NP shape evolves progressively from near-perfect octahedron to near-perfect cube shape. Thus, with increasing temperature, the strong proportion of $(1\ 1\ 1)$ facets forming the NP surface changes to the benefit of the $(1\ 0\ 0)$ facets. These results are in line with the calculated strong hydrogen adsorption on Pt $(1\ 0\ 0)$ surface;

(ii) For hydrogen pressure lower than 10^4 Pa and with temperature increasing, the Pt-NP is found to undergo reversible shape changes. Firstly, the Pt-NP

changes from near-perfect octahedron to the near-perfect cube shape, then for higher temperature, it returns to its initial truncated octahedral shape.

Concerning the small sized Pt-NP, the AIMD simulations of hydrogen covered TOh-Pt₂₀₁_H₁₂₂ show no changes in the structure during simulation time of 30-ps at 500 K. The TOh structure is found to remain extremely stable and the comparison between the bare Pt-NP and hydrogen covered Pt-NP indicates that the strongly adsorbed hydrogen atoms ($E_{\text{ads}} = \sim 0.5$ eV) have no effect on the structure or the shape of small Pt-NP.

To validate these original results, we tried to confront these predicted shape evolutions of Pt under hydrogen media to the experimentally observed results published in the literature. Unfortunately, this was a challenging task, because, as far as we aware, there exists no study devoted to the investigation of the shape changing of Pt-NPs, specifically under hydrogen pressure. Nevertheless, we found several works reporting the changes in the shape of Pt-NPs under capping agents or during synthesis, generally in dry conditions, and the reported shapes fully concord with our predicted shapes.

Finally, we show here that the MSR approach is practical to screen candidate structures with efficiency, especially for big-sized NPs that are out of reach of quantum calculations. However, such approach is only reliable for large size NPs (at least 5 nm) owing to the fact that the DFT parameters applied in this model are calculated from extended surfaces models. In addition, compared to AIMD simulations, which despite being computationally much more expensive, chemical reaction details such as the bond breaking and forming, as well as the adsorbates diffusion evolutions on the surface cannot be captured. One strategy can be pointed out to balance together the accuracy and computational cost for the description of dynamic metallic NPs properties in reactive gas conditions. It is to firstly start by scanning all possible shapes

that may exist under specific P and T of our working catalytic system by using MSR model. Then select one or several most promising structures to be further studied using AIMD simulations for more accurate and detailed understandings of microscopic mechanisms.

Reference

1. Rolison, D. R., Catalytic Nanoarchitectures--the Importance of Nothing and the Unimportance of Periodicity. *Science* **2003**, *299*, 1698-1701.
2. Shao, M.; Peles, A.; Shoemaker, K., Electrocatalysis on Platinum Nanoparticles: Particle Size Effect on Oxygen Reduction Reaction Activity. *Nano Letters* **2011**, *11*, 3714-3719.
3. Li, L.; Hu, L.; Li, J.; Wei, Z., Enhanced Stability of Pt Nanoparticle Electrocatalysts for Fuel Cells. *Nano Research* **2015**, *8*, 418-440.
4. Astruc, D., Introduction: Nanoparticles in Catalysis. *Chemical Reviews* **2020**, *120*, 461-463.
5. Jennings, P. C.; Aleksandrov, H. A.; Neyman, K. M.; Johnston, R. L., A DFT Study of Oxygen Dissociation on Platinum Based Nanoparticles. *Nanoscale* **2014**, *6*, 1153-1165.
6. Li, L.; Plessow, P. N.; Rieger, M.; Sauer, S.; Sánchez-Carrera, R. S.; Schaefer, A.; Abild-Pedersen, F., Modeling the Migration of Platinum Nanoparticles on Surfaces Using a Kinetic Monte Carlo Approach. *The Journal of Physical Chemistry C* **2017**, *121*, 4261-4269.
7. Verga, L. G.; Aarons, J.; Sarwar, M.; Thompsett, D.; Russell, A. E.; Skylaris, C. K., DFT Calculation of Oxygen Adsorption on Platinum Nanoparticles: Coverage and Size Effects. *Faraday Discussions* **2018**, *208*, 497-522.
8. Braunwarth, L.; Jung, C.; Jacob, T., Exploring the Structure–Activity Relationship on Platinum Nanoparticles. *Topics in Catalysis* **2020**, *63*, 1647-1657.
9. An, K.; Somorjai, G. A., Size and Shape Control of Metal Nanoparticles for Reaction Selectivity in Catalysis. *Chemical Catalysis Catalytical Chemistry* **2012**, *4*, 1512-1524.
10. Zhang, H.; Jin, M.; Xia, Y., Noble-Metal Nanocrystals with Concave Surfaces: Synthesis and Applications. *Angewandte Chemie International Edition* **2012**, *51*, 7656-7673.
11. Xie, S.; Choi, S.-I.; Xia, X.; Xia, Y., Catalysis on Faceted Noble-Metal Nanocrystals: Both Shape and Size Matter. *Current Opinion in Chemical Engineering* **2013**, *2*, 142-150.
12. Cao, S.; Tao, F. F.; Tang, Y.; Li, Y.; Yu, J., Size- and Shape-Dependent Catalytic Performances of Oxidation and Reduction Reactions on Nanocatalysts. *Chemical Society Reviews* **2016**, *45*, 4747-4765.
13. Wang, H.; Zhou, S.; Gilroy, K. D.; Cai, Z.; Xia, Y., Icosahedral Nanocrystals of Noble Metals: Synthesis and Applications. *Nano Today* **2017**, *15*, 121-144.
14. Mistry, H.; Behafarid, F.; Zhou, E.; Ono, L. K.; Zhang, L.; Roldan Cuenya, B., Shape-Dependent Catalytic Oxidation of 2-Butanol over Pt Nanoparticles Supported on Γ -Al₂O₃. *ACS Catalysis* **2014**, *4*, 109-115.
15. Fernandez, S., et al., In Situ Structural Evolution of Single Particle Model Catalysts under Ambient Pressure Reaction Conditions. *Nanoscale* **2018**, *11*, 331-338.
16. Liu, L.; Zakharov, D. N.; Arenal, R.; Concepcion, P.; Stach, E. A.; Corma, A., Evolution and Stabilization of Subnanometric Metal Species in Confined Space by in Situ TEM. *Nature Communications* **2018**, *9*, 574.
17. Bergmann, A.; Roldan Cuenya, B., Operando Insights into Nanoparticle Transformations During Catalysis. *ACS Catalysis* **2019**, *9*, 10020-10043.
18. Mavrikakis, M.; Stoltze, P.; Nørskov, J. K., Making Gold Less Noble. *Catalysis Letters* **2000**, *64*, 101-106.
19. Lopez, N.; Janssens, T. V. W.; Clausen, B. S.; Xu, Y.; Mavrikakis, M.; Bligaard, T.; Nørskov, J. K., On the Origin of the Catalytic Activity of Gold Nanoparticles for Low-Temperature CO Oxidation. *Journal of Catalysis* **2004**, *223*, 232-235.

20. Norskov, J. K.; Bligaard, T.; Hvolbaek, B.; Abild-Pedersen, F.; Chorkendorff, I.; Christensen, C. H., The Nature of the Active Site in Heterogeneous Metal Catalysis. *Chemical Society Reviews* **2008**, *37*, 2163-2171.
21. Mostafa, S.; Behafarid, F.; Croy, J. R.; Ono, L. K.; Li, L.; Yang, J. C.; Frenkel, A. I.; Cuenya, B. R., Shape-Dependent Catalytic Properties of Pt Nanoparticles. *Journal of the American Chemical Society* **2010**, *132*, 15714-15719.
22. Blochl, P. E.; Jepsen, O.; Andersen, O. K., Improved Tetrahedron Method for Brillouin-Zone Integrations. *Physical Review B* **1994**, *49*, 16223-16233.
23. Xia, Y.; Xiong, Y.; Lim, B.; Skrabalak, S. E., Shape-Controlled Synthesis of Metal Nanocrystals: Simple Chemistry Meets Complex Physics? *Angewandte Chemie International Edition* **2009**, *48*, 60-103.
24. Sun, Y.; Xia, Y., Shape-Controlled Synthesis of Gold and Silver Nanoparticles. *Science* **2002**, *298*, 2176-2179.
25. Wang, C.; Yin, L.; Zhang, L.; Xiang, D.; Gao, R., Metal Oxide Gas Sensors: Sensitivity and Influencing Factors. *Sensors (Basel)* **2010**, *10*, 2088-2106.
26. Wei, G. F.; Liu, Z. P., Restructuring and Hydrogen Evolution on Pt Nanoparticle. *Chemical Science* **2015**, *6*, 1485-1490.
27. Yu, M.; Liu, L.; Jia, L.; Li, D.; Wang, Q.; Hou, B., Equilibrium Morphology Evolution of FCC Cobalt Nanoparticle under CO and Hydrogen Environments. *Applied Surface Science* **2020**, *504*.
28. Vitos, L.; Ruban, A. V.; Skriver, H. L.; Kollar, J., The Surface Energy of Metals. *Surface Science* **1998**, *411*, 186-202.
29. Tran, R.; Xu, Z.; Radhakrishnan, B.; Winston, D.; Sun, W.; Persson, K. A.; Ong, S. P., Surface Energies of Elemental Crystals. *Scientific Data* **2016**, *3*, 160080.
30. Yu, Y.; Yang, J.; Hao, C.; Zhao, X.; Wang, Z., The Adsorption, Vibration and Diffusion of Hydrogen Atoms on Platinum Low-Index Surfaces. *Journal of Computational and Theoretical Nanoscience* **2009**, *6*, 439-448.
31. Shi, Q.; Sun, R., Adsorption Manners of Hydrogen on Pt(1 0 0), (1 1 0) and (1 1 1) Surfaces at High Coverage. *Computational and Theoretical Chemistry* **2017**, *1106*, 43-49.
32. Bernard Rodriguez, C. R.; Santana, J. A., Adsorption and Diffusion of Sulfur on the (111), (100), (110), and (211) Surfaces of FCC Metals: Density Functional Theory Calculations. *The Journal of Chemical Physics* **2018**, *149*, 204701.
33. Garcia-Araez, N., Enthalpic and Entropic Effects on Hydrogen and Oh Adsorption on Pt(111), Pt(100), and Pt(110) Electrodes as Evaluated by Gibbs Thermodynamics. *The Journal of Physical Chemistry C* **2010**, *115*, 501-510.
34. Ahmadi, T. S.; Wang, Z. L.; Green, T. C.; Henglein, A.; El-Sayed, M. A., Shape-Controlled Synthesis of Colloidal Platinum Nanoparticles. *Science* **1996**, *272*, 1924-1926.
35. Ahmadi, T. S.; Wang, Z. L.; Henglein, A.; El-Sayed, M. A., "Cubic" Colloidal Platinum Nanoparticles. *Chemistry of Materials* **1996**, *8*, 1161-1163.
36. Song, H.; Kim, F.; Connor, S.; Somorjai, G. A.; Yang, P., Pt Nanocrystals: Shape Control and Langmuir-Blodgett Monolayer Formation. *Journal of Physical Chemistry B* **2005**, *109*, 188-193.
37. Bratlie, K. M.; Lee, H.; Komvopoulos, K.; Yang, P.; Somorjai, G. A., Platinum Nanoparticle Shape Effects on Benzene Hydrogenation Selectivity. *Nano Letters* **2007**, *7*, 3097-3101.
38. Duan, M.; Yu, J.; Meng, J.; Zhu, B.; Wang, Y.; Gao, Y., Reconstruction of Supported Metal Nanoparticles in Reaction Conditions. *Angewandte Chemie, International Edition in English* **2018**, *57*, 6464-6469.

39. Shi, Y.; Lyu, Z.; Zhao, M.; Chen, R.; Nguyen, Q. N.; Xia, Y., Noble-Metal Nanocrystals with Controlled Shapes for Catalytic and Electrocatalytic Applications. *Chemical Reviews* **2021**, *121*, 649-735.
40. Watson, G. W.; Wells, R. P. K.; Willock, D. J.; Hutchings, G. J., A Comparison of the Adsorption and Diffusion of Hydrogen on the {111} Surfaces of Ni, Pd, and Pt from Density Functional Theory Calculations. *The Journal of Physical Chemistry B* **2001**, *105*, 4889-4894.

Chapter IV

Modeling small Au nanoparticles under hydrogen media

1. Introduction

Bulk gold is chemically inert and has been generally considered catalytically inactive, until the breakthrough discovery of Haruta [1] in 1987 showing that Au became active for the oxidation of monoxide carbon under temperature even lower than 0 °C when its size is smaller than 5 nm. This precedent finding has led a wave of research towards the catalytic activity of Au nanoparticles (Au-NPs), and applications were discovered in many oxidation and hydrogenation reactions [2-5].

One of the main characteristics of the gold nanocatalysts is that their activity is improved when their size decreases. Over the years, many concepts have been proposed to explain the origin of this higher activity of small Au-NPs. One of them is related to the geometrical effects [6-8]. More precisely, it is widely agreed in the literature, that the low-coordination sites such as the edges and corners are the catalytically active sites of Au-NPs. These sites providing additional surface configurations for adsorbates [9-12], exist in a high proportion in small sized NPs. Indeed, the smaller the nanoparticles, the higher is the fraction of low-coordinated surface atoms. So, as illustrated in **Figure IV.1**, a remarkable increase of the fraction of the step-edge and corner sites on the surface is recorded for Au-NPs size decreasing from 4 to 1 nm.

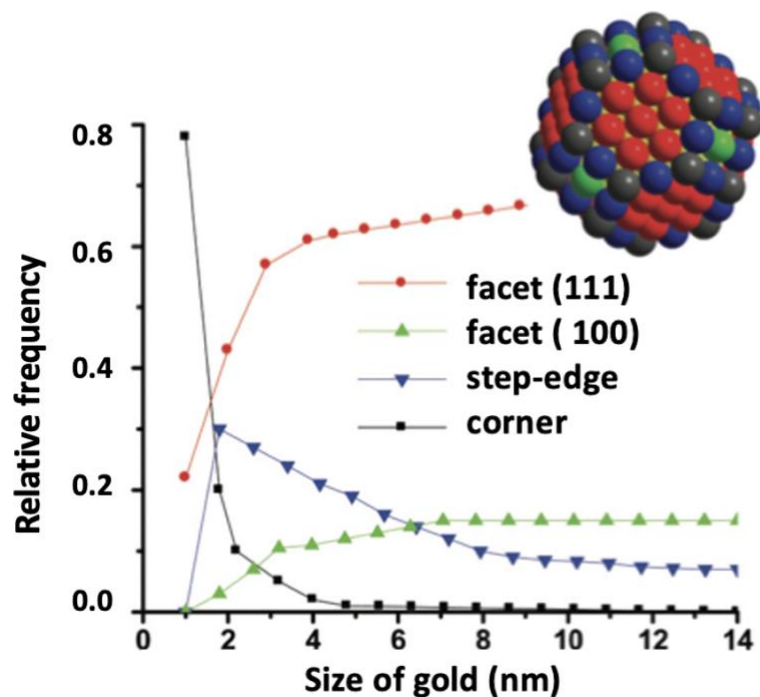


Figure IV.1 | Dependence of relative numbers of surface sites over size of Au nanoparticle, based on cuboctahedron model Au-NP. Figure adapted with permission from [3], Copyright 2001 SAGE Publications.

This concept of increasing fraction of low-coordination sites with decreasing NP size, has been largely adopted for studying the reactivity of Au-NPs, especially in theoretical modeling and in the field of surface science [13]. The common practice is to consider Au nanoparticles as perfect model crystals with well-defined symmetry and “rigid” atomic structure, then to study the interaction of isolated gas molecules on the surface [14-16]. However, as it is addressed all along this manuscript, such model shows serious drawback since it ignores that adsorbates may induce surface changes in response to the reactive environment which eventually may affect their catalytic properties.

Aside from structural effects, quantum-size effects [17-18] are also frequently invoked to explain the exceptional activity of Au-NPs. It has been reported, that reducing the nanoparticle size leads to a discrete electronic band structure that results in a transition from metal to non-metal character. For instance, Valden *et al.* [19] reported that for Au clusters ranging in size

from 1 to 6 nm supported on single crystalline surfaces of titania, the scanning tunneling microscopy measurements showed that the catalytic activity coincides with the onset of a band gap uncharacteristic (appearance of the non-metallic properties) of Au bulk metals. Moreover, several other works strongly suggest that Au particles below ~ 2.5 nm in size exhibit non-metallic character, which makes them especially active in H_2 chemisorption and dissociation [20] favoring H-rich environment promoting hydrogenation reactions.

Despite the diversity of proposed concepts and assumptions, no agreement on the origin of the improved reactivity of small-sized Au-NPs was found. This is because of the lack of a tangible scenario that takes into account the surface atomic evolution under *realistic* temperature and pressure conditions.

The powerful development of *in situ* experimental techniques has extended the characterization of catalysts from the ultra-high vacuum into more realistic working (T, P)-conditions. Recently, the *in situ* aberration-corrected environmental transmission electron microscopy (ETEM) observations of gold catalysts under hydrogen were performed by our collaborators (Dr. Jaysen Nelayah's group) from the Laboratoire Matériaux et Phénomènes Quantiques, Université de Paris. These colleagues investigated structural evolutions of supported Au-NPs on titanium oxide surface with different sizes under different temperatures and hydrogen gas pressures. Their *in situ* atomic-scale observations of individual Au-NPs complemented with *ex situ* TEM observations show that the fcc Au-NPs initially (under inert gas) shaped as truncated octahedron (TOh) undergo dramatic structural changes in H_2 when the size is smaller than ~ 4 nm. In contrast, the TOh shape is roughly maintained for the Au-NPs with bigger size. In order to address the above experimentally observed size-dependent shape transition, and to understand the factors ascribable to the shape changes in small gold NPs, we performed AIMD simulations. This method is capable of capturing the complex dynamic changes of materials in reactive gas

condition (see discussion in **Chapter 1**), and thus expected to be able to reveal the origin of those experimental observed structural transformations of the small-sized Au-NPs under hydrogen condition. In this chapter, we start by presenting a summary of the experimental observations (section 2) and then we introduce the theoretical methodology details in section 3. In section 4, the AIMD simulation results are detailed where geometric and electronic structure analyses are presented and thoroughly analyzed and discussed. This work was submitted for publication in the journal “Small”.

2. Experimental Observation

In the following, the experimental details evidencing the size-dependent structural changes of Au-NPs in H₂ are presented. All these experimental manipulations/data are achieved/provided by our collaborators (Dr. Jaysen Nelayah's group, Laboratoire Matériaux et Phénomènes Quantiques, Université de Paris).

Size-dependent structural change

Figure IV.2 shows the selected *in situ* high angle annular dark field scanning ETEM (HAADF STEM) images of Au-NPs of two different sizes: 4.5 nm (**Figure IV.2-A**) and 3 nm (**Figure IV.2-B**) under Ar exposure (vacuum) and under 10⁵ Pa H₂. Under vacuum conditions, it can be seen that for both investigated sizes, the Au-NPs are in truncated octahedral shape (TOh) with well-defined (1 1 1) and (1 0 0) facets. In contrast, when exposed to H₂, size-dependent structural changes of Au-NPs are revealed, where the 4.5 nm Au-NP is found to keep its initial TOh shape (fcc structure) from 400 °C to 25 °C, while the 3 nm-sized Au-NP drastically changed and transformed into a rounded shape at 400 °C and at 200 °C.

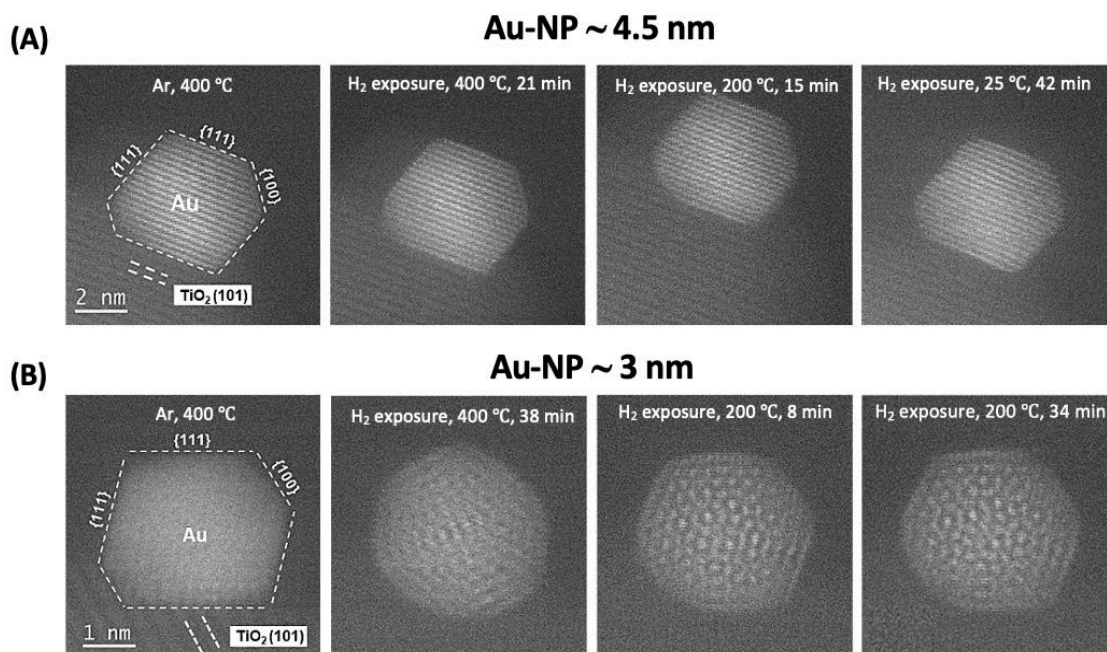


Figure IV.2 | *In situ* HAADF STEM of Au-NPs supported on anatase titania in Ar and under H₂. (A) 4.5 nm Au-NP sequentially acquired in 40 Pa Ar at 400 °C and 10⁵ Pa H₂ at 400, 200 and 25 °C. (B) 3 nm Au-NP in 40 Pa Ar at 400 °C and 10⁵ Pa H₂ at 400 and 200 °C. The broken white lines highlight the projected truncated octahedral equilibrium shapes of both NPs in Ar at 400 °C.

Moreover, the rounded shape observed for 3 nm-sized Au-NPs was further proofed as an icosahedral-shape by comparing with the kinematic STEM simulations of Au₉₃₁ icosahedron in vacuum (see **Figure IV.3**).

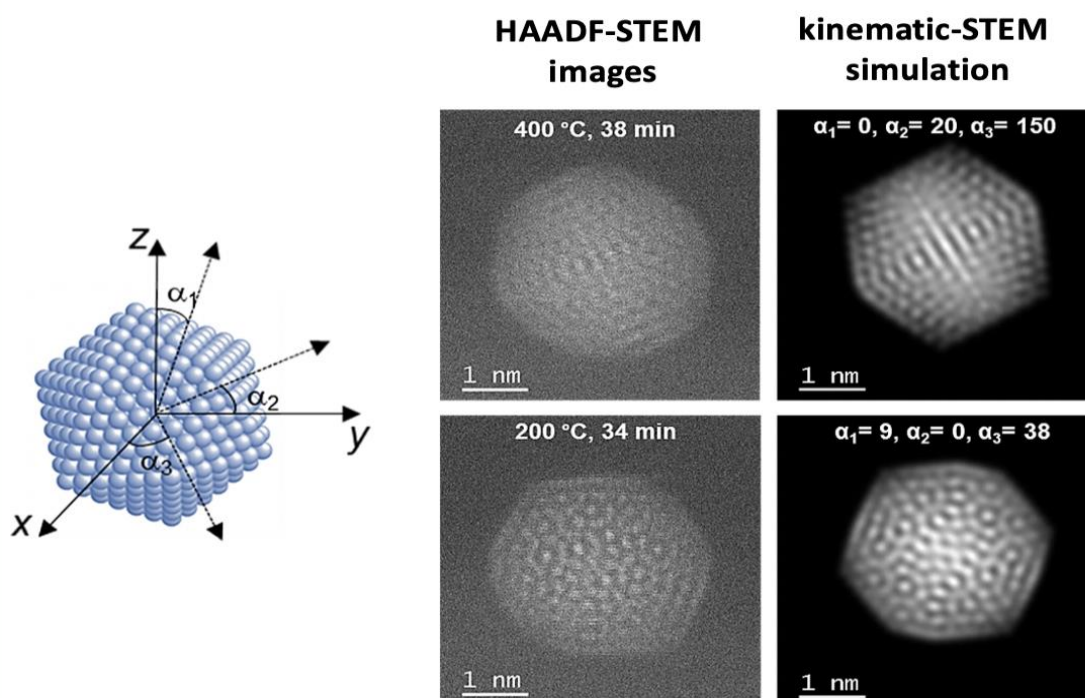


Figure IV.3]. Comparison of HAADF-STEM images of 3 nm Au-NPs captured from Figure IV-2-b with the Kinematic STEM simulation of an icosahedral Au₉₃₁ NPs under vacuum. Left side of the figure shows the referenced geometry of STEM simulation. The electron beam is incident along the Z direction and the particle can be tilted in any direction with respect to the incoming electrons via angles α_1 , α_2 and α_3 . The kinematic STEM simulations of Au₉₃₁ icosahedron in vacuum is viewed close to its 2-fold (top) and a five-fold (bottom) axes.

Based on the above *in situ* images and the kinematic simulation results, it can be confirmed that the small-sized Au-NPs (< 3 nm) undergo structural changes from TOh shape (fcc structure) to rounded shape (icosahedral-like structure) under H₂ condition. In contrast, H₂ exposure has roughly no effect on the structure of Au-NPs with size above 4 nm. This result presents, the first experimental observation evidencing size-dependent structural transformation of Au-NPs under hydrogen condition. Moreover, no theoretical work has been devoted to the investigation of hydrogen effects on the structural evolution of small gold NPs. In order to fill this gap, the work described in the following sections was performed.

3. Theoretical details

3.1 Cluster model

Same as in the case of our study on Pt small NPs, we considered the truncated octahedron (TOh) shape with the size of 1.8 nm containing 201 atoms to model small gold NP (herein noted as TOh_Au₂₀₁). To simulate the hydrogen-exposure environment, the Au-NP is covered by 122 H atoms (denoted as TOh_Au₂₀₁H₁₂₂), which corresponds to a gas coverage of one monolayer (1 ML). The Au-NP model structures were modelled using an orthorhombic periodic cell of dimensions $(30 \times 30 \times 30)\text{\AA}$. Note that the NP models for MD simulations (TOh_Au₂₀₁ and TOh_Au₂₀₁H₁₂₂) were initially pre-optimized by DFT calculations, leading to fcc local minimum energy structures with slightly distorted surface facets, for the case of hydrogen adsorption with H atoms mainly occupying bridge and hollow sites on the Au-NP surface.

3.2 AIMD simulations and DFT calculations

Ab initio molecular dynamics simulation invoking Born-Oppenheimer approximation were carried out in the canonical (NVT) ensemble employing Nosé-Hoover thermostats [21-22] with a time step of 1.5-fs at 300 and 500 K for at least 60-ps time span. All *ab initio* MD simulations and DFT calculations were conducted using Vienna *Ab-initio* Simulation Package (VASP) [23]. All local minima associated with specific atomic arrangements selected from MD simulations have been isolated and their geometrical and electronic properties have been calculated and analyzed by DFT method. The generalized gradient approximation functional of the exchange–correlation energy was calculated within the Perdew, Burke, and Ernzerhof formulation [24] of the generalized-gradient approximation (GGA-PBE). The van der Waals interactions were included using Grimme’s dispersion correction terms [25]. The cut-off energy was fixed to 400 eV. The convergence criterion for the electronic self-consistent cycle was fixed to 10^{-6} eV.

Geometry optimizations were performed within a conjugate-gradient algorithm until the convergence criterion on forces ($10^{-2} \text{ eV} \cdot \text{\AA}^{-1}$) was reached.

Velocity rescaling

In this chapter, the direct Canonical (NVT) ensembles are employed for the simulations of TOh_Au₂₀₁ under vacuum. For the hydrogenated-gold NP and considering the possible hydrogen adsorption inducing strong energy fluctuations, velocities of the initial structure (TOh_Au₂₀₁H₁₂₂) were primally scaled at each ionic step to allow a continuous increase of the kinetic energy. This leads to a gradually heated up temperature from 0 to 500 K within 1.5-ps simulation time. Then the temperature was maintained at 500 K under NVT ensemble until the end of simulation (60-ps).

4. Results and discussion

4.1 AIMD simulation of Au NP under vacuum

The AIMD simulation of the TOh_Au₂₀₁ structure under vacuum was performed at 300 and 500 K for over 60-ps simulation time. As illustrated by the **Figure IV.4**, the Au-NP reaches its dynamic equilibrium state around ~3-ps, after which a fluctuation of relative potential energy difference remains less than ~1 eV until 60-ps of simulation time. The temperature also remains well stabilized close to 300 K (**Figure IV.4-B**) where the averaged temperature curve (red curve) tightly sticks around 300 K. The similar energy and temperature stabilization processes of TOh_Au₂₀₁ is also observed for simulations under vacuum at 500 K (see **Figure-IV.5**).

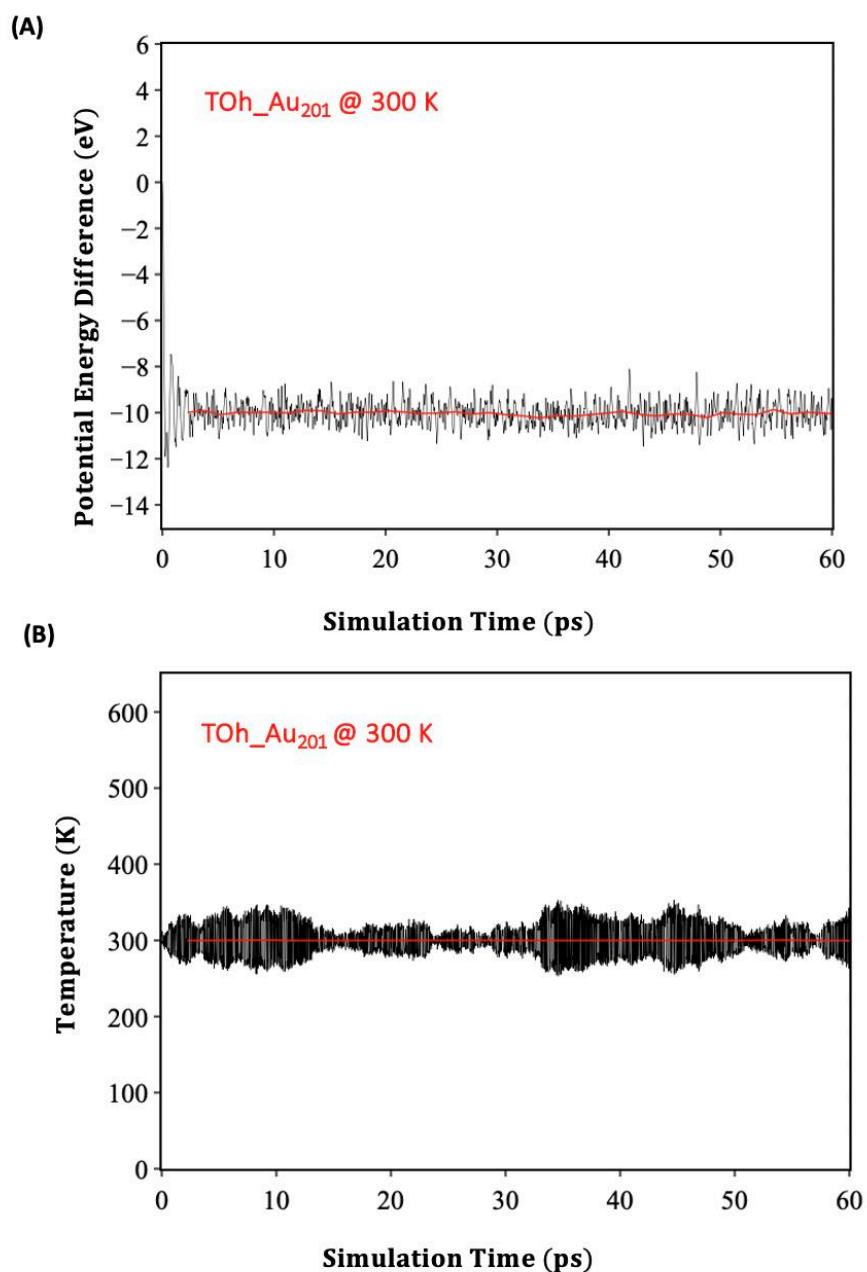


Figure V.4 | *Ab-initio* molecular dynamics (AIMD) simulations of TOh_Au₂₀₁ (under vacuum) at 300 K. (A) Potential energy profiles of TOh_Au₂₀₁ relating to the initial state for AIMD simulations. (B) Temperature profile of TOh_Au₂₀₁ during AIMD simulations. The red curves are the fitted average values taken at each 1-ps of simulation time.

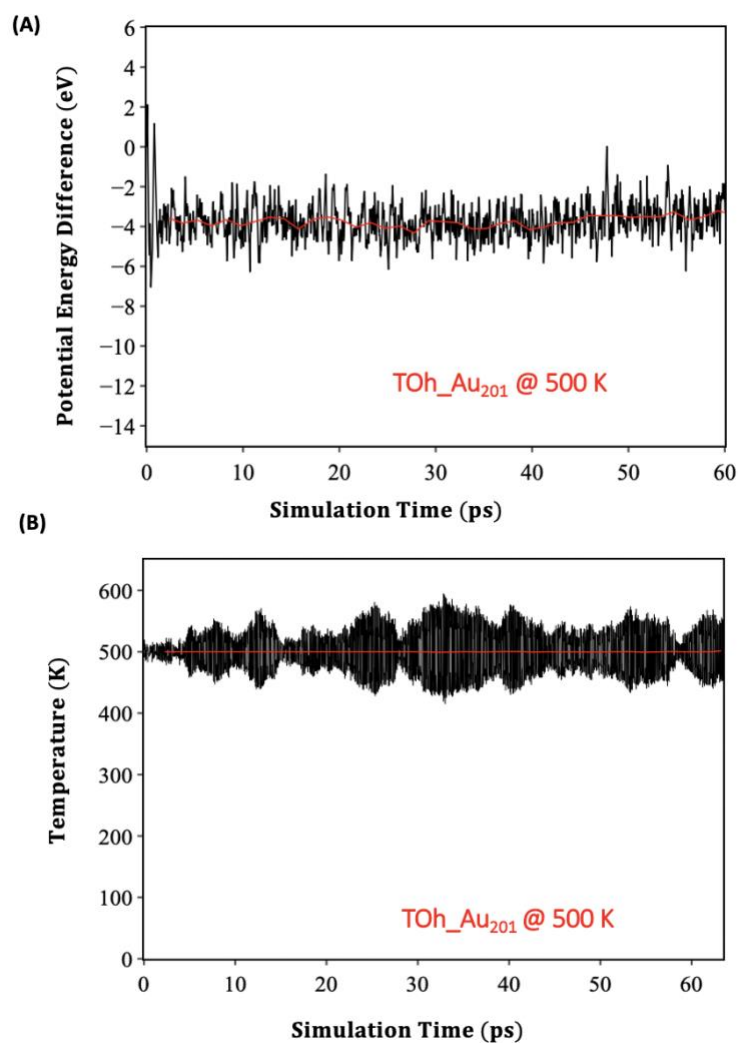


Figure IV.5|. *Ab-initio* molecular dynamics (AIMD) simulations of TOh_Au₂₀₁ (under vacuum) at 500 K. (A) Potential energy profiles of TOh_Au₂₀₁ relating to the initial state for AIMD simulations. (B) Temperature profile of TOh_Au₂₀₁ during AIMD simulations. The red curves are the fitted average values taken at each 1-ps of simulation time.

The DFT pre-optimized initial structure (denoted as TOh_Au₂₀₁@0 K) before conducting AIMD simulations and the final structure under 300 K (TOh_Au₂₀₁@300 K) and under 500 K (TOh_Au₂₀₁@500 K) extracted from the last trajectory of simulations are compared by the radial distribution function of “Au-Au” distance and the probability distribution functions of the Au atoms relative to the center of mass of Au-NPs (**Figure IV.6** for 300 K and **Figure IV.7** for 500 K).

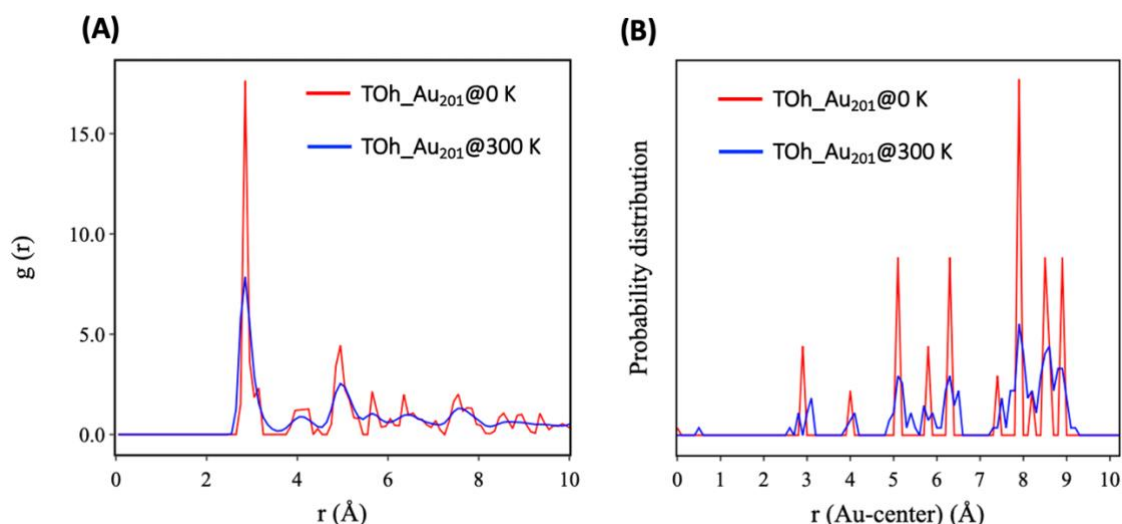


Figure IV.6]. *Ab-initio* molecular dynamics (AIMD) simulations of TOh_Au₂₀₁ (under vacuum) at 300 K. (A) Radial distribution functions of initial TOh_Au₂₀₁ structure (red line) and the final structure (blue line) between Au-Au pairs. (B) The probability distribution functions of the Au atoms relative to the center of mass between the initial structure (red line), and the final structure (blue line).

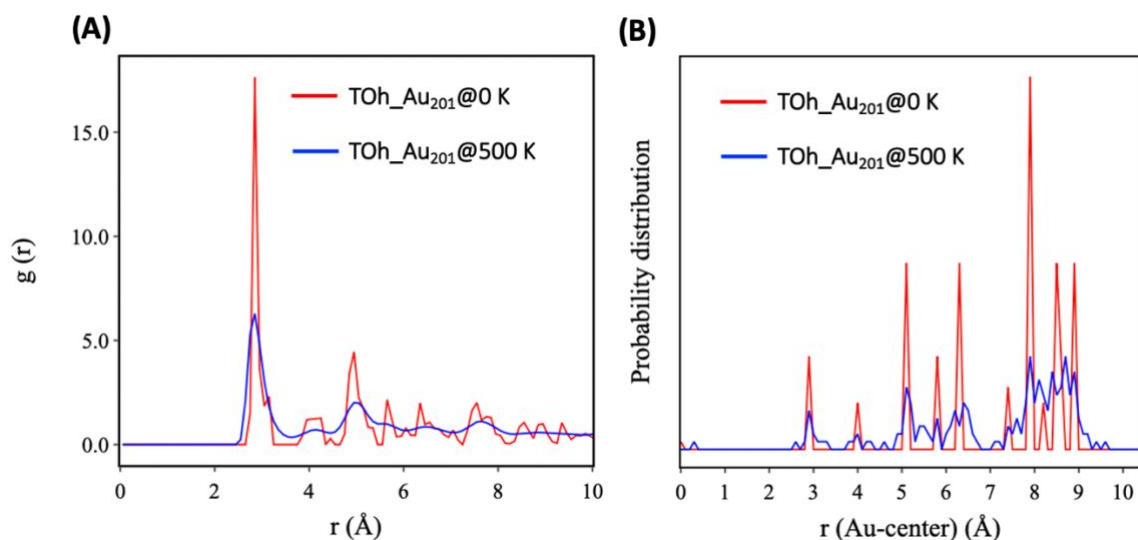


Figure IV.7]. *Ab-initio* molecular dynamics (AIMD) simulations of TOh_Au₂₀₁ (under vacuum) at 500 K. (A) Radial distribution functions of initial TOh_Au₂₀₁ structure (red line) and the final structure (blue line) between Au-Au pairs. (B) The probability distribution functions of the Au atoms relative to the center of mass between the initial structure (red line), and the final structure (blue line).

In accord with the experimental observation (**Figure IV.2-B**) on small-sized Au-NPs under Ar at 400 °C, there is no structural changes found during the AIMD simulations for TOh_Au₂₀₁ at

both investigated temperatures of 300 and 500 K. To confirm this, the radial distributions of the resulted structures are analyzed. As shown in **Figure IV.6-A** and **Figure IV.7-A** the first neighbor peaks of “Au-Au” distance are located at 2.85 Å for the initial and the final structure of TOh_Au₂₀₁. Besides, it can be seen that the distribution function of the final structure TOh_Au₂₀₁@300 K and TOh_Au₂₀₁@500 K both maintain their fcc structure within the simulation time span as manifested by the 3 groups of well-defined fcc-signature peaks (**Figure IV.6-B, Figure IV.7-B**). These peaks correspond to the distances of the atoms in the fcc core (located at 2.9 Å), the inner-shell of NP (located at 3.9 ~ 6.5 Å) and the outer-shell (located at 7.2 ~ 9 Å). Thus, despite a few slightly scattered distributions, the peaks remain restrained to their corresponding centers under 300 and 500 K.

To sum up, according to the analysis of MD simulations on the bare Au-NP (TOh_Au₂₀₁) under different temperatures, it can be confirmed that for a TOh shaped Au-NP under vacuum condition, there is no structural effects on the bare NP and the fcc structure remains well preserved whatever the applied temperature.

4.2 AIMD simulation of Au NP in presence of hydrogen

The initial step before running AIMD simulations on hydrogen covered TOh Au-NP was to optimize the structure with DFT. The results show slight surface disturbance induced by the adsorbed 1 ML H atoms mainly locating on the bridge and top sites of Au-NPs surface. As illustrated in the **Figure IV.8**, the TOh shape and the fcc symmetry remain unchanged after DFT geometry optimization. The adsorption energy is calculated to be of +0.08 eV, which indicates a very weak H-adsorption on the Au-NPs. Taking this optimized structure as initial configuration, AIMD simulation over more than 60-ps of time span under 300 and 500 K were performed.

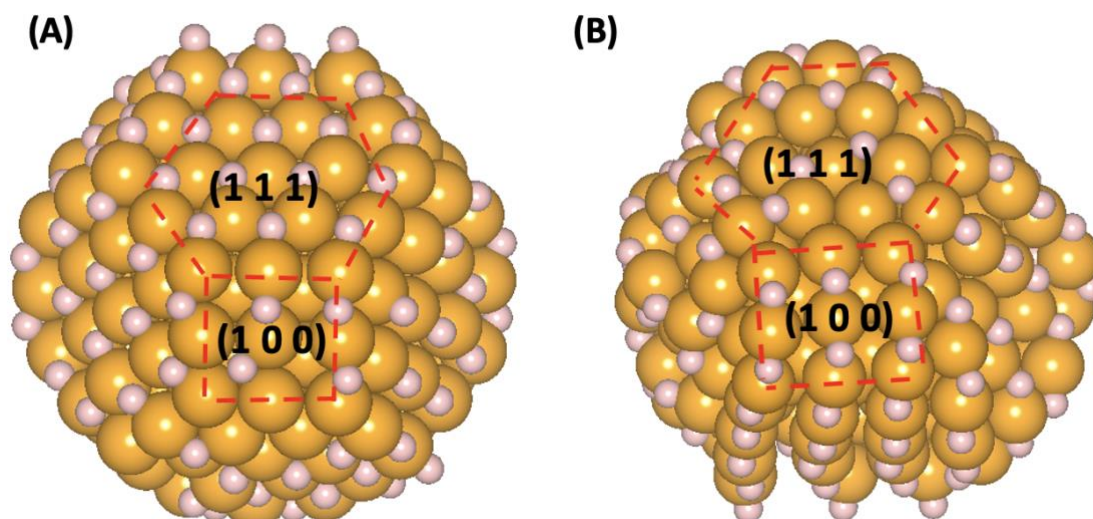


Figure IV.8|. Illustration of the Au-NP with 1 ML of atomic hydrogen coverage (A) before and (B) after the DFT geometry optimization at 0 K.

4.2.1 Hydrogenated Au-cluster simulation under 300 K

Equilibrium process

During the simulation of hydrogenated Au-NP under 300 K, according to the relative potential energy profile (**Figure IV.9-A**), the energy progressively increases of about ~ 13 eV compared to its initial value during the velocity scaling process (0-1.5-ps) with increasing temperature from 0 to 300 K (**Figure IV.9-B**). Then the potential energy rapidly drops during the first 15-ps simulation time, which is the result of the 3 pairs of hydrogen atoms that were desorbed from the Au-NPs surface during that time. After this period, the system starts to stabilize with small energy fluctuations continuing until the end of simulation. Similarly, the temperature stabilizes around 300 K after the 1.5-ps of velocity scaling time.

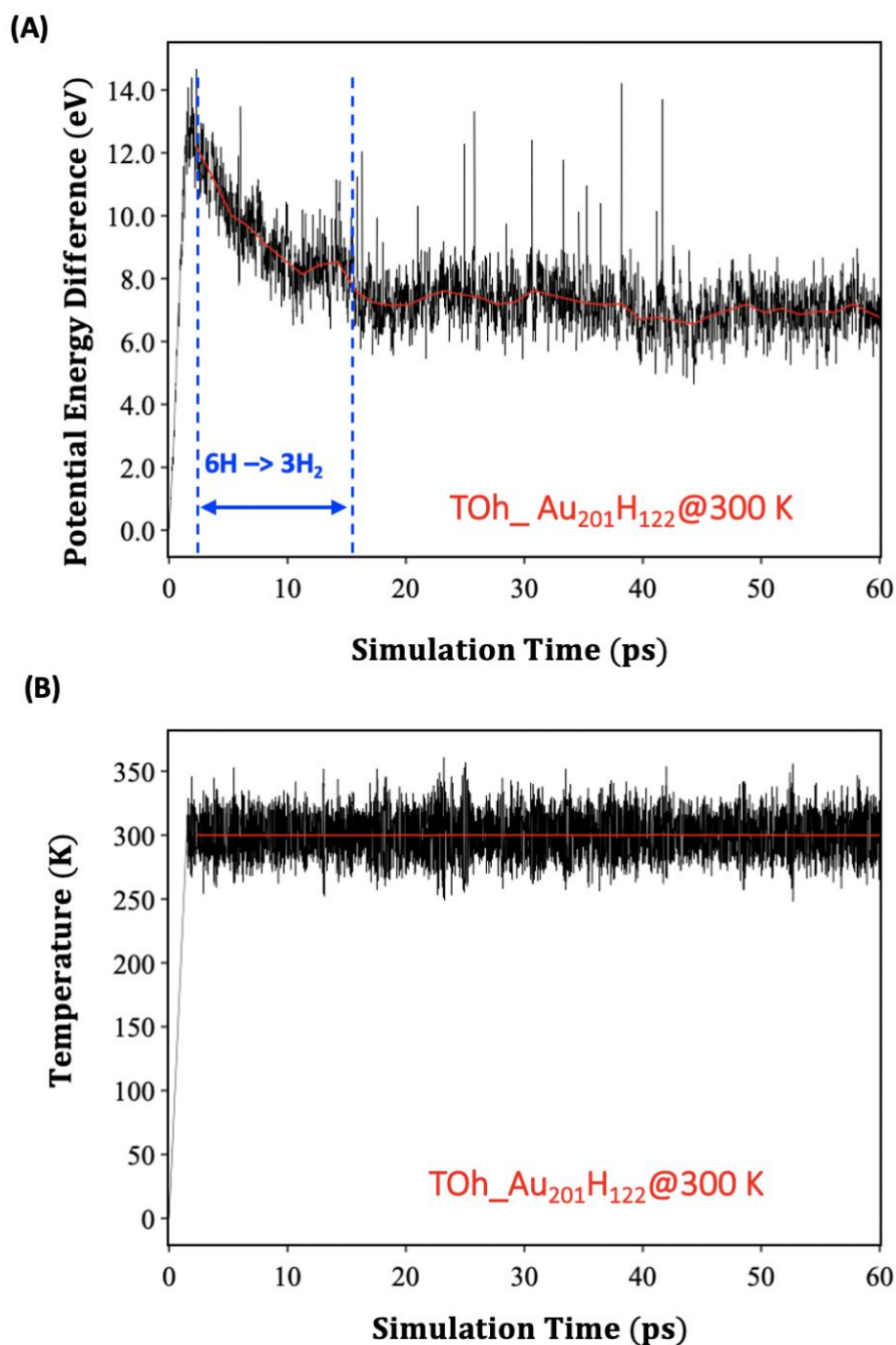


Figure IV.9|. *Ab-initio* molecular dynamics (AIMD) simulations of model Au-NP (TOh_Au₂₀₁H₁₂₂) in presence of hydrogen at 300 K. (A) Potential energy profiles of TOh_Au₂₀₁H₁₂₂ relating to the initial state for AIMD simulations. (B) Temperature profile of TOh_Au₂₀₁H₁₂₂ during AIMD simulations. The red curves are the fitted average values taken at each 1-ps of simulation time.

Configurational evolutions

Figure IV.10 shows four configurations extracted from the AIMD simulation of the hydrogenated Au-NP evolving as a function of time under 300 K:

i) the Configuration-0 corresponding to the DFT pre-optimized initial structure, ii) the Configuration-1 selected after 1.5-ps time simulation span, which corresponds to the end of velocity scaling process where the temperature reached 300 K, iii) the Configuration-2 extracted at 40-ps, and iv) the Configuration-3 which is the final structure after 60-ps simulation time.

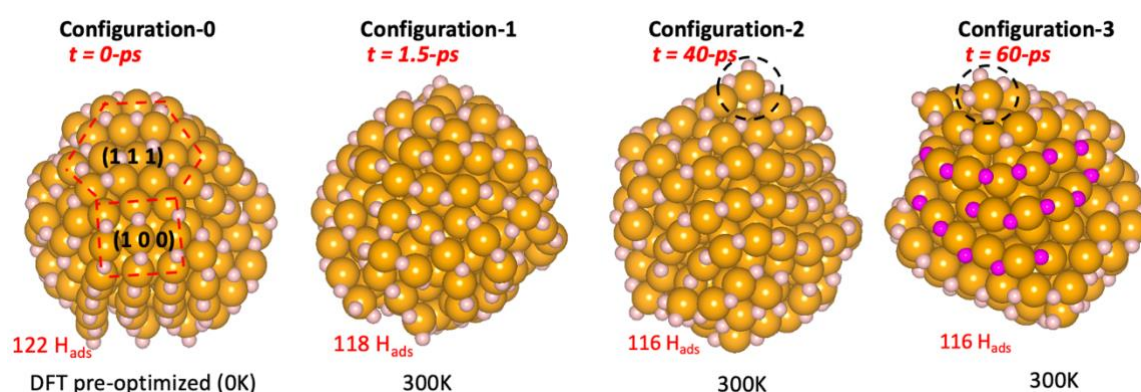


Figure IV.10]. Illustration of hydrogenated Au-NPs configurations extracted from AIMD simulation at 300 K. Structure of hydrogenated Au-NPs extracted at simulation time: 0-ps (initial structure, pre-optimized by DFT), 1.5-ps, 40-ps and 60-ps. Some formed crown like “H-Au-H” chains are highlighted with H atoms colored in magenta to facilitate the view.

During the simulation process, hydrogen desorptions are found to occur and the number of adsorbed hydrogens decrease progressively. As it can be seen from **Figure IV.10**, at 1.5-ps (Configuration-1), the structure of Au-NP readily undergoes an evident structural change with hydrogens arranged themselves preferentially on the bridge sites of surface Au atoms, and the initially well-defined (1 1 1) and (1 0 0) facets have been lost. Then the structure continues to evolve with hydrogen atoms constantly moving on the surface of Au-NP forming well-ordered

“H-Au-H” chains with one hydrogen bridging two Au atoms, like “crowns” (see the chains with H atoms marked in magenta on Configuration-3). The overall shape of the simulated NP is transformed from TOh to distorted sphere. This predicted transformation confirms the experimentally observed drastic structural changes of small-sized Au-NPs from the TOh to rounded-shape nanoparticles under hydrogen atmosphere.

To identify the structure of the formed rounded-shape, the final structure, Configuration-3, was extracted and re-optimized using DFT at 0 K (denoted as Configuration-3'), then compared with the “perfect” fcc structure TOh_Au₂₀₁ in **Figure IV.11**.

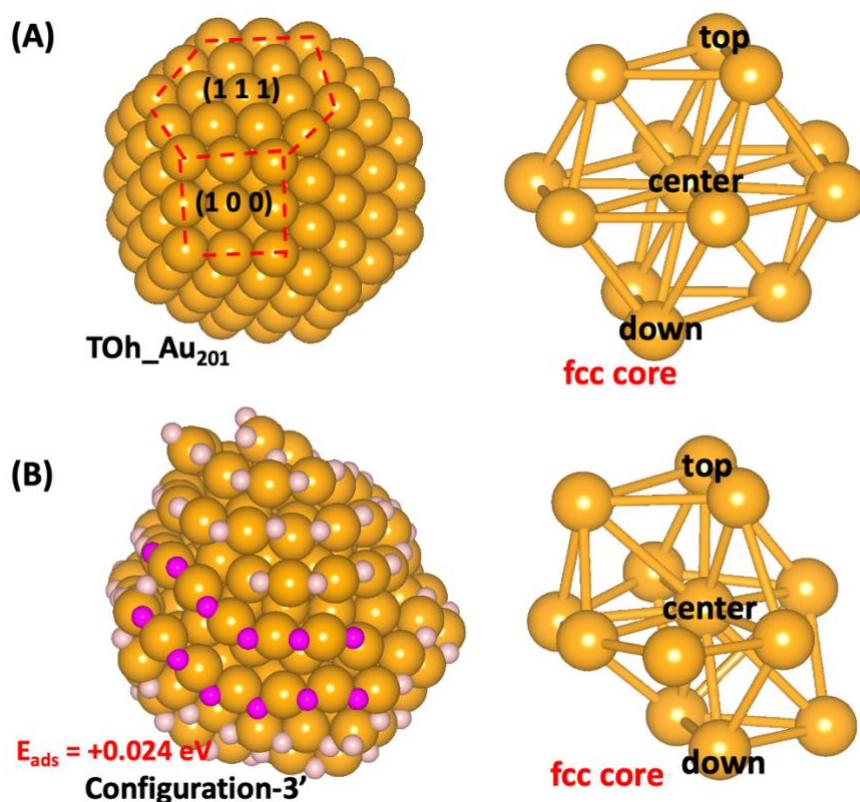


Figure IV.11]. Structural comparison between Configuration-3' and TOH_Au₂₀₁. (A) The configuration of the DFT optimized TOH_Au₂₀₁ (left) and its core structure showing a typical fcc basic crystal arrangement (right). (B) DFT optimized structure extracted from the last trajectory of AIMD simulation of hydrogenated Au-NP under 300 K (left, denoted as Configuration-3') and its core structure showing a slightly disturbed fcc basic crystal arrangement (right).

As depicted in **Figure IV.11**, the Configuration-3' is indeed a rounded shape NP with well ordered “crown-like” structure of the hydrogenated gold at the surface. For this structure, the hydrogen adsorption energy is found to be slightly improved after to the desorption of 3 pairs of H₂ ($E_{\text{ads}} = +0.024$ eV instead of +0.08 eV on the initial configuration). The core-structure of Configuration-3' presented in **Figure IV.11-B** (right-side picture) is compared with the referenced core-structure of the fcc TOh_Au₂₀₁ NP (**Figure IV.11-A**). As one can see for a typical fcc crystal arrangement, the atoms are organized as follows: 1 atom in the body-center, 6 atoms in its horizontal plane and 3 atoms on the top, 3 atoms on the bottom, which counts 13 atoms in total. The core-structure of Configuration-3' is found to keep this fcc arrangement although undergoes slight deformation. To summarize, the AIMD simulation of hydrogenated Au-NP under 300 K indicates drastic morphological changes which confirms the *in situ* experimental observations. However, under this temperature, the theoretical results show no symmetry transformation as the fcc remains stable for simulation time span as longer as 60-ps. At 300 K, the “icosahedral-like” structure is not captured by the AIMD simulation, which is probably due to the low temperature that cannot provide sufficient kinetic energy to the system to overcome the activation energy barrier necessary to reach the symmetry transition. For this reason, AIMD simulations of hydrogenated Au-NPs were further performed at 500 K.

4.2.2 Hydrogenated Au-cluster simulation under 500 K

Equilibrium process

As shown in **Figure IV.12-A**, during AIMD simulation of the hydrogenated Au-NPs under 500 K, the potential energy of the system abruptly increases to ~ 24 eV in the first 1.5-ps of velocity scaling process, then the energy drops rapidly during ~ 20-ps of time. In this period, 10 pairs of H₂-desorb from the surface. Then, the energy fluctuation starts to reduce and become quite stable after 40-ps of simulation time (less than ~1.5 eV of fluctuation) until the end of

simulation. Concerning the temperature, the **Figure IV.12-B** shows stable fluctuation around 500 K after the first 1.5-ps velocity scaling process.

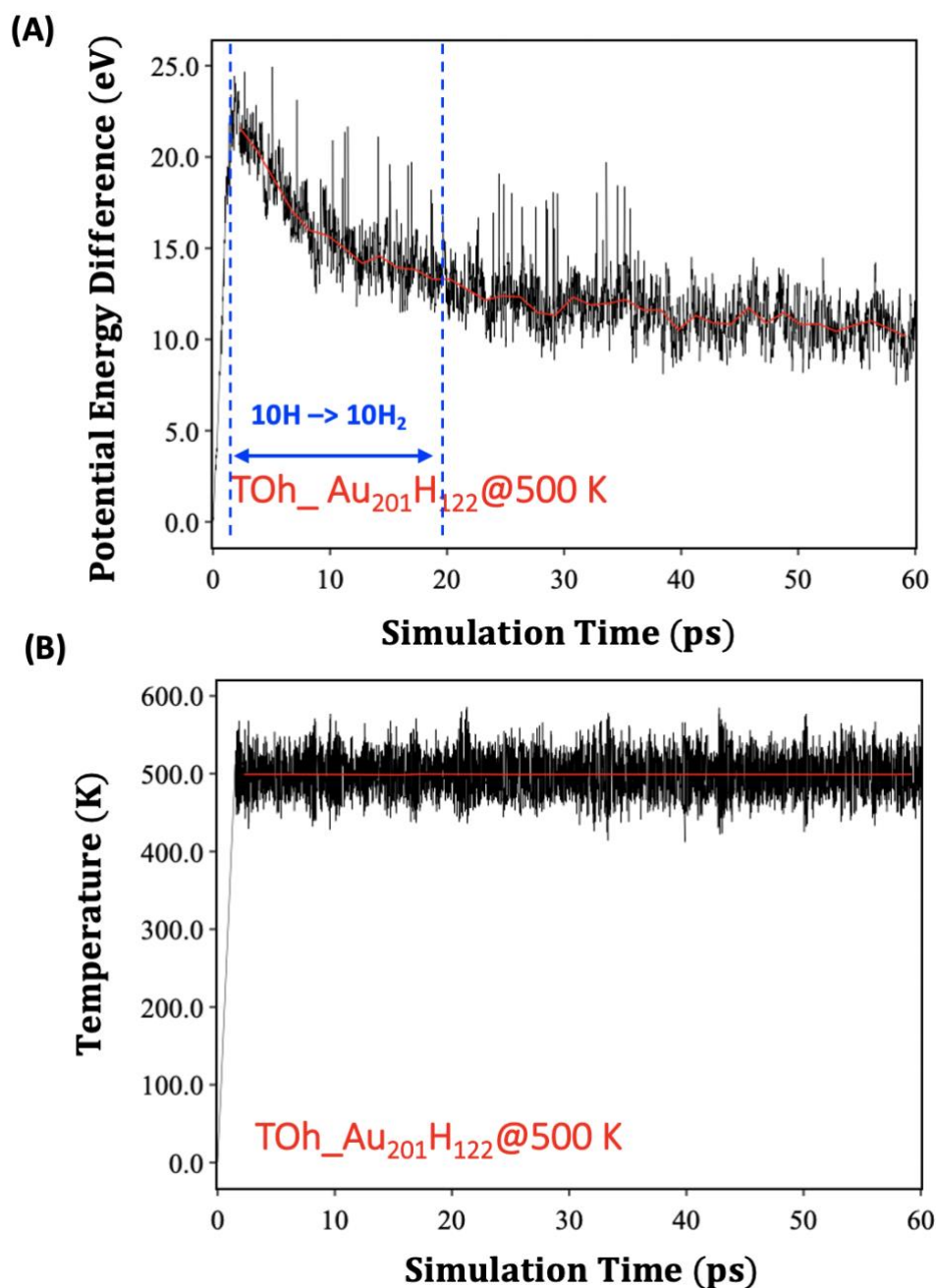


Figure IV.12 | . *Ab-initio* molecular dynamics (AIMD) simulations of model Au-NP (TOh_Au₂₀₁H₁₂₂) in presence of hydrogen at 500 K. (A) Potential energy profiles of TOh_Au₂₀₁H₁₂₂ relating to the initial state for AIMD simulations. (B) Temperature profile of TOh_Au₂₀₁H₁₂₂ during AIMD simulations. The red curves are the fitted average values taken at each 1-ps of simulation time.

Configurational evolutions

Similar to the case of 300 K, three configurations are extracted from trajectory time during the AIMD simulation. The **Figure IV.13** shows the initial configuration (Configuration-0) at 0-ps, which is the DFT pre-optimized structure, the Configuration-b taken at 1.5-ps, the Configuration-c, extracted at 40-ps and the final structure, Configuration-d, at 60-ps.

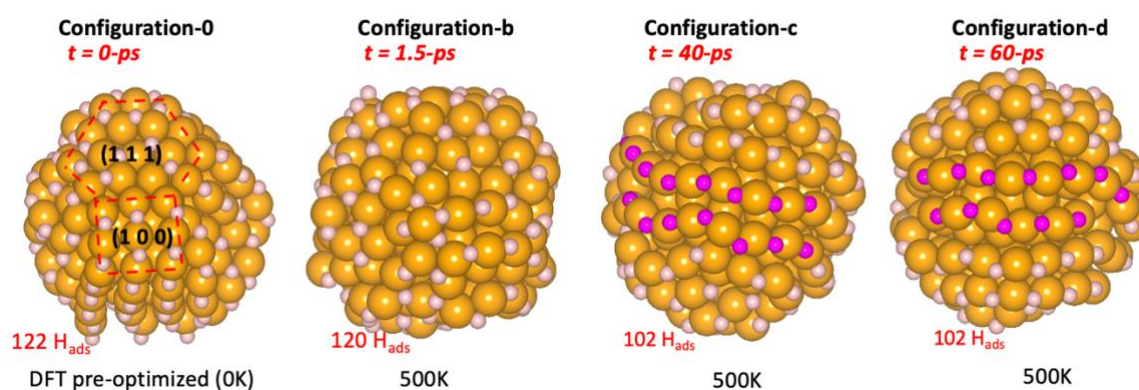


Figure IV.13]. Illustration of hydrogenated Au-NPs configurations extracted from AIMD simulation at 500 K. (Structure of Au-NPs extracted at simulation time: 0-ps (initial structure, optimized by DFT), 1.5-ps, 40-ps and 60-ps. Some formed crown-like “H-Au-H” chains are highlighted with H atoms colored in magenta to facilitate the view.

From **Figure IV.13**, it can be seen that similar to the simulation under 300 K, the hydrogenated Au-NP readily loses its TOh equilibrium shape during the first rescaling period (Configuration-b at 1.5-ps) in which 1 pair of H_2 desorbs from the surface. Then 9 more pairs of atomic hydrogen desorbed progressively into H_2 gas molecules while others highly diffuse on the surface. From 40-ps to the end of the simulation (Configuration-c and -d, the H atoms on two of the crown-like chains are marked with magenta color), the mobile hydrogen stabilizes on bridge sites leading to an arrangement in the form of “crown-like” “H-Au-H” chains. The resulted shape of the NP is rounded with well ordered “H-Au-H” chains sliding over a highly distorted core. The hydrogen coverage in the end of the simulation is found to reach 0.8 ML with 102 H adsorbed H on the surface. This final structure resulting from the AIMD simulation

at 500 K (Configuration-d) is then extracted and re-optimized by DFT at 0 K (denoted as (Configuration-d')). As shown in **Figure IV.14-A**, the ordered “H-Au-H” chains are well defined with almost constant “H-Au” and “H-H” distances (as an illustrative example, one of the surface chains with “H-Au” and “H-H” bond distances is presented in **Figure IV.14-B**). Moreover, the calculated hydrogen adsorption energy under this structure is calculated to be of -0.025 eV, which indicates a favorable hydrogen bonding on Au-surface in contrast with the initial configuration ($+0.08$ eV), as well as the final structure obtained from AIMD simulation under 300 K ($+0.024$ eV) both showing unfavorable H-Au bonding. The structure of Configuration-d' is further investigated by analyzing the bulk atoms. Interestingly, the typical fcc core arrangement is found to be totally lost and instead, a distorted icosahedral arrangement composed of 19 Au atoms is generated (**Figure IV.14-C**). This result is highly consistent with the experimental observation showing highly stable icosahedral-like structure of small-sized Au-NP under hydrogen atmosphere.

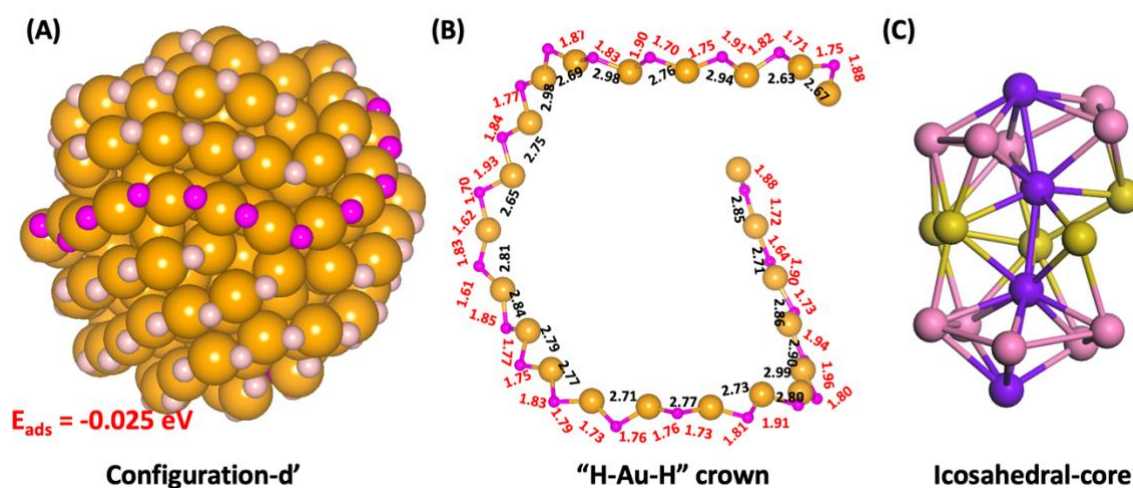
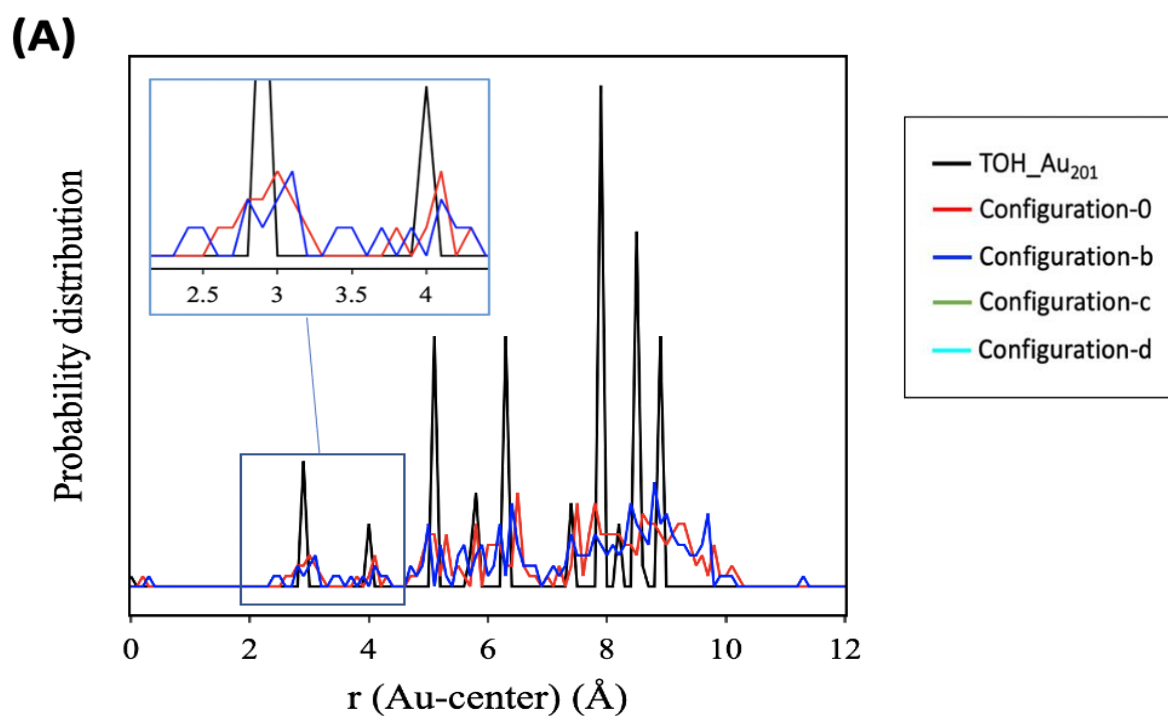


Figure IV.14 | . Structural analysis of Configuration-d'. (A) DFT optimized structure extracted from the last trajectory of AIMD simulation of hydrogenated Au-NP under 500 K. (B) Measured H-Au (red numbers) and H-H (black numbers) distances of one of the formed “H-Au-H” chains. (C) The core structure of Configuration-d' showing a distorted icosahedral arrangement.

To go further in the analysis of the atomic structure of the predicted hydrogenated gold NP, the probability distributions of Au atoms distances relative to the mass center of configurations extracted at different AIMD simulations are reported in **Figure IV.15**. The evolution of atomic probability distribution during simulation time, from its initial configuration (Configuration-0) to final configuration (Configuration-d), shows how the structure of Au-NP changes from fcc to non fcc symmetry. Thus, the initially well-distinguished peaks signature of ideal fcc-symmetry (black lines) especially the first two peaks representing for the core- and inner-shell, have progressively disappeared during the simulation time (the fcc-peaks are flattened and scattered progressively from **Figure IV.15-A** to **Figure IV.15-C**). This suggests a complete transition from fcc to non fcc structure.



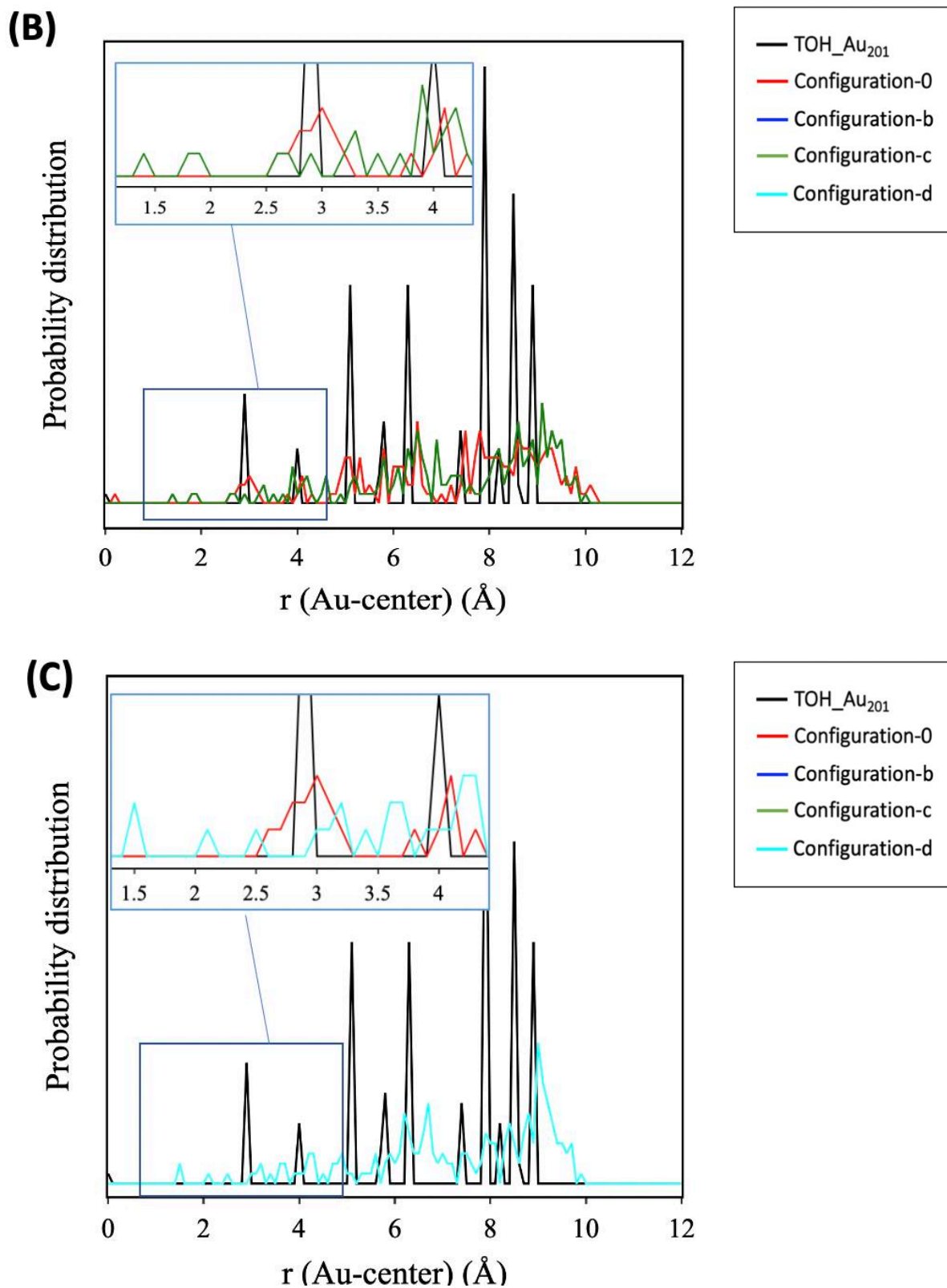


Figure IV.15 | The probability distribution functions of the Au atoms relative to the center of mass of the DFT pre-optimized TOh_Au₂₀₁, Configuration-0, Configurations b, c and d. The enlarged windows show the distributions at the core of the Au-NP.

Au-H and Au-Au bond formation and breaking processes

To analyze the mobility of hydrogen atoms on the Au-NP surface, several pairs of “H-Au” atoms are selected and the evolution of their relative distances are followed during the entire AIMD simulation time. As illustrated in the **Figure IV.16**, some hydrogen atoms show high mobility on the surface of Au-NP while others remain fixed in their initial adsorption site until the end of the simulation time. Thus, in **Figure IV.16-A** while the Au-H bond represented by the black curve remains at ~ 1.78 Å during the entire simulation time, the cyan curve shows bond dissociation at ~ 12 -ps. The Au and H atoms initially forming this bond do not meet again. In the **Figure IV.16-B** the bond formation of two Au-H pairs occurs after 30-ps and 40-ps. The hydrogen atoms initially located at distances of 5 and 8 Å from the selected gold atoms (the purple and blue curves), move closer and form stable Au-H bond of ~ 1.78 Å. Note that the formed “H-Au” pairs are bonded together to form one of the “H-Au-H” crowns (from 30-ps and 40-ps until the end 60-ps).

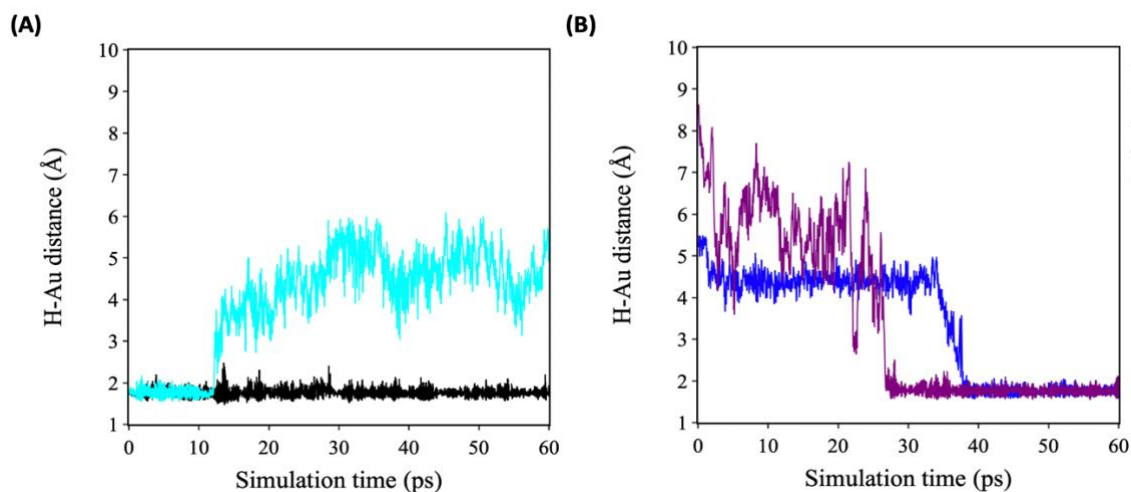


Figure IV.16]. High mobility of hydrogen atoms on the Au surface during AIMD simulation of hydrogenated-Au-NP under 500 K. (A) the evolutions of the relative distance between two pairs of “H-Au” that are initially neighboring atoms located on the surface of Au-NP. (B) the evolutions of the relative distance between two pairs of “H-Au” that are initially not bonded and located on the surface of Au-NP.

The **Figure IV.17**, reports the bond distance evolutions of several randomly selected Au atoms located in the surface (outer shell atoms **Figure IV.17-A1** and **-A2**), from the inner shell (**Figure IV.17-B**) and from the core (**Figure IV.17-C**) during the AIMD simulation under 500 K. The Au-Au bond distances of the atoms located on the outer-shell are found to fluctuate around an average distance, but no formation and bond breaking was recorded. In contrast, Au atoms located in the inner-shell and the core are found to be strongly mobilized. For instance, Au atom located in the inner-shell **Figure IV.17-B** is found to move toward the core (the red curve showing the Au-Au distance varies from $\sim 5 \text{ \AA}$ to $\sim 3 \text{ \AA}$). Other Au-atoms segregate from the core to the inner-shell of the Au-NP (**Figure IV.17-C**, blue- and cyan-curve showing the Au-Au distance varying from $\sim 3 \text{ \AA}$ to $\sim 5 \text{ \AA}$). The above bond profiles provide direct evidence of the drastic and dynamic structural transformations occurring during the AIMD simulations.

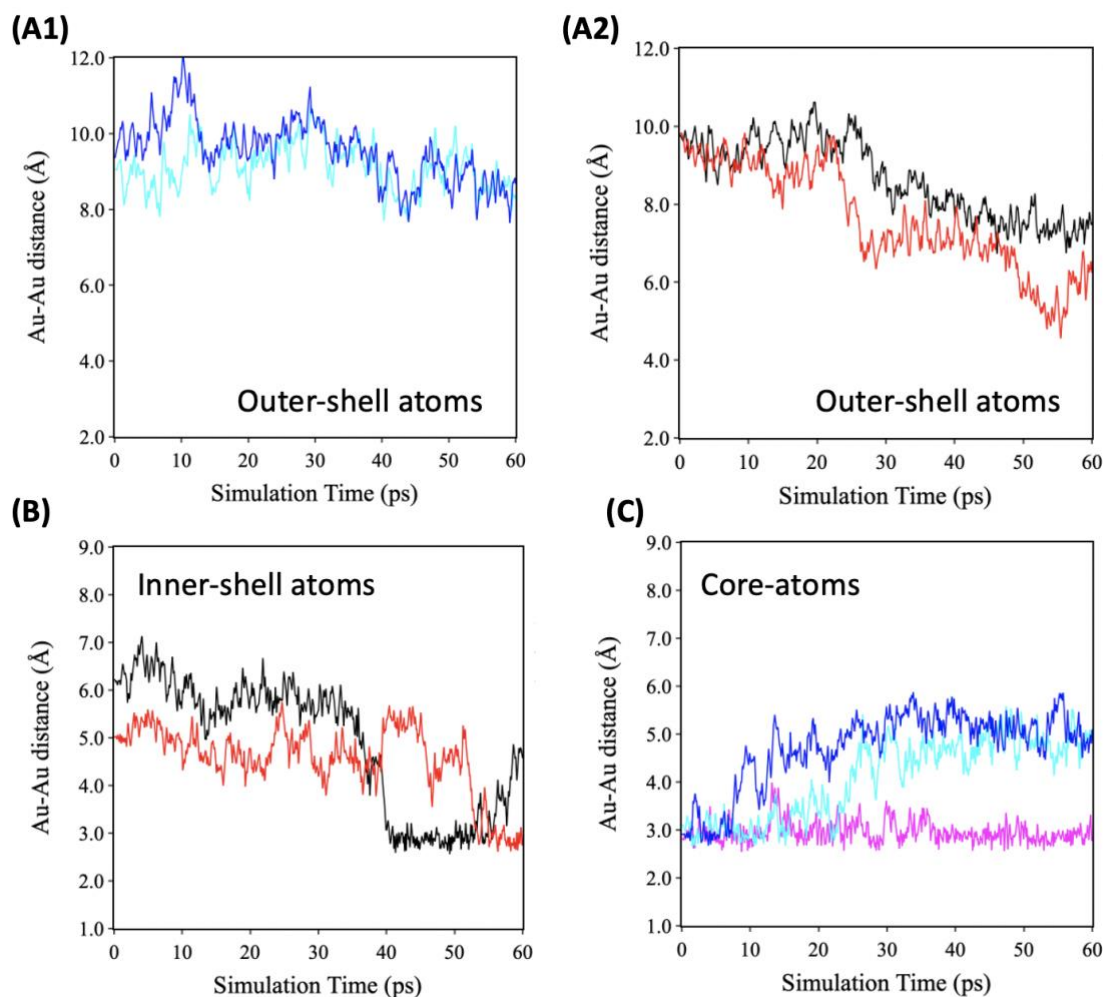


Figure IV.17]. “Au-Au” bond-forming and bond-breaking during AIMD simulation of hydrogenated Au-NP under 500 K. Evolution of bond distance for Au atoms: (A1) located in the outer-shell of Au-NP that stay all along of whole simulation time; (A2) located in the outer-shell of Au-NP that mobilized into the inner-shell geometries in the end of simulation; (B) located in the inner-shell of Au-NP; (C) located in the core of Au-NP. All distances monitored are related to the Au-atom located in the center of the Au-NP.

Electronic structure analysis

In order to understand the stability of the original surface structure of Au-NP formed in presence of hydrogen, we performed electronic structure calculations where the distribution of charge density (**Figure IV.18**) and the local density of states (DOS, **Figure IV.19**) of the Configuration-d' are analyzed.

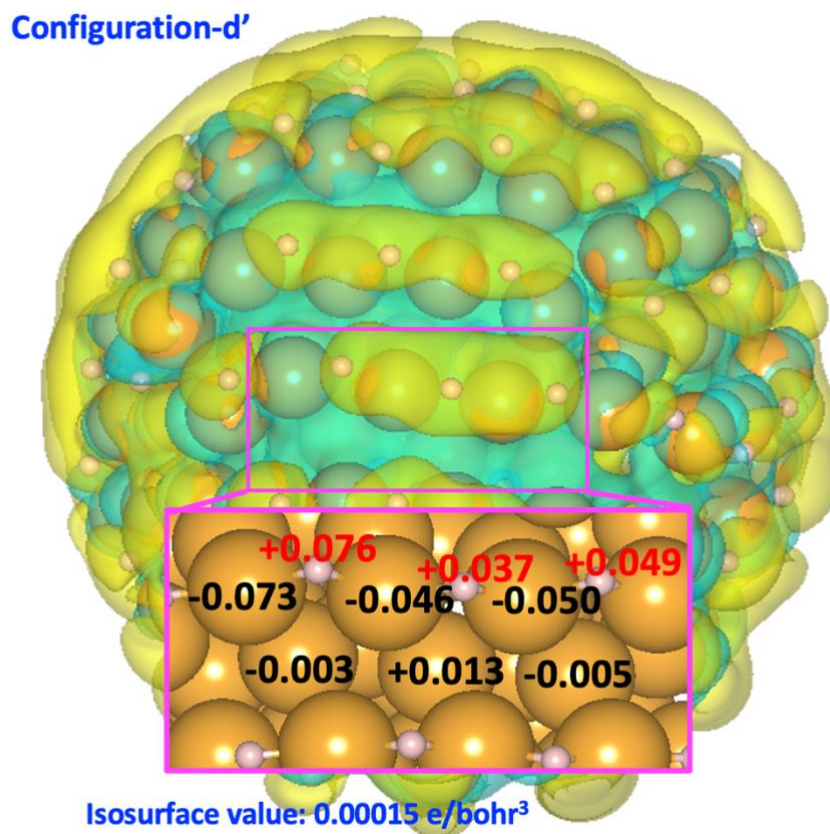


Figure IV.18 | 3D charge-density difference between the surface hydrogenated Au layer and the inner-shell of Configuration-d'. The isosurface value is 0.00015 e/bohr³. Color code: yellow, gaining electrons; blue, losing electrons. The inset represents the Bader charges of a selected region where red and black values are for hydrogen and gold atoms, respectively.

In **Figure IV.18** is represented the distribution of the charge density difference between the hydrogenated gold NP outer-shell, formed by “H-Au-H” chains and the rest of the NP atoms i.e., the inner-shell and the core atoms. The strong charge density accumulation is found on the “H-Au-H” chains, while the strong charge density depletion is on the inner-shells. Moreover, the Bader charge calculations over these two types of shells also show different charged states, where the Au located on the “crown-like” “H-Au-H” chains are more negatively charged (> 0.04 e units of elementary charge) than on the Au located in the inner-shells. These two distinct electronic structures suggest two types of accessible sites for the incoming reactants in hydrogenation catalytic reactions.

In **Figure IV.19**, the Au 5*d*-band density of states (DOS) for both Au surface and core atoms of Configuration-d' are compared with the Au 5*d*-band DOS of the “perfect” fcc Au-NP in TOh shape (TOh_Au₂₀₁).

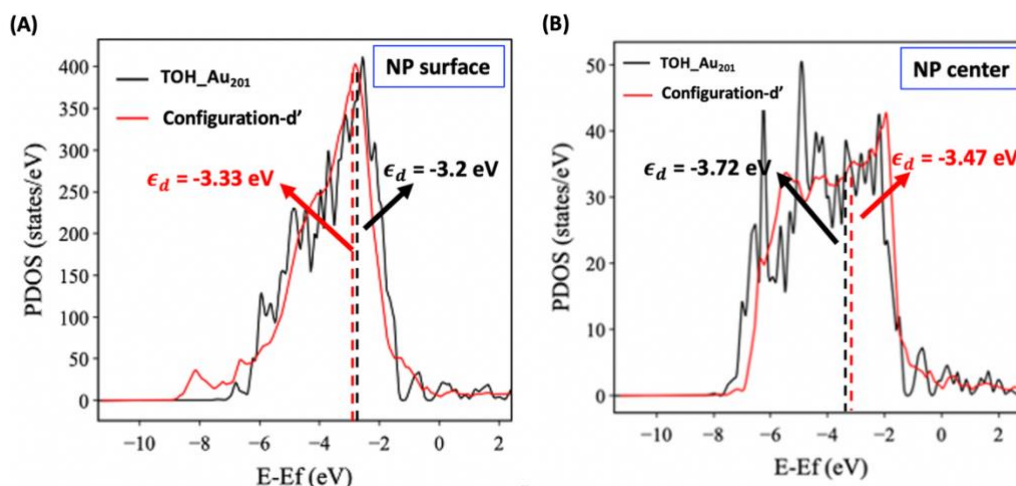


Figure IV.19]. Comparison of Au 5*d*-band density of states between the Configuration-d' and TOh_Au₂₀₁. (A) Au 5*d*-band of Au atoms in the outer-shell (the crown “H-Au-H” chains) of Configuration-d' and the top-surface layer of TOh_Au₂₀₁. (B) Au 5*d*-band of Au atoms in the core (19 atoms) of Configuration-d' and the core of TOh_Au₂₀₁ (13 atoms). Color code: red curves are for Configuration-d' and black curves are for TOh_Au₂₀₁. Their *d*-band centers are calculated and denoted as ϵ_d in the figures. E_f is the Fermi energy.

The DOS curves of hydrogenated gold NP are found to be quite different from the DOS of the perfect fcc TOh_Au₂₀₁ free from hydrogen. These formers are found to be narrowed which is in complete agreement with the theoretically predicted and experimentally observed transition from fcc to icosahedral-like symmetry [26]. For hydrogenated gold surface atoms, the *d*-band center (-3.33 eV) is found to “downshift” away from the Fermi level *d*-band center TOh_Au₂₀₁ (-3.2 eV), which is in line with the hydrogen-Au chemisorption. In contrast, the *d*-band center of core atoms is found to ‘upshift’ toward the Fermi level (-3.47 eV vs -3.72 eV), which may be the result of charge transfers for the benefit of the upper surface atoms. All these results open the way for a deep investigation of the reactivity of these revealed surface active sites to

understand accurately the reaction mechanisms occurring over hydrogenated gold nanocatalysts.

5. Summary and conclusion

In the framework of a collaboration with colleagues from the MPQ lab (Université Paris Diderot), environmental transmission electron microscopy observations (ETEM) were performed to study the structural evolution of gold nanocatalysts under reactive media. Particularly, the *in situ* atomic scale observations of individual Au-NPs complemented with *ex situ* TEM observations, show supported fcc Au-NPs undergoing dramatic structural changes in H₂ when their size is smaller than ~ 4 nm while no changes are observed for higher sized NPs. The initially well faceted TOh Au-NP with fcc symmetry, stable in presence of inert gas (similar to the under vacuum conditions), are found to transform to a rounded shape with an icosahedron-like symmetry. This result provided the first real space evidence of a size-dependent structural transformation in Au-NPs exposed to hydrogen confirming by the way, the importance of understanding the dynamic structural changes undergone by the gold nanocatalysts under realistic conditions.

In order to understand these observations and to explain at the atomic level the origin of the structural and symmetry transitions observed in small gold NPs, we performed AIMD simulations and DFT calculations on truncated octahedral (TOh) shaped Au-NP containing 201 Au atoms. The simulations were performed at two different temperatures of 300 and 500 K, under vacuum condition and in presence of 1 ML of adsorbed hydrogen atoms. The results show that hydrogen is chemisorbed on the gold NP surface and that this chemisorption induces transformation of the Au-NP from TOh shape to rounded shape with transition from the fcc to a icosahedron-like symmetry. These results are in full agreement with the experimental

observations. Moreover, the predicted AIMD configurations show original structure of the hydrogenated gold NP where surface gold atoms are found to stabilize in the form of a well-ordered crowned “Au-H-Au” lines sliding over a highly distorted gold center. The electronic structure analysis show electron accumulation over the surface hydrogenated Au lines and electron depletion in the valleys in between. This predicted picture is far from the conventional model of Au-NP catalysts often used in heterogeneous catalysis (well faceted NPs with rigid structure) to study the reactivity as is the case in hydrogenation catalytic reactions.

To conclude, by this work, we showed how AIMD simulation method is powerful and able to correctly predict the dynamic shape evolutions occurring under reactive conditions. These results provide the first evidence of hydrogen adsorption-inducing complete restructuring of small gold nanocatalysts and suggests the necessity of reinvestigating their reactivity through a more complete picture.

References

1. Haruta, M.; Kobayashi, T.; Sano, H.; Yamada, N., Novel Gold Catalysts for the Oxidation of Carbon Monoxide at a Temperature Far Below 0 °C. *Chemistry Letters* **1987**, *16*, 405-408.
2. Bond, G. C.; Sermon, P. A.; Webb, G.; Buchanan, D. A.; Wells, P. B., Hydrogenation over Supported Gold Catalysts. *Journal of the Chemical Society, Chemical Communications* **1973**, 444b-445.
3. Mohr, C.; Claus, P., Hydrogenation Properties of Supported Nanosized Gold Particles. *Science Progress* **2001**, *84*, 311-334.
4. Takei, T.; Akita, T.; Nakamura, I.; Fujitani, T.; Okumura, M.; Okazaki, K.; Huang, J.; Ishida, T.; Haruta, M., Heterogeneous Catalysis by Gold. 2012; pp 1-126.
5. Bond, G. C., Hydrogenation by Gold Catalysts: An Unexpected Discovery and a Current Assessment. *Gold Bulletin* **2016**, *49*, 53-61.
6. Bond, G. C.; Thompson, D. T., Catalysis by Gold. *Catalysis Reviews* **1999**, *41*, 319-388.
7. *Nanoparticles and Catalysis*; Wiley, 2007; Vol. 1.
8. Bond, G. C., The Effect of the Metal to Non-Metal Transition on the Activity of Gold Catalysts. *Faraday Discussions* **2011**, *152*, 277-291.
9. Bus, E.; Miller, J. T.; van Bokhoven, J. A., Hydrogen Chemisorption on Al₂O₃-Supported Gold Catalysts. *The Journal of Physical Chemistry B* **2005**, *109*, 14581-14587.
10. Hugon, A.; Delannoy, L.; Louis, C., Supported Gold Catalysts for the Reaction of Selective Hydrogenation of 1,3-Butadiene in the Presence of an Excess of Alkenes. *Gold Bulletin* **2008**, *41*, 127-138.
11. Gatin, A. K.; Grishin, M. V.; Dokhlikova, N. V.; Kolchenko, N. N.; Shub, B. R., The Effect of Hydrogen Adsorption on the Electronic Structure of Gold Nanoparticles. *Doklady Physical Chemistry* **2016**, *470*, 125-128.
12. Wijzenbroek, M.; Helstone, D.; Meyer, J.; Kroes, G. J., Dynamics of H₂ Dissociation on the Close-Packed (111) Surface of the Noblest Metal: H₂ + Au(111). *The Journal of Chemical Physics* **2016**, *145*, 144701.
13. Meyer, R.; Lemire, C.; Shaikhutdinov, S. K.; Freund, H. J., Surface Chemistry of Catalysis by Gold. *Gold Bulletin* **2004**, *37*, 72-124.
14. Howie, A., Introductory Lecture: Blazing the Trail from Metals to Nuclei. *Faraday Discussions* **1991**, *92*, 1-11.
15. Ueda, K.; Kawasaki, T.; Hasegawa, H.; Tanji, T.; Ichihashi, M., First Observation of Dynamic Shape Changes of a Gold Nanoparticle Catalyst under Reaction Gas Environment by Transmission Electron Microscopy. *Surface and Interface Analysis* **2008**, *40*, 1725-1727.
16. Chmielewski, A., et al., Reshaping Dynamics of Gold Nanoparticles under H₂ and O₂ at Atmospheric Pressure. *ACS Nano* **2019**, *13*, 2024-2033.
17. Kubo, R., Generalized Cumulant Expansion Method. *Journal of the Physical Society of Japan* **1962**, *17*, 1100-1120.
18. Halperin, W. P., Quantum Size Effects in Metal Particles. *Reviews of Modern Physics* **1986**, *58*, 533-606.
19. Valden, M.; Lai, X.; Goodman, D. W., Onset of Catalytic Activity of Gold Clusters on Titania with the Appearance of Nonmetallic Properties. *Science* **1998**, *281*, 1647-1650.
20. Bond, G. C.; A Louis, C.; A Thompson, D. T., *Catalysis by Gold*; Imperial College Press, 2006.
21. Nosé, S., A Unified Formulation of the Constant Temperature Molecular Dynamics Methods. *The Journal of Chemical Physics* **1984**, *81*, 511-519.

22. Hoover, W. G., Canonical Dynamics: Equilibrium Phase-Space Distributions. *Physical Review A* **1985**, *31*, 1695-1697.
23. Kresse, G.; Hafner, J., Ab Initio Molecular Dynamics for Liquid Metals. *Physical Review B* **1993**, *47*, 558-561.
24. Perdew, J. P.; Wang, Y., Accurate and Simple Analytic Representation of the Electron-Gas Correlation Energy. *Physical Review B* **1992**, *45*, 13244-13249.
25. Grimme, S., Accurate Description of Van Der Waals Complexes by Density Functional Theory Including Empirical Corrections. *Journal of Computational Chemistry* **2004**, *25*, 1463-1473.
26. Mottet, C.; Trégliat, G.; Legrand, B., Electronic Structure of Pd Clusters in the Tight-Binding Approximation: Influence of Spd-Hybridization. *Surface Science* **1996**, *352-354*, 675-679.

Chapter V

Modeling Pt based alloys under hydrogen

media: from single atom to host surface

1. Introduction

Bimetallic nanoparticles (NPs) have attracted growing attention because of their improved catalytic properties compared to monometallic ones. In the recent decade, several works have showed that the addition of a second metal to a given metallic catalyst, increases its catalytic activity and/or selectivity performances [1-2]. However, as the bimetallic NPs are composed of two different types of metal atoms, in addition to the possible structural re-shaping underwent by the nanocatalysts, surface composition evolutions may occur during reaction conditions. Indeed, it is now well established that the surface composition of bimetallic NPs may be modified when exposed to reactive (gas) environments, driven by the changed strain effects and the different bonding-strengths of metals to the adsorbates. This is manifested as the enrichment of the surface or of the bulk by one of the components. This process is called the surface/bulk segregation phenomena. Thus, predicting the chemical ordering changes on the surface of bimetallic NPs is essential for understanding and controlling the performances of catalysts.

Among all bimetallic nanoparticle catalysts, platinum-based alloys are the most efficient and indispensable in many chemical reactions, particularly in heterogeneous catalysis and electrocatalysis. Meanwhile, due to the scarcity and the high price of the platinum, it is highly

relevant to reduce its usage by adding other metals while maintaining and even improving its catalytic performance. Moreover, using *in situ* and *operando* experimental techniques [3-6] as well as DFT method [7-8], several works have reported surface or bulk segregation behaviors induced by the presence of adsorbates for a number of Pt-based bimetallic systems. For instance, R. Cuenya *et al.* [6] have reported experimental evidences of segregation trends on Ni/Pt nanoparticles as a function of reactive gas pressure. Using environmental XPS techniques, these authors measured the evolution of Ni/Pt surface ratio of Ni/Pt-NPs exposed to 1 bar of CO. The results show an increase of Ni/Pt ratio from 0.7 at 298 K (Pt-rich) to 1.5 at 673 K (Ni-enriched), followed by a decreased ratio until 0.7 (Pt-rich) at 873 K.

From theoretical point of view, the study of the segregation behavior of alloy systems is generally performed under vacuum conditions. For the few available works accounting for the presence of adsorbed gas, the employed theoretical methodologies are mainly stationary approaches. More precisely, the theoretical approaches generally consist in considering an initial system A in presence of adsorbed molecules (most often one adsorbed molecule) with an impurity B located in the bulk and a final system where such impurity B is in the surface of system A, directly interacting with the adsorbed gas molecule. Then the segregation energy is calculated as the energy difference between the final and the initial systems. The problem is that this static model does not include the dynamic changes of reaction conditions (temperature and gas pressure) under working conditions.

Very recently, Zhu *et al.* [9] proposed an improved environmental segregation energy model for surface segregation (E_{eseg}) evaluation of bimetallic alloy under temperature and pressure changes, using DFT calculations coupled with Fowler-Guggenheim adsorption isotherm that includes the gas coverage and the lateral interaction effects. This approach has been shown

effective to predict the surface composition evaluation of several bimetallic alloy systems under varying temperature and pressure.

During my thesis, I spent one month of visiting program in the Zhu's lab in Shanghai and I learned about using this environmental segregation model to study my systems. I investigated the evolution of segregation behavior of several Pt-based alloy systems under various temperatures (T) and hydrogen gas pressures (P). I focused on the two diluted states of these alloyed systems. More precisely, I started by studying the Pt as a single-atom diluted in 8 selected transition metal (M) surfaces (M = Cu, Ag, Au, Ni, Pd, Co, Rh, Ir). Then, I considered Pt as a host surface of the same M single-atoms and I studied their segregation behaviors for the same range of temperature and hydrogen pressure. Thus in this chapter, I will start by presenting the results of Pt single-atom alloy systems named dilute-Pt/M alloys (**Section 3.A**), which were published in the journal of *Applied Surface Science* [10]. Then, in **Section 3.B**, I will detail the results obtained on single-atoms M diluted in Pt surfaces systems named dilute-M/Pt alloys (publication under preparation).

2. Computational Details

The DFT spin-polarized calculations were performed using Vienna Ab initio Simulation Package (VASP) [11] with the Perdew, Burke, and Ernzerhof (PBE) functional [12]. The valence electrons were treated explicitly, and their interactions with the ionic cores were described by the projector augmented-wave method, which allows the use of a low cut-off energy equals to 400 eV for the plane-wave basis.

In order to evaluate the environmental segregation trends of bimetallic alloys, 4 types of slab models (**Figure V.1**) were constructed, corresponding to the position of the impurity B in host

metal A. Three low index surfaces, (1 1 1), (1 0 0) and (1 1 0) are selected because as it was demonstrated in chapter 3, they represent the most dominant facets of stable Pt nanoparticles. Two sizes of unit cells of selected facets (hkl) were constructed: (3 × 3) and (1 × 1) unit cells, which are both separated by 15 Å of vacuum space containing 6 atomic layers from which the bottom two layers are fixed on the bulk atom positions. The Brillouin zone integrations are performed with a Monkhorst-Pack (3 × 3 × 1) k -point mesh for the (3 × 3) unit cells and (6 × 6 × 1) k -point mesh for the (1 × 1) unit cells.

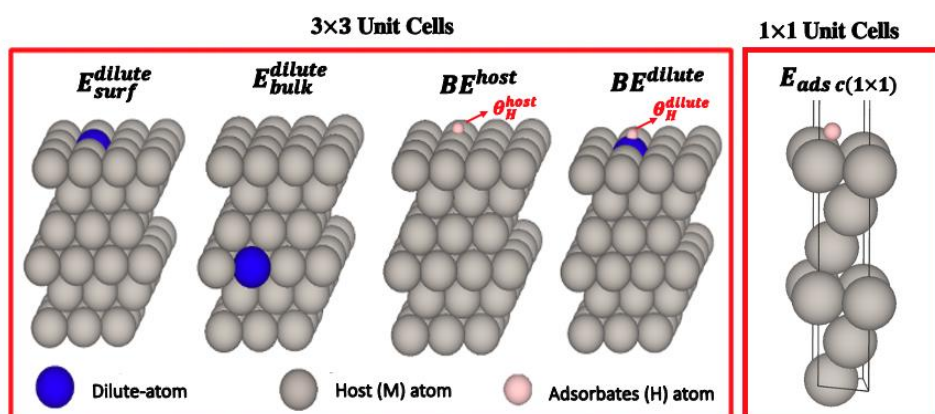


Figure V.1 | DFT surface slab models constructed for environmental segregation model.

Single-atom Pt diluted in M-host surfaces: For the study of single atom Pt catalyst, the Pt metal atom is taken as diluted in host-M surfaces ((3 × 3) unit slab models) M(1 1 1), M(1 0 0) and M(1 1 0) (M = Cu, Ag, Au, Ni, Pd, Co, Rh, Ir). To be noticed that in the case of host Cobalt surface, only the most stable surface Co(0 0 0 1) is considered.

Single-atom M diluted in Pt-host surfaces: Metal atom M (M = Cu, Ag, Au, Ni, Pd, Co, Rh, Ir) is taken as the single-atom M diluted in (3 × 3) unit slab models: Pt(1 1 1), Pt(1 0 0) and Pt(1 1 0) surfaces.

Under vacuum segregation energy (E_{seg}) and environmental segregation energy (E_{eseg})

The segregation energy (E_{seg}) under vacuum is defined as the energy difference between a system where the single-atom is diluted in the topmost host surfaces (E_{surf}^{single}) and the system where the single-atom is diluted in the bulk geometry (E_{bulk}^{single}) of host surfaces, i.e., in the 4th layer of our 6 layers slab:

$$E_{seg} = E_{surf}^{single} - E_{bulk}^{single} \quad (\text{V.1})$$

When the hydrogen is introduced into the alloy, the gas-induced segregation energy E_{eseg} is described as below:

$$E_{eseg} = E_{seg} + (E_{ads}^{single} \theta_H^{single} - E_{ads}^{host} \theta_H^{host}) \quad (\text{V.2})$$

where the E_{ads}^{single} and E_{ads}^{host} are the average adsorption energy of atomic hydrogen on the single-atom site and on the surface of host metals, θ_H^{single} and θ_H^{host} are the coverage of adsorbed hydrogen atom on the dilute sites and host sites, respectively.

According to the definition, if E_{eseg} or E_{seg} is sufficiently negative, the metallic single-atom is stable on the surface. Conversely, it segregates to the bulk when E_{eseg} or E_{seg} is sufficiently positive.

Binding Energy BE^{host} and BE^{single}

The adsorption energies (E_{ads}^{single}) and (E_{ads}^{host}) are coverage-dependent due to the non-negligible lateral interaction (w) between the neighboring adsorbed molecules:

$$E_{ads}^{host} = BE^{host} - zW\theta_H^{host} \quad (\text{V.3})$$

and

$$E_{ads}^{single} = BE^{single} - zW\theta_H^{host} \quad (\text{V.4})$$

with z representing the number of nearest neighboring adsorbates. BE^{host} is the binding energy of the isolated adsorbate on the host surface. BE^{single} is the binding energy of adsorbate on the single-atom inserted in the host surface.

Lateral Interaction (zw)

The lateral interaction is evaluated as the hydrogen adsorption energy difference between the (1×1) and (3×3) M-host surfaces, representing full adsorbates coverage ($\theta_H = 1$) and extremely low coverage ($\theta_H = 1/9$), respectively.

Fowler-Guggenheim Theorem: Gas Coverage (θ_H^{single} , θ_H^{host}) and Entropy (S_{gas} , S_{ads})

The Fowler-Guggenheim (F-G) adsorption formalism is employed to describe the evolution of hydrogen coverage on single-atom Pt site (θ_H^{single}) and on host atom site (θ_H^{host}), and the coverage θ is temperature (T), pressure (P), and adsorption energy dependent:

$$PK = \frac{\theta_H^{host/single}}{1 - \theta_H^{host/single}} e^{-c\theta_H^{host}}, c = \frac{zW}{RT} \quad (\text{V.5})$$

$$K = \exp\left(-\frac{BE^{host/single} - T(S_{ads} - S_{gas})}{RT}\right) \quad (\text{V.6})$$

where K is the adsorption equilibrium constant, S_{ads} is the entropy of adsorbed gas assumed to stick on the surface, and S_{gas} is the entropy of gas phase molecule that is considered to be equal to zero. The S_{gas} is dependent on T and P :

$$S_{gas} = S_{gas}(T, P^0) - R \ln\left(\frac{P}{P^0}\right) \quad (\text{V.7})$$

$S_{gas}(T, P^0)$ is the gas entropy at 1 atmosphere pressure (P^0) as a function of T , which is fitted based on the data from the NIST-JANAF Thermochemical Tables [13], **Figure SI-III.1**.

Mapping segregation energy (E_{eseg}) of single-atom as a function of (T, P)

In this chapter, considering hydrogen as the reactive gas, the segregation energies of single-atom dispersed in bimetallic surfaces are studied under the pressure range of 1 - 10^6 Pa and the temperature range of 200 - 1200 K, which covers most of experimental working conditions. The predicted environmental segregation energy E_{eseg} of single-atom for both bimetallic systems are color-coded as a function of temperature and hydrogen pressure and are plotted in contour-figures. The color code of the contour plots is defined as follows: positive values of E_{eseg} superior to +0.7 eV (dark blue), between +0.7 and +0.3 eV (light blue) and between +0.3 and +0.05 eV (aqua) represent the ‘very strong’, ‘strong’ and ‘weak’ bulk segregation of dilute-atom, respectively. The negative values of E_{eseg} inferior to -0.7 eV (red), between -0.3 and -0.7 eV (orange) and between -0.05 and -0.3 eV (yellow) represent the ‘very strong’, ‘strong’ and ‘weak’ surface segregation of dilute-atom, respectively. When E_{eseg} is between -0.05 and

+0.05 eV (light green), single-atom is considered as stable on the surface as in the bulk (no segregation preference).

The predicted environmental segregation energy for two systems are presented and discussed separately, in **Section 3-A** and **Section 3-B** and all calculated DFT energetic values issued from the different binary systems are depicted in **Table SI-V.1**.

3. Results and Discussions

3.A. Single-atom Pt diluted in M-host surfaces

3.A.1 Environmental segregation of single-atom Pt diluted in M-host surfaces

The study of Pt diluted in M-host surfaces highly integrates the recently emerged hot topic called “single-atom alloys (SAAs) systems” [14]. By definition, SAAs are a type of catalysts where the active metal atom (i.e., Pt in this case) is isolated into the relatively inert host-metal surfaces while exhibiting improved catalytic performance with optimal metal utilization. Following this idea and in attempt to find an alternative way for reducing the amount of Pt as a scarce noble metal and potentially enhancing its catalytic selectivity, Pt-based single-atom alloys (SAAs) have generated significant interest [15-16].

The most important challenge for stabilizing the SAA catalysts is to prevent the sintering and/or segregation phenomena, especially in presence of gas or solvent. As explained above, the segregation process leads to an enrichment of one of the alloy components at the surface or into the bulk, depending on the affinity of each alloy component with the gas environment. The sintering phenomena is governed by the high surface mobility and diffusion of atomically dispersed metal species and results in the aggregation of SAAs to form clusters of few atoms

on the surface [17-21]. The sintering of singly dispersed metal atoms into clusters and nanoparticles has been observed for many SAAs [22-23].

Although the metal segregation has been commonly observed in bimetallic nanoparticles under reaction conditions [24-27], the segregation and the stability of the isolated atoms in the SAAs have been rarely studied [28]. In this section, with a focus on the segregation phenomena thus leaving the sintering effect for a near-future scope, the evolution modes of segregation energies of single-atom Pt in different Pt-based SAAs and the effect of hydrogen on their stability will be presented.

Single-atom Pt diluted in coinage group host-metal surfaces

In **Figure V.2**, the E_{eseg} of single-atom Pt anchored in coinage group surfaces show interesting changes with increasing hydrogen pressure and/or decreasing temperature. The stability trends of single-atom Pt in Au and Ag host surfaces are very similar and evolve monotonically whereas non-monotonic changes were found in Cu(1 0 0) and Cu(1 1 0) host surfaces. For Au and Ag host surfaces (1 1 1), (1 0 0) and (1 1 0), the Pt is found to have a positive segregation energy under vacuum (see **Table SI-V.1**), which means that single-atom Pt could not be present on these host surfaces and prefers to stabilize in the bulk. This is an expected result as the surface energies of Au (1.5 J/m² [29]) and Ag (1.32 eV/atom [29]) are much lower than that of Pt surface (2.37 J/m² [30]).

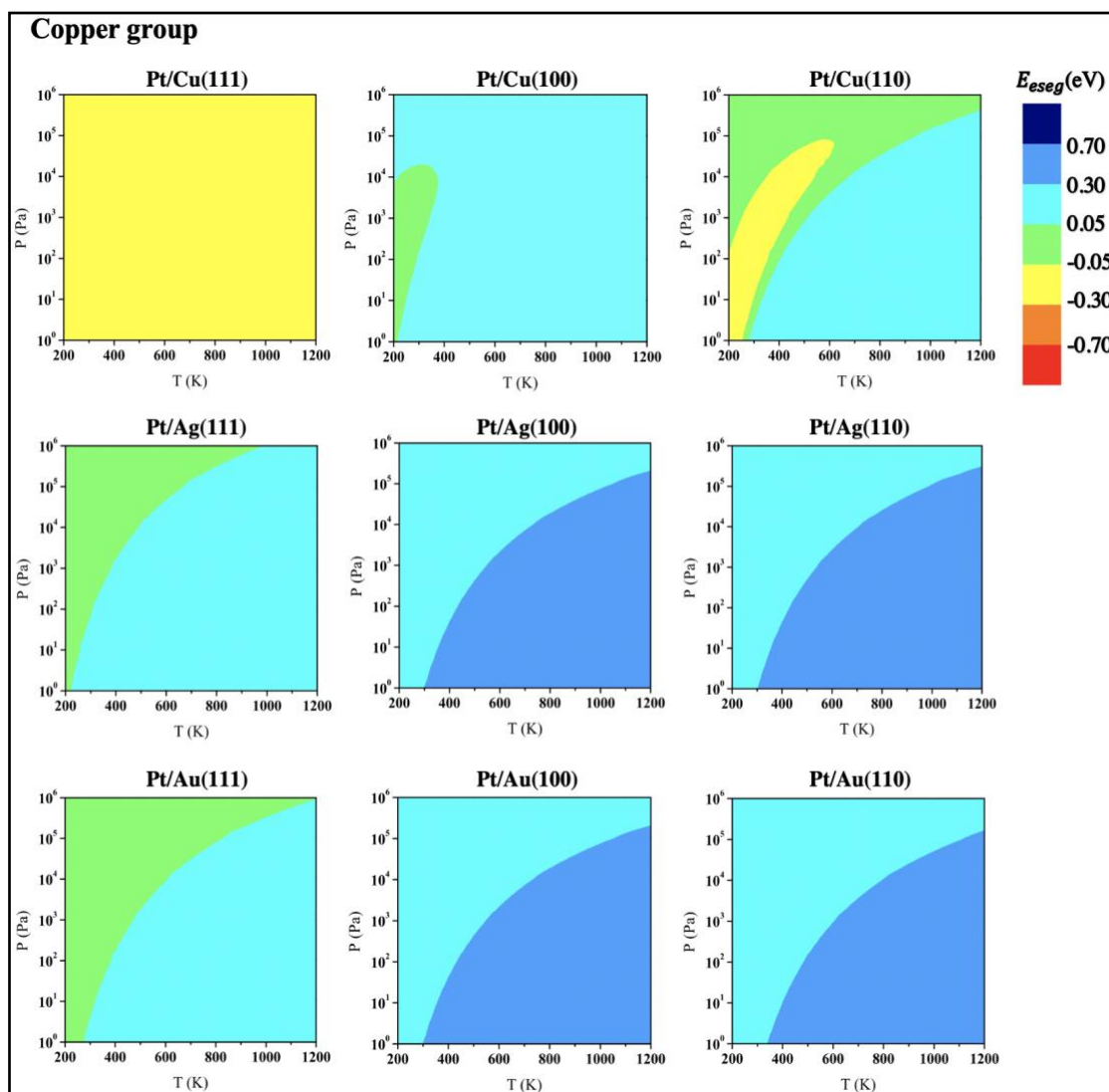


Figure V.2]. Color mapped environmental E_{eseg} of single-atom Pt as function of temperature (T) and H₂ pressure (P). Single-atom Pt is hosted by metal surface from Coinage group (Cu, Ag and Au). Negative segregation energies (dark red, orange and yellow) indicate surface segregation of single-atom Pt and its stability on the top-most layers of the host surface. Positive values (dark blue, light blue and aqua) indicate that single-atom Pt prefers to segregate toward the bulk. Light green color indicates the absence of segregation tendency.

Interestingly, hydrogen exposure seems not to alter this tendency. Indeed, the color changes in the counter plots from strong (light blue) to weak (aqua) bulk segregation and non-existing (light green) segregation with decreasing temperature and increasing hydrogen pressure, show that the probability to find single-atom Pt on these surfaces (Au and Ag) is negligible. In

contrast, in Cu(1 1 1), the surface segregation of single-atom Pt is found to be quite favorable under vacuum ($E_{seg} = -0.06$ eV) and could be preserved (yellow color) for the entire pressure and temperature considered ranges. When inserted in Cu(1 1 0), which represents edges of nanoparticles, the single-atom Pt could be only stabilized in the surface within a small temperature window of 300 - 500 K at 10^4 Pa of hydrogen pressure or at very low temperatures and pressures (lower than 300 K and 10^2 Pa). These temperature/pressure domains are governed by a competition between coverage of hydrogen on host Cu surface and on dilute-Pt sites as illustrated by **Figure SI-V.3**. These results are in agreement with the reported experimental work of Lucci *et al.* [31] showing the high selectivity for butadiene hydrogenation to butene under mild reaction conditions of copper nanocatalysts with dilute-site Pt dispersed in the surface. Moreover, these authors reported that under realistic pressures (1 bar) and at low loadings, Pt exists as individual isolated (substituted) atoms in the Cu(1 1 1) surface, these species ensuring stable activity and 100% selectivity. Several other recent works demonstrated the stability of Pt/Cu SAAs under hydrogen pressure [32] and in many selective hydrogenation and dehydrogenation reactions [33-36]. Therefore, the herein results bring a molecular picture of the surface under selected experimental conditions.

Single-atom Pt diluted in nickel group host-metal surfaces

Under vacuum conditions, the segregation behaviors of single-atom Pt in nickel and palladium surfaces are found to be opposite. Indeed, Pt surface segregation toward top-most surface nickel is favored whereas bulk segregation is predicted in Pd bulk. This behavior is in line with the surface energies order increasing from Pd (2 J/m² [29]) to Pt (2.37 J/m² [30]) and Ni (2.44 J/m² [30]).

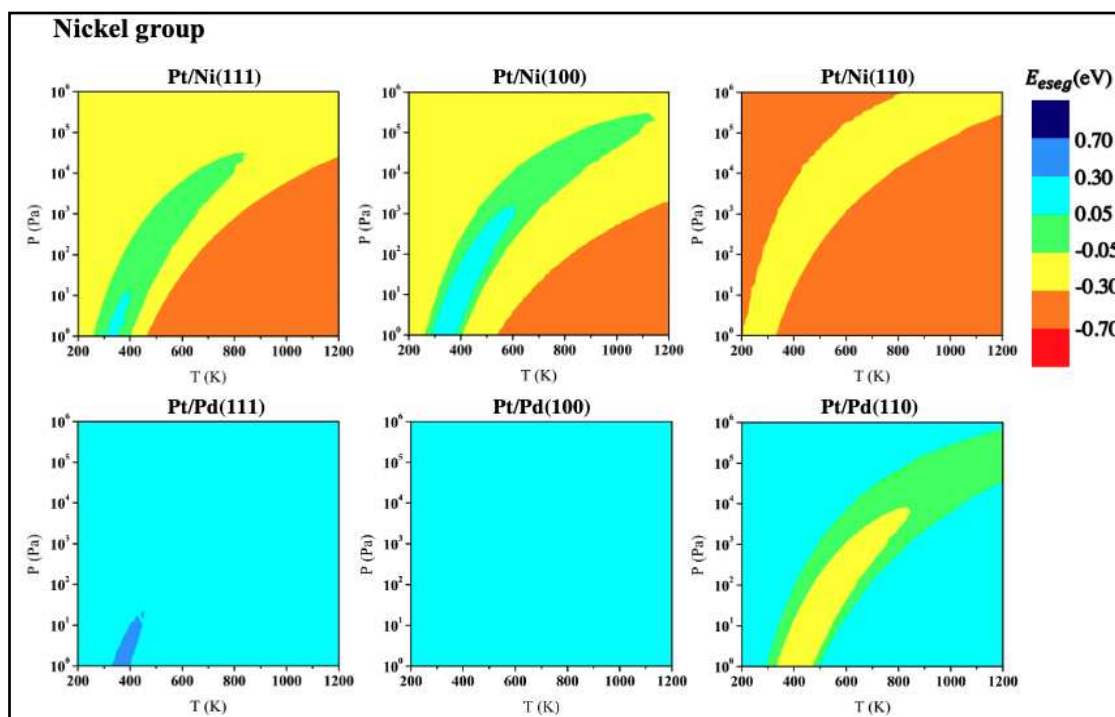
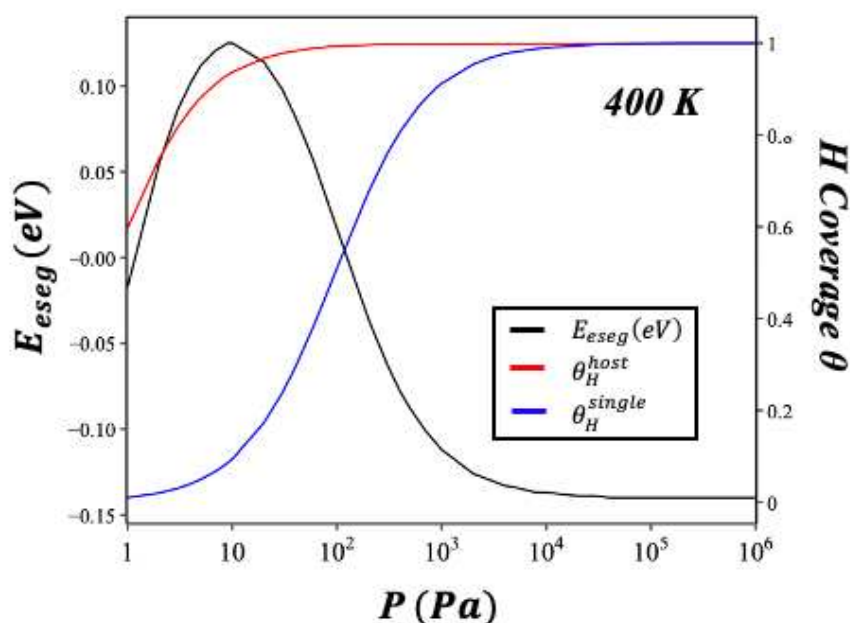


Figure V.3 | Color mapped environmental E_{eseg} of single-atom Pt as function of temperature (T) and H_2 pressure (P). Single-atom Pt is hosted by metal surface from Nickel group (Ni and Pd).

Figure V.3 shows that hydrogen pressure and temperature may affect the stability of single-atom Pt in Ni. This former remains stable on the surface for a wide range of temperatures and pressures except within a narrow window of temperature between 300 and 600 K and at very low hydrogen pressure (below 10^3 Pa), where it is found to segregate into the bulk of Ni(1 1 1) and Ni(1 0 0). To explain the changes within these narrow domains, we followed at fixed temperature of 400 K, the evolutions of E_{eseg} of Pt in Ni (1 0 0), the hydrogen coverage on surface host site θ_H^{host} and single-atom Pt θ_H^{dilute} as a function of hydrogen pressure (see **Figure V.4**). At 1 Pa pressure, the calculated E_{eseg} in Pt/Ni (1 0 0) is -0.01 eV. For this low pressure, the hydrogen already covers almost 0.6 ML of Ni surface sites. However, the coverage on single-atom Pt by hydrogen is near to zero. At this stage, the hydrogen has a negligible effect on the segregation behavior of single-atom Pt. With the pressure increasing from 1 to 10 Pa, the E_{eseg} increases monotonically. At 10 Pa, it reaches a maximum positive value of $+0.13$ eV.

The coverage of hydrogen on the host surface and on single atom sites is 0.9 ML and 0.10 ML, respectively. The hydrogen prefers to adsorb on the surface Ni atoms instead of Pt atoms (see **Table SI-V.1**). Such difference of adsorption preference prevented the segregation of the single-atom Pt. The E_{eseg} starts to decrease with the further increase in pressure. This is because the hydrogen on the Ni atoms reaches its maximum. Further increasing the pressure only increases the coverage on the single-atom Pt, which reduces the coverage difference, and consequently, the hydrogen adsorption effects on the segregation energy. Near 10^6 Pa, E_{eseg} decreases to -0.14 eV, which is higher than E_{eseg} at 1 Pa.



V.4. Evolution of environmental segregation energy of Pt (black line), hydrogen coverage on Ni host site (red line), hydrogen coverage on single-Pt site (blue line) as function of hydrogen pressure at 400 K (single-Pt/Ni(1 0 0) bimetallic alloy).

Recently, Peng *et al.* [37] have reported the high activity of Pt diluted atoms embedded in the surface of Ni nanocrystals toward the selective hydrogenation reaction of nitro compounds. The reactions were conducted at low temperature (313 K) and hydrogen pressure as high as 1-3 bar, conditions allowing the stabilization of single-atom Pt in the Pt/Ni SAAs.

In contrast with nickel, single-atom Pt could not be found in the surface of Pd under hydrogen pressure. Located in the bulk of Pd matrix under vacuum, it may remain stable for a wide range of temperatures and hydrogen pressures, except for the Pd(1 1 0) surface. In this latter, single-atom Pt is found to segregate toward the surface at a very narrow window of intermediate temperature and pressure (around $10^2 - 10^3$ Pa and 400 - 600 K). These results are in contradiction with the recent published work of Zhang *et al.* [38] who reported the fabrication of Pt/Pd SAA catalysts through an ALD method. According to these authors Pt atoms were successfully deposited on Pd nanoparticles with (1 0 0) and (1 1 1) surfaces, respectively. The as-prepared Pt/Pd SAA catalysts have been reported to exhibit much higher activities for hydrogen evolution reaction (HER) and oxygen evolution reaction (OER) than other types of ALD-prepared Pd/Pt catalysts. However, despite the thorough characterization work (XANES, EXAFS and XAS) showing the stabilization of such single-atom Pt in octahedral Pd nanoparticle surfaces, no evidence of its stability in the surface under operating conditions was given.

Single-atom Pt diluted in cobalt group host-metal surfaces

Under vacuum conditions, the segregation energies E_{seg} of single-atom Pt in Co(0 0 0 1), Rh(1 1 1) and Ir(1 1 1) are predicted to be of -0.63 eV, -0.32 eV and -0.53 eV, respectively. These negative values indicate the strong stability of Pt on the top surface of these alloys.

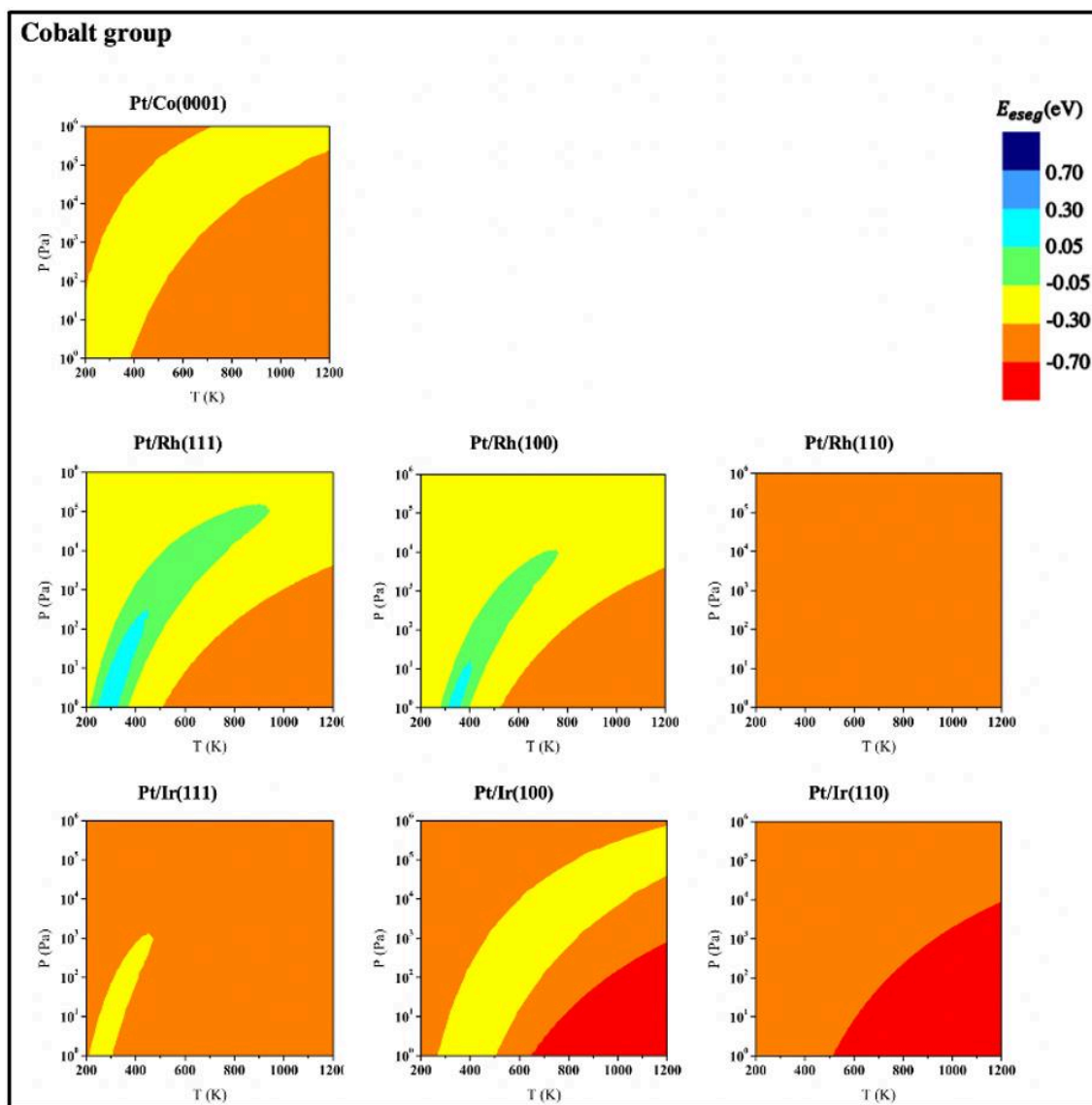


Figure V.5 | Color mapped environmental E_{eseg} of single-atom Pt as function of temperature (T) and H_2 pressure (P). Single-atom Pt is hosted by metal surface from Cobalt group (Co, Rh and Ir). For Co host surface, only the most stable (0001) surface orientation is considered.

In **Figure V.5**, the contour plots of E_{eseg} evolutions of single-atom Pt in Pt/Co, Pt/Rh and Pt/Ir SAAs are presented. From a general point of view, the hydrogen pressure and temperature do not seem to strongly alter the stability of Pt surface site. Except a very small window at very low pressure (less than 10^2 Pa) and around 300 K where single-atom Pt in Rh(1 1 1) and Rh(1 0 0) seems to prefer bulk segregation, the single-atom Pt is predicted to remain stable on the cobalt group metal surfaces. For Ir(1 0 0) and (1 1 0) surfaces, the surface segregation of Pt is

predicted to be strongly favored for high temperature. The high stability of single-atom Pt in cobalt group surfaces was recently demonstrated experimentally. Jiang *et al.* [39] have reported single-atom Pt decorating nanoporous cobalt selenide as efficient electrocatalysts for HER. Using Operando X-ray absorption spectroscopy technics, these authors show that single-atom Pt significantly reduces energy barriers of water dissociation and improves adsorption/desorption behavior of hydrogen.

To the best of our knowledge, no results are yet reported on single-atom Pt anchored in Rh or Ir metallic supports. Here we present the evidence of the high stability of these SAAs under hydrogen pressure and temperature conditions.

To compare the general behavior of single-atom Pt in all considered SAAs at the most common working pressure, we report in **Figure V.6**, the typical segregation trends that change with temperature under the hydrogen pressure of 10^5 Pa. Results obtained for lower pressures (100 Pa and 10^2 Pa) are reported in **Figure SI-V-1**.

Three classes of SAAs could be distinguished but not related to the position of the host metal group in the periodic table. Exposed to hydrogen pressure, single-atom Pt anchored in Au and Ag could not be stabilized in the surface and will segregate into the bulk. For Cu and Pd supports, surface segregation of Pt could be optimum only for definite orientations and under specific conditions. For Co, Rh, Ir and Ni, single-atom Pt is found to be stable on the surface in the quasi-totality of the pressure and temperature ranges, with exception for Rh and Ni where Pt is predicted to segregate into the bulk within a narrow window of low temperature and pressure. In order to understand this puzzling behavior of single-atom Pt in these metal supports, we analyzed the effect of hydrogen from binding energies and from electronic density of states (DOSs).

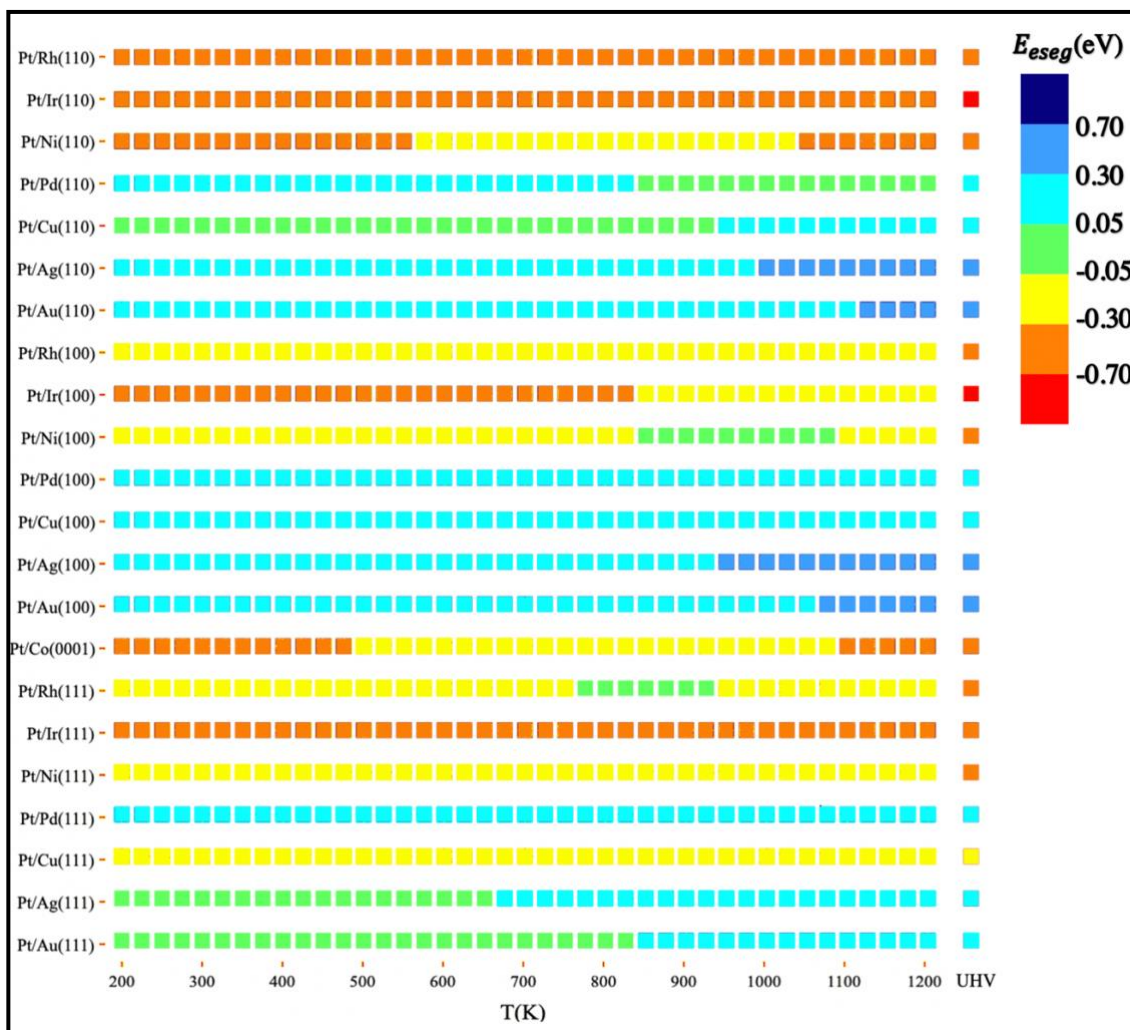


Figure V.6]. Evolution of the environmental segregation energy E_{eseg} of single-atom Pt in dilute-Pt/M alloys as function of temperature under 10^5 Pa of hydrogen gas pressure, compared with E_{seg} under vacuum (UHV).

3.A.2 Binding hydrogen energies and electronic density of states

Figure V.7 represents in one graph, the binding energies of hydrogen on pure host metallic (1 1 1) surfaces (free from single-atom sites) and on single-atom Pt sites anchored on these surfaces. The binding energy of hydrogen atom on pure Pt(1 1 1) surface is added for valuable

comparison. Two other graphs gathering computed hydrogen binding energies on (1 0 0) and (1 1 0) surfaces are provided in **Figure SI-V.2**.

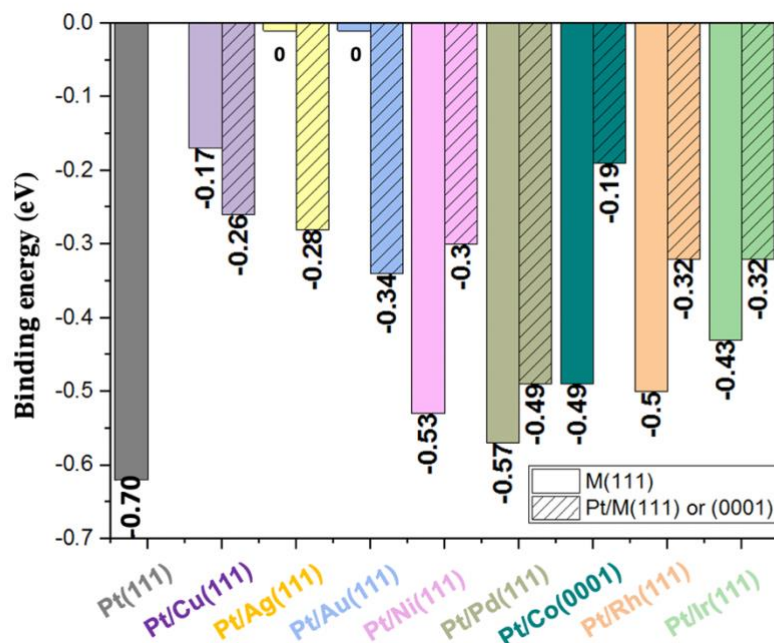


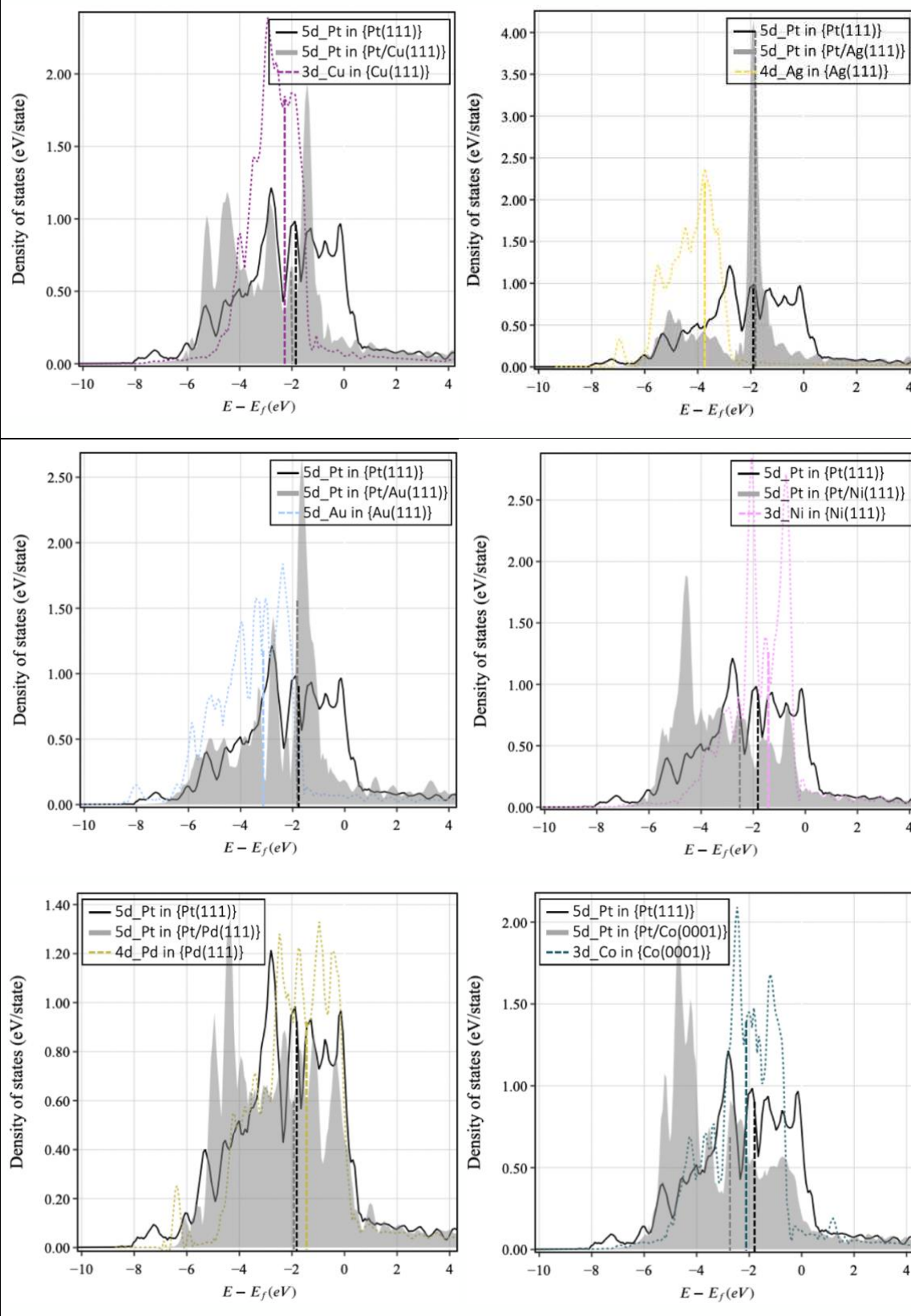
Figure V.7 | Binding energy comparison between pure M(1 1 1) host surfaces BE_{ads}^{host} and M(1 1 1) surfaces anchoring single-atom Pt BE_{ads}^{single} . For comparison, the binding energy of hydrogen on pure Pt(1 1 1) surfaces is indicated.

Generally, the expected response to adsorbates is that the more reactive alloy component (i.e., the one interacting more strongly with the adsorbates) segregates to the surface [40-44]. Contrary to this simplistic picture, the results on the considered SAAs show more complex behaviors. The results on Au(1 1 1) and Ag(1 1 1) surfaces, show that the most reactive component with hydrogen, i.e. the single-atom Pt, segregates toward the bulk. Indeed, the adsorption energy of hydrogen on Pt(1 1 1) is calculated to be of -0.62 eV while it is found to be endothermic on Au and Ag surfaces. The analysis of local density of states in presence of hydrogen (see **Figure V.8**) show that when single-atom Pt is located in the surface of Au(1 1 1) and Ag(1 1 1), its *d*-band is characterized by a pronounced narrow peak which lies below the Fermi level. Interestingly, the calculation of *d*-band centers (**Table SI-V.2**) shows negligible

shift between the $5d$ -band center of pure Pt(1 1 1) and single-atom Pt anchored in Au and Ag surfaces. For these latter nearly filled 1B metals, the position of the d -band centers is found to lie far away from the Fermi level in line with the calculated endothermic hydrogen binding energies. Thus, the non-stability of single-atom Pt could be explained by the fact that highly endothermic surface segregation under vacuum, could not be compensated by the mild binding energy of hydrogen on single-atom Pt of -0.28 eV and -0.34 eV in Ag(1 1 1) and Au(1 1 1), respectively.

The calculated binding energies of hydrogen on single-atom Pt in Cu(1 1 1) and Pd(1 1 1) compared with host surfaces are found to be competitive (0.09 eV in favor of single-atom Pt for the case of copper, and 0.08 eV in favor of host surface for the case of palladium). The calculated d -band centers of single-atom Pt vs. host surfaces are found to lie in the same energy ranges for the two systems, which is in agreement with the competitive binding energies. As the surface segregation of single-atom Pt in Cu(1 1 1) is slightly favored under vacuum, the better affinity of hydrogen toward Pt increases the stability of this latter under a wide range of temperatures and pressures. In contrast, for Pd, the better affinity of hydrogen for Pd induces the better stability of single-atom Pt in the bulk. For these two systems, the interplay between adsorption-driven surface segregation and surface orientation are found to induce different behaviors under reactive conditions.

Local density of state analysis of surface metallic atoms in presence of hydrogen



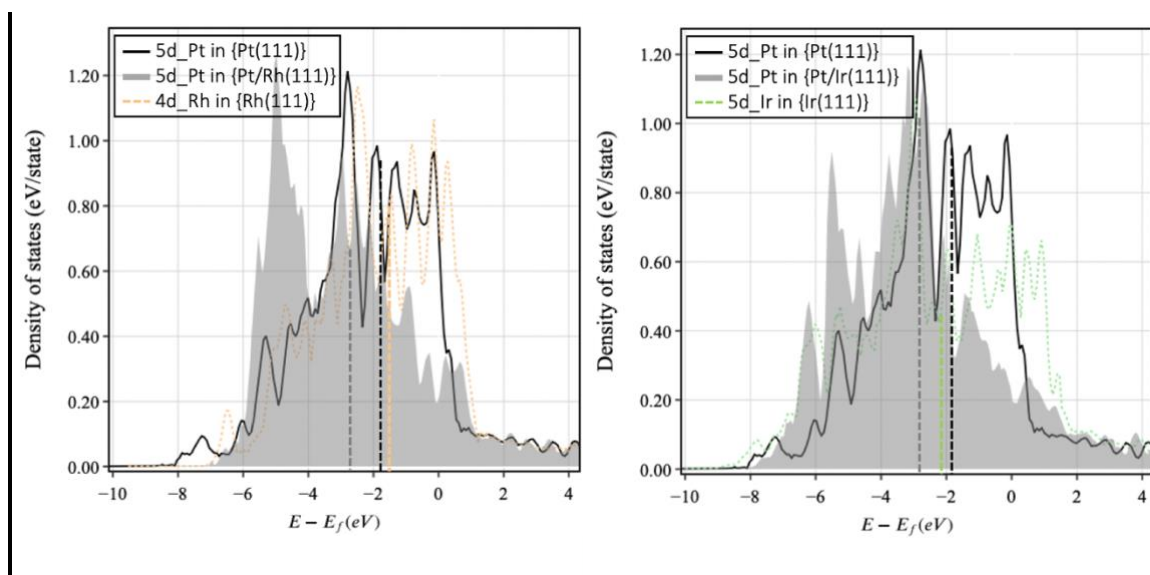


Figure V.8| *d*-band DOSs (state/eV) of Pt(1 1 1) (black line), of M(1 1 1) host metal surface (dashed colored lines) and of single-atom Pt in host metal surfaces (grey color). Dashed vertical lines correspond to the *d*-band centers relative to the Fermi energy ($E - E_f$ (eV)).

The binding energies of hydrogen interacting with single-atom Pt in the metallic Ni(1 1 1) (-0.3 eV), Co(0 0 0 1) (-0.19 eV), Rh(1 1 1) (-0.32 eV) and Ir(1 1 1) (-0.32 eV) surfaces are found to be lower than on host surfaces (see graph in **Figure V.7**). These results are in agreement with the calculated *d*-band centers of single-atom Pt found to lie much away from the Fermi level than the *d*-band centers of host metals. Despite the lower reactivity of single-atom Pt toward hydrogen, it is found to be stable on the surface because of its highly exothermic surface segregation under vacuum. These identified single-atom properties (high stability under hydrogen pressure and temperature and lower interaction with hydrogen) may be of great interest for specific catalytic reactions.

3.A.3 Section summary

In this section, we clearly demonstrated that the stability of dilute-atom Pt in Pt-based SAAs is changing under reactive conditions. Using the environmental segregation model, we provided a valuable picture of the surface stability of single-atom Pt within various metal-host surfaces

under different hydrogen pressures and temperatures. Three classes of SAAs could be distinguished:

- i) The Au and Ag surfaces, in which single-atom Pt exposed to hydrogen pressure could not be found because it will prefer to segregate into the bulk,
- ii) Copper and palladium supports, where the surface segregation of single-atom Pt could be optimum only for definite orientations (Cu(1 1 1) and Cu(1 1 0) for Pt/Cu and Pd(1 1 0) for Pt/Pd) and under specific hydrogen pressures and temperatures,
- iii) Co, Rh, Ir and Ni supports in which single-atom Pt could remain stable on the surface within the quasi-totality of the pressure and temperature ranges studied (200 -1200 K and 1 - 10⁵ Pa)

These results are in contrast with the intuitive image in which the more reactive alloy component (i.e., the one interacting strongly with the adsorbates) segregates to the surface. The reality is that the chemistry of diluted single-atom Pt is completely different from what is known from the extended surfaces and from clusters and nanoparticle. Its stability on the surface is an interplay between different properties and depends either on its modified electronic structure within the host material, its geometric ensemble (surface orientation) and its (new) affinity (as a single atom) with the reactive gas.

3. B. Single-atom M diluted in Pt-host surfaces

In order to go further in our understanding of the Pt-based bimetallic systems, we decided to study the opposite extreme diluted system of Pt/M (M = Cu, Ag, Au, Ni, Pd, Co, Rh, Ir) alloys, i.e., the earlier named “diluted M/Pt alloys” system of which the atoms “M” are diluted in Pt-host surfaces. The questions that we wanted to answer are:

- (i) How a given single transition-metal atom M may behave in the Pt surfaces and what are the ranges of temperature and hydrogen pressure allowing its stability in the Pt surfaces,
- (ii) How a single-atom M may affect the Pt-host surface atoms and their binding with hydrogen.

To answer these questions, the environmental segregation model was applied to map the evolution of segregation energies of single atoms M for the pressure range of 1 - 10^6 Pa and the temperature range of 200 -1200 K, and binding energies as well as electronic structures were computed and analyzed on the different considered M/Pt surfaces.

3.B.1 Single-atom M diluted in Pt-host surfaces

Figures V.9, V.10 and V.11 represent the mapped M single-atoms from coinage, nickel and cobalt groups diluted into Pt-host surfaces, respectively. These results show monotonic evolutions in all the three considered orientation Pt(1 1 1), Pt(1 0 0) and Pt(1 1 0), where the E_{seg} values decrease with increasing temperature and/or reducing hydrogen pressure. Interestingly, when analyzing the colored maps, we can see that the segregation behaviors of M diluted in Pt-host surfaces are not intuitive and are not, as it may be expected, simply a reversed segregation behavior of Pt in M-host surfaces. More precisely, if for a given range of pressure and temperature, Pt single-atom is not stable in the surface of M, reversibly the M single-atom is not systematically stable in Pt-host surface. As it will be detailed in the following

section, the segregation behavior of single M atoms is much more complex and cannot be predicted without calculations.

M single atoms from coinage group diluted in Pt-host surfaces

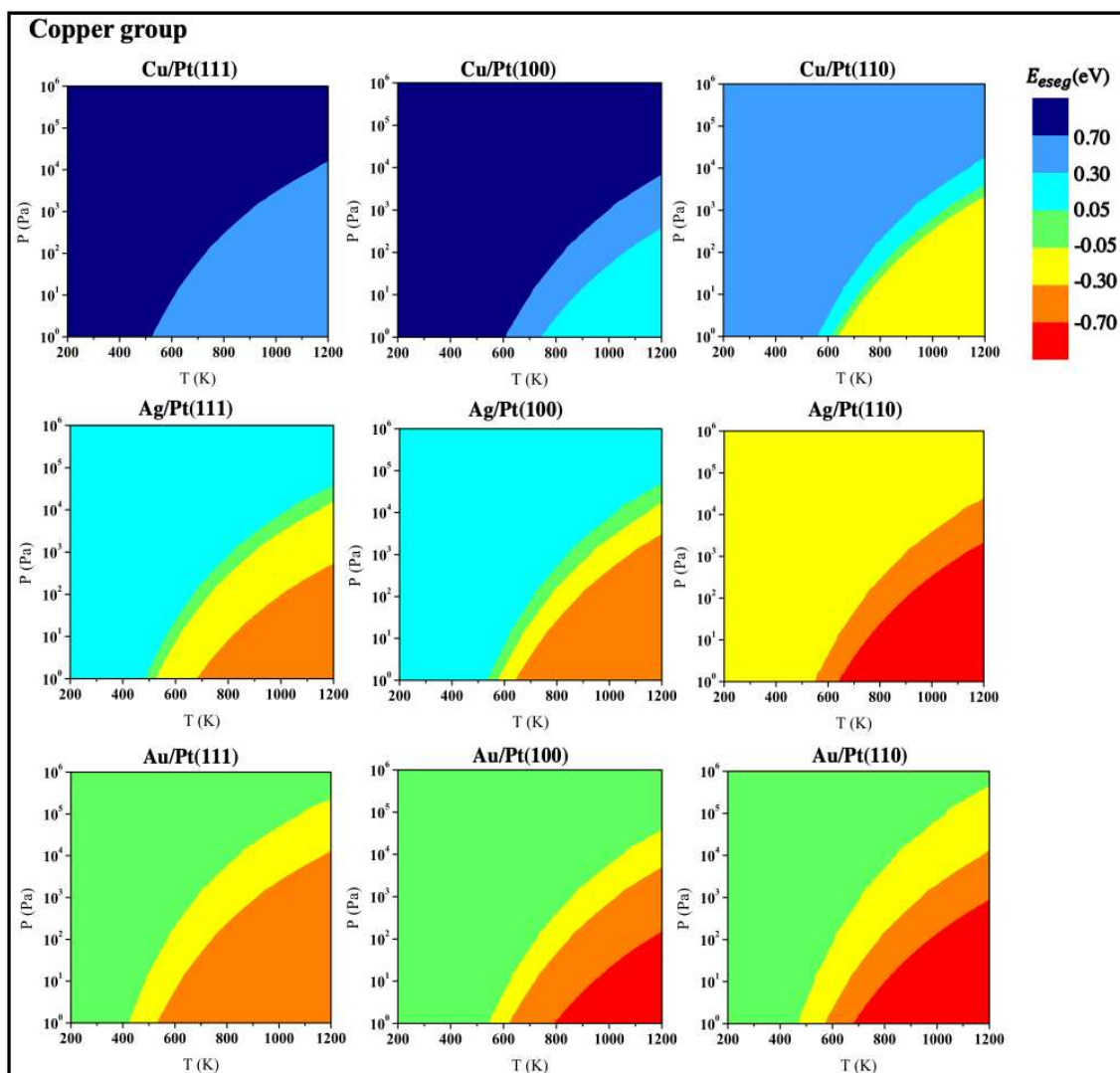


Figure V.9]. Color mapped environmental E_{seg} of M single-atoms ($M = \text{Cu, Ni, Co}$) in $\text{Pt}(1\ 1\ 1)$, $\text{Pt}(1\ 0\ 0)$ and $\text{Pt}(1\ 1\ 0)$ host surfaces as function of temperature (T) and H_2 pressure (P).

Under vacuum conditions, the segregation energies of Cu-single atoms are calculated to be $E_{seg} = 0.42$ eV in $\text{Pt}(1\ 1\ 1)$, $E_{seg} = 0.21$ eV in $\text{Pt}(1\ 0\ 0)$ and $E_{seg} = -0.24$ eV in $\text{Pt}(1\ 1\ 0)$. These values predict the strong stability of Cu in the bulk of $\text{Pt}(1\ 1\ 1)$ and $(1\ 0\ 0)$ and a surface stability in the upper layer of the more open $(1\ 1\ 0)$ surface. In presence of hydrogen pressure, the

mapped segregation energies show that Cu-single atom remains stable in the bulk of Pt(1 1 1) and (1 0 0) surfaces. This is based on the contour diagram which shows that the bulk-segregation trend of Cu increases from weak (aqua) in Pt(1 0 0) and strong (light-blue) in Pt(1 1 1) to very strong (dark-blue) with decreasing temperature and/or increasing hydrogen pressure. When diluted in Pt(1 1 0) surface, the Cu stability can be reversed from weak surface-segregation (light-yellow) into strong bulk-segregation (light-blue) with decreasing temperature and/or increasing hydrogen pressure. These results indicate that for moderate and high hydrogen pressure (10^4 - 10^6 Pa) conditions, the probability to find single Cu-atoms in the surface of Pt NPs is inexistent.

Considering the Ag/Pt and Au/Pt systems, under vacuum and at high temperature and low hydrogen pressures, single Ag and Au atoms are found to be stable in the surface of Pt (red, orange and yellow regions). This stability is lowered with increasing pressure and decreasing temperature. For temperature lower than 500 K and pressure varied from 1 to 10^6 Pa, the Ag and the Au single atoms are likely to be found in the bulk of Pt (1 1 1) and (1 0 0) surface. An exception is found for Ag in the surface of Pt(1 1 0) where the mapped surface segregation indicates a favorable surface segregation. From these results, one can extrapolate that under hydrogen pressure, single Ag atoms anchored in Pt NPs can be located at the edge sites while (1 0 0) and (1 1 1) facets remain free from Ag. This is in line with Gordon and Jones's experimental observations [45] reporting that on dilute-Ag/Pt system, low-levels of Ag atoms doping in the Pt-NP surface can promote C_2H_2 to C_2H_4 hydrogenation under excess H_2 at reaction temperatures from 373 to 673 K. For Au single atom, the mapped surface segregation indicates slight stability on the three surface orientations of Pt, and this stability increases with increasing temperature. This result also corroborates with XPS analysis of Wang *et al.* [46], who showed that for the initially "Pt-rich" Pt-Au NP ($Pt_{80}Au_{20}$), after the treatment under H_2 at

520 K, the surface content of Pt atoms is reduced ($\text{Pt}_{77}\text{Au}_{23}$), and when increasing temperature to 620 K, the Au atoms are enriched in surface of NP ($\text{Pt}_{61.9}\text{Au}_{38.1}$).

M single atoms from nickel group diluted in Pt-host surfaces

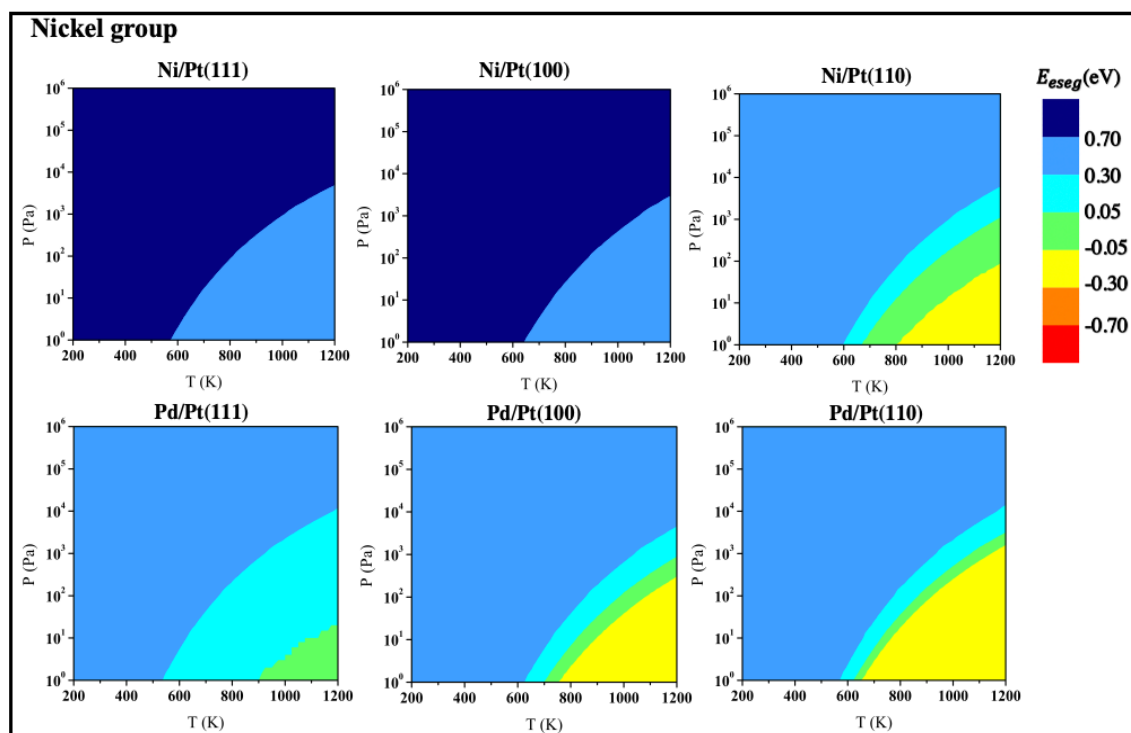


Figure V.10| Color mapped environmental E_{eseg} of single-M ($M = \text{Ni}, \text{Pd}$) in $\text{Pt}(1\ 1\ 1)$, $\text{Pt}(1\ 0\ 0)$ and $\text{Pt}(1\ 1\ 0)$ host surfaces as function of temperature (T) and H_2 pressure (P).

In contrast with the non-monotonic evolution of Pt-single atom in Ni host surfaces (see **Figure V.3**), the single-atoms Ni in the Pt-host surfaces (**Figure V.10**) is found to prefer the bulk for all investigated temperature and pressure ranges. The mapped E_{eseg} is found to be very similar to the previous dilute-Cu/Pt system in all 3 orientations. It is stable in bulk-segregation for all investigated temperature and hydrogen pressure ranges in $\text{Pt}(1\ 1\ 1)$ and $\text{Pt}(1\ 0\ 0)$ host surfaces and surface-segregation occurs for high temperature (higher than 800 K) and low hydrogen pressure (lower than 100 Pa) window of $\text{Pt}(1\ 1\ 0)$ host surface. The similarity of the two bulk-segregation behaviors of Cu and Ni in Pt-host surfaces may be linked to the smaller atomic radius (128 pm for Cu and 125 pm for Ni) compared to Pt (139 pm). Moreover, the smaller

cohesive energies [47] of Cu (3.49 eV/atom) and Ni (4.44 eV/atom) compared to Pt (5.84 eV/atom), as well as the lower surface energy [48] of Ni (1.25 J/m²) and Cu (1.28 J/m²) over Pt (1.39 J/m²), both favor the bulk-segregation of Cu and Ni, whereby they will have reduced strain effects and higher coordination [49].

Like under vacuum, single-atom Pd anchored in Pt (1 1 1) surface ($E_{seg} = 0.049$ eV) shows bulk-segregation preference in presence of hydrogen. The weak surface-segregation energies calculated in Pt(1 0 0) ($E_{seg} = -0.12$ eV) and Pt(1 1 0) ($E_{seg} = -0.20$ eV) surfaces (correspond to the yellow regions), change to bulk-segregation in presence of hydrogen. These results also show the weak probability to find single Pd atoms in the surface of Pt-NPs exposed to hydrogen.

M single atoms from cobalt group diluted in Pt-host surfaces

Under vacuum, the single-atom Co shows strong, very strong and weak bulk-stability in Pt(1 1 1) ($E_{seg} = 0.63$ eV), Pt(1 0 0) ($E_{seg} = 1.01$ eV) and Pt(1 1 0) ($E_{seg} = 0.058$ eV) host surfaces, respectively. In **Figure V.11**, when exposed to hydrogen environment, the tendency of Co segregating into the bulk-geometry is enhanced in all 3 investigated orientations.

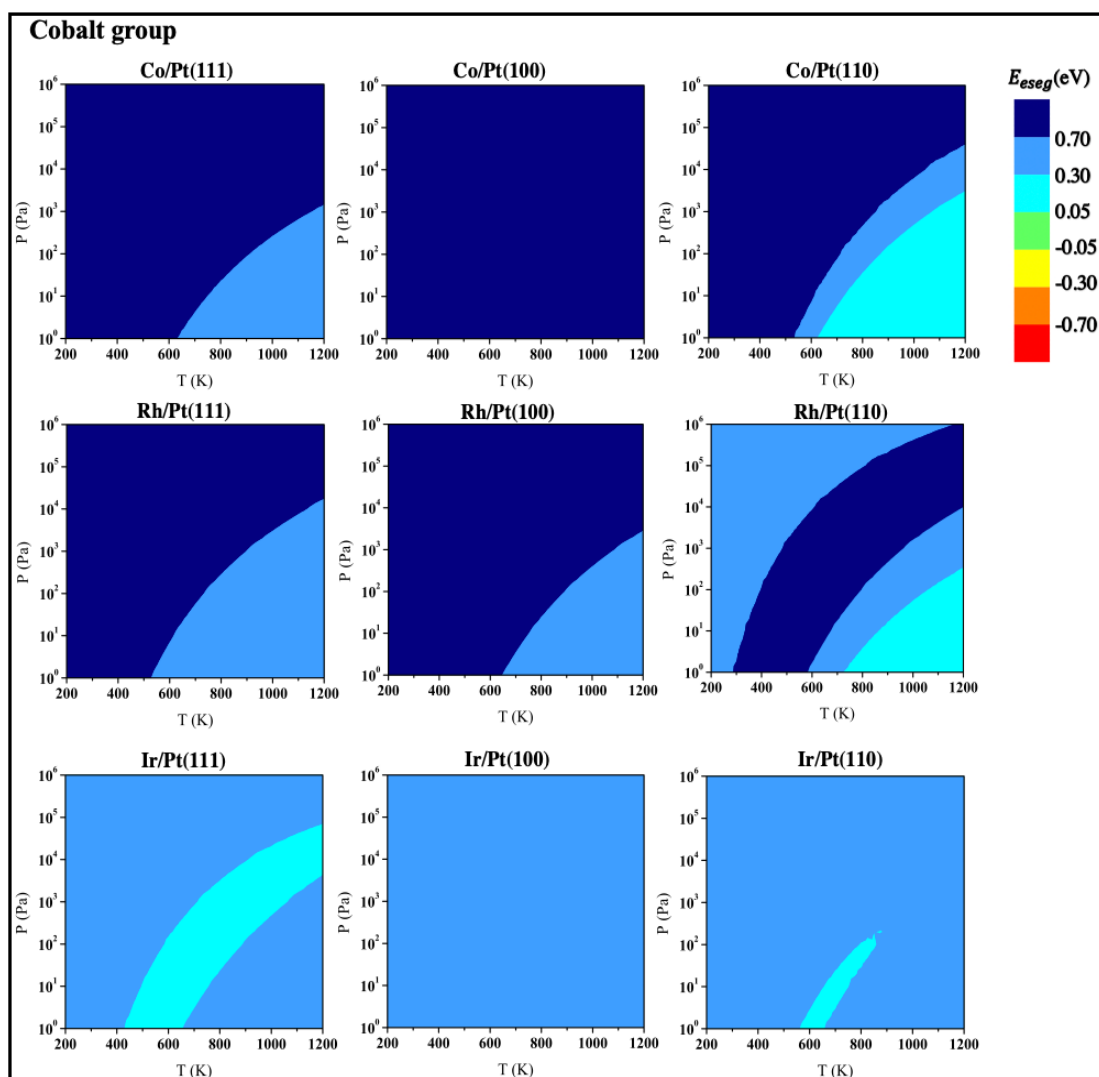


Figure V.11 | Color mapped environmental E_{eseg} of single-M ($M = \text{Co, Rh, Ir}$) in Pt(1 1 1), Pt(1 0 0) and Pt(1 1 0) host surfaces as function of temperature (T) and H_2 pressure (P).

Same as dilute-Co/Pt alloys, in vacuum condition, the single-atom Rh and Ir are both found to be more stable in bulk-geometry than in surface-geometry when diluted into Pt(1 1 1), Pt(1 0 0) and Pt(1 1 0). These predicted behaviors of the bulk segregation tendency of M single atoms from cobalt group in Pt corroborate with several reported experimental studies [50-51] of under vacuum observations. Unfortunately, no results exist under hydrogen pressure which makes our exploratory results very useful.

3.B.2 Binding hydrogen energy

In order to understand the monitoring effect of the segregation of single M atom in Pt surface, we analyze the energetic structure of the systems through the binding energy calculations. In **Table V.1** are depicted the binding energies of hydrogen interacting with single-M atoms anchored in Pt(1 1 1) host surfaces. Additionally, to evaluate how single-M atoms affect their neighboring Pt atoms, the hydrogen binding energies on the neighboring Pt (with M free from hydrogen) are also calculated (see histogram presentation in **Figure V.12**). Binding energies of atomic hydrogen on pure Pt and M(1 1 1) surfaces are also included for comparisons. Two other tables and graphs gathering same calculated binding energy information for (1 0 0) and (1 1 0) surfaces are provided in **Figure SI-V.4** and **Figure SI-V.5**.

Table V.1 Hydrogen binding energy comparison between single-atom M sites anchoring in Pt-host surfaces Pt(1 1 1) and neighboring Pt-site of M with M free from hydrogen. Pure Pt-host surfaces are added as reference. Unfavorable (endothermic) binding energies are noted as red color to facilitate the comparisons.

		Pt(1 1 1)	
Pure Pt-host		-0.70	
Single-atom M		M/Pt(1 1 1)	
		H on M	H on Pt
Coinage group	Cu	0.50	-0.69
	Ag	0.81	-0.68
	Au	0.15	-0.66
		H on M	H on Pt
Nickel group	Ni	-0.07	-0.70
	Pd	-0.16	-0.68
		H on M	H on Pt
Cobalt group	Co	0.12	-0.17
	Rh	-0.43	-0.77
	Ir	-0.79	-0.68

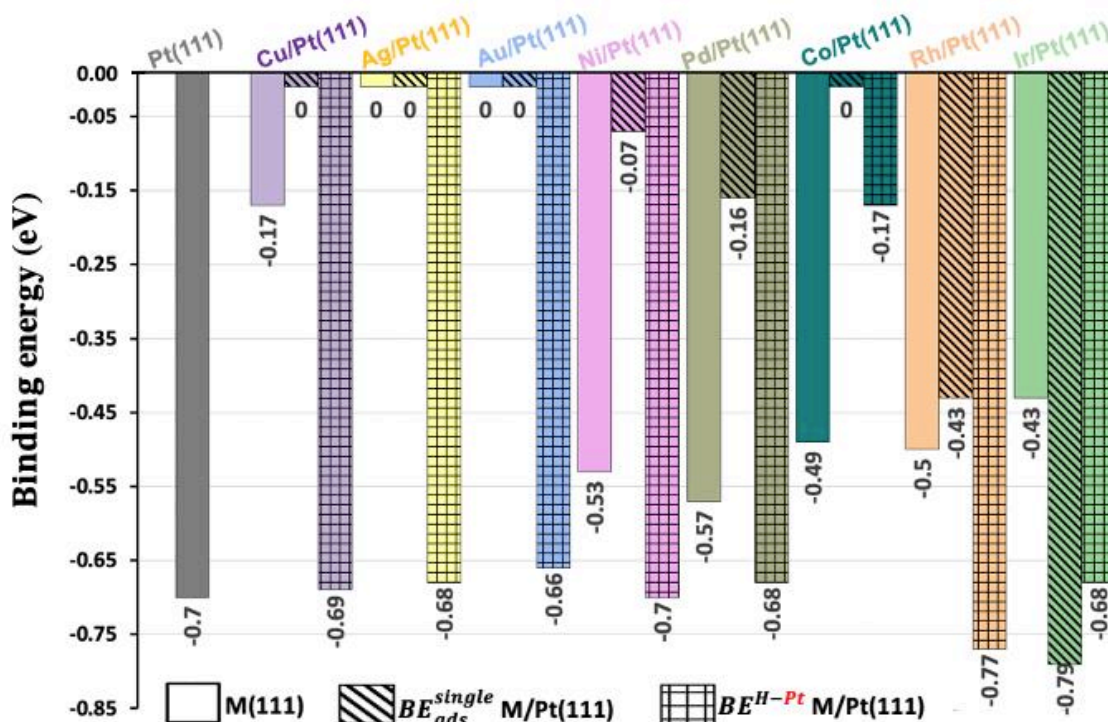


Figure V.12 | Hydrogen binding energy on single-atom M anchored in Pt-host surfaces Pt(1 1 1) (BE_{ads}^{single} , histograms filled with diagonal lines) and on the neighboring Pt-site of M (with M free of hydrogen) (BE^{H-Pt} , histograms filled in cubic-grills). The binding energy of hydrogen atom on Pure Pt(1 1 1) and M(1 1 1) surfaces are added for comparison. Unfavorable (endothermic) binding energy values are fixed at 0 eV.

The results reveal that among all the considered systems, only in the case of Ir/Pt(1 1 1) hydrogen shows a stronger affinity to the single atom than to the host surface. Thus, the hydrogen is found to strongly bound to single-atom Ir with $BE_{ads}^{single} = -0.79$ eV while the binding energy on neighboring Pt atoms is predicted to be of 0.11 eV lower. Surprisingly, except for the case of Co, the binding energies of hydrogen interacting with host Pt atoms (neighbors of anchored M-single atom) are found to not be affected by the presence of M-single atom neighbors. Compared to Pt(1 1 1) surface (-0.7 eV), the binding energies on M-single atoms vary by +0.07 and -0.02 eV. For the case of Rh/Pt(1 1 1), the hydrogen affinity to the Pt is more pronounced ($BE = 0.77$ eV). Despite the strong affinity of hydrogen to Ir and as it was

discussed in the previous section, this latter still prefers to be in the bulk and does not segregate to the surface. For the case of M single-atoms from the coinage group (Cu, Ag and Au), they all show unfavorable binding energies (positive values or in case of Au/Pt(1 1 0), negligibly negative value (-0.01 eV)). For Cu/ Pt(1 1 1) surface, the bulk-segregation trends of single-atom Cu under vacuum is in line with its calculated endothermic hydrogen binding energy. Nevertheless, with endothermic binding to hydrogen, Au and Ag single atoms still present strong surface-segregation preference in Pt surfaces (**Figure V.9**). This confirms the previously discussed “counterintuitive” image and shows again, that the simple consideration of the affinity of one of the alloy components to the adsorbed gas phase cannot allow predicting the surface segregation or surface enrichment. The segregation of alloy components under reactive conditions will depend on many interplaying factors as the interfacial surface energies, the cohesive energies, the atomic radiuses, the surface orientations, etc.

3.B.3 Section summary

To recap, for the studied M/Pt surface alloys, in which the M-single atoms are anchored in different Pt-host surfaces, it can be concluded that:

- (i) M/Pt with M from the cobalt group, i.e. (M= Co, Rh and Ir), cannot present stable M single-atoms in the surface. This is true whatever the Pt orientation surface and applied temperature and hydrogen pressure.
- (ii) Single atom Pd in Pt (1 0 0), Pt(1 1 0) surface and single atom Ni in Pt(1 1 0) are found to be stable at the surface at high-T and low-P window. With decreasing T and/or increasing P (corresponding to the increase of hydrogen coverage) single-atoms are predicted to segregate from the surface to the bulk.

(iii) Among all investigated metals, possible favorable surface segregation and stability on the Pt surface are found for Ag and Au. These single atoms may be stable in all Pt surface orientations at high temperature and/or low hydrogen pressure range. However, this surface-segregation preference may be weakened with decreasing T and/or increasing P.

4. Conclusion

In this chapter, using the environmental segregation model, the evolution of the segregation behavior of several Pt-based alloy systems under various temperatures (T: 200 -1200 K) and hydrogen gas pressures (P:1 - 10^5 Pa) were investigated. We focused on the two diluted limits of these alloyed systems, the Pt atom diluted in metallic host surfaces and metallic atoms diluted in Pt host surfaces.

We started by studying the Pt as a single-atom diluted in 8 selected transition metal (M) surfaces (M = Cu, Ag, Au, Ni, Pd, Co, Rh, Ir). Several of these systems anchoring and named as Pt single atom alloy (SAAs) catalysts have been found to exhibit superior catalytic activity. Three classes of SAAs could be distinguished: i) The Au and Ag surfaces, in which single-atom Pt exposed to hydrogen pressure could not be found because this latter will prefer to segregate into the bulk; ii) Copper and palladium supports, where the surface segregation of single-atom Pt could be optimum only for definite orientations (Cu(1 1 1) and Cu(1 1 0) for Pt/Cu and Pd(1 1 0) for Pt/Pd) and under specific hydrogen pressures and temperatures; iii) Co, Rh, Ir and Ni supports in which single-atom Pt could remain stable in the surface within the quasi-totality of the pressure and temperature ranges studied.

Then, we considered Pt as a host surface of M single-atoms (M = Cu, Ag, Au, Ni, Pd, Co, Rh, Ir) and we studied their segregation behaviors for the same range of temperature and hydrogen

pressure than previously. For these systems, only Ag and Au single atom Pt are found to segregate toward the surface of Pt under hydrogen. These results show how the segregation behavior in presence of reactive gas is a complex process happening in bimetallic alloys. The simplistic picture in which the response to adsorbates is that the more reactive alloy component (i.e., the one interacting strongly with the adsorbates) segregates to the surface, may induce erroneous interpretations. The reality is that the chemistry of diluted single atom Pt is completely different from what is known from the extended surfaces and from clusters and nanoparticle. Its stability in the surface is an interplay between different properties and depends either on its modified electronic structure within the host material, its geometric ensemble (surface orientation) and its affinity to the reactive gas.

Reference

1. Besenbacher, F.; Chorkendorff, I. I.; Clausen, B. S.; Hammer, B.; Molenbroek, A. M.; Norskov, J. K.; Stensgaard, I. I., Design of a Surface Alloy Catalyst for Steam Reforming. *Science* **1998**, *279*, 1913-1915.
2. Kyriakou, G.; Boucher, M. B.; Jewell, A. D.; Lewis, E. A.; Lawton, T. J.; Baber, A. E.; Tierney, H. L.; Flytzani-Stephanopoulos, M.; Sykes, E. C., Isolated Metal Atom Geometries as a Strategy for Selective Heterogeneous Hydrogenations. *Science* **2012**, *335*, 1209-1212.
3. Tao, F.; Grass, M. E.; Zhang, Y.; Butcher, D. R.; Renzas, J. R.; Liu, Z.; Chung, J. Y.; Mun, B. S.; Salmeron, M.; Somorjai, G. A., Reaction-Driven Restructuring of Rh-Pd and Pt-Pd Core-Shell Nanoparticles. *Science* **2008**, *322*, 932-934.
4. Mu, R. T.; Guo, X. G.; Fu, Q.; Bao, X. H., Oscillation of Surface Structure and Reactivity of PtNi Bimetallic Catalysts with Redox Treatments at Variable Temperatures. *The Journal of Physical Chemistry C* **2011**, *115*, 20590-20595.
5. Vendelbo, S. B., et al., Visualization of Oscillatory Behaviour of Pt Nanoparticles Catalysing CO Oxidation. *Nature Materials* **2014**, *13*, 884-890.
6. Ahmadi, M.; Cui, C.; Mistry, H.; Strasser, P.; Cuenya, B. R., Carbon Monoxide-Induced Stability and Atomic Segregation Phenomena in Shape-Selected Octahedral PtNi Nanoparticles. *ACS Nano* **2015**, *9*, 10686-10694.
7. Greeley, J.; Mavrikakis, M., Alloy Catalysts Designed from First Principles. *Nature Materials* **2004**, *3*, 810-815.
8. Andersson, K. J.; Calle-Vallejo, F.; Rossmeisl, J.; Chorkendorff, I., Adsorption-Driven Surface Segregation of the Less Reactive Alloy Component. *Journal of the American Chemical Society* **2009**, *131*, 2404-2407.
9. Meng, J.; Zhu, B. E.; Gao, Y., Surface Composition Evolution of Bimetallic Alloys under Reaction Conditions. *The Journal of Physical Chemistry C* **2019**, *123*, 28241-28247.
10. Wang, Q.; Zhu, B.; Tielens, F.; Tichit, D.; Guesmi, H., Mapping Surface Segregation of Single-Atom Pt Dispersed in M Surfaces (M = Cu, Ag, Au, Ni, Pd, Co, Rh and Ir) under Hydrogen Pressure at Various Temperatures. *Applied Surface Science* **2021**, *548*.
11. Kresse, G.; Hafner, J., Ab Initio Molecular Dynamics for Liquid Metals. *Physical Review B* **1993**, *47*, 558-561.
12. Blochl, P. E.; Jepsen, O.; Andersen, O. K., Improved Tetrahedron Method for Brillouin-Zone Integrations. *Physical Review B* **1994**, *49*, 16223-16233.
13. Chase, M. W.; Davies, C. A.; R., D. J.; Frurip, D. J.; McDonald, R. A.; Syverud, A. N., Nist-Janaf Thermochemical Tables. In <https://janaf.nist.gov/>, 1999.
14. Hannagan, R. T.; Giannakakis, G.; Flytzani-Stephanopoulos, M.; Sykes, E. C. H., Single-Atom Alloy Catalysis. *Chemical Reviews* **2020**, *120*, 12044-12088.
15. Lu, B. Z.; Liu, Q. M.; Chen, S. W., Electrocatalysis of Single-Atom Sites: Impacts of Atomic Coordination. *ACS Catalysis* **2020**, *10*, 7584-7618.
16. Zhang, H. T.; Fang, S. Y.; Hu, Y. H., Recent Advances in Single-Atom Catalysts for CO Oxidation. *Catalysis Reviews-Science and Engineering* **2020**, 1-42.
17. Daelman, N.; Capdevila-Cortada, M.; Lopez, N., Dynamic Charge and Oxidation State of Pt/CeO₂ Single-Atom Catalysts. *Nature Materials* **2019**, *18*, 1215-1221.
18. DeRita, L., et al., Structural Evolution of Atomically Dispersed Pt Catalysts Dictates Reactivity. *Nature Materials* **2019**, *18*, 746-751.
19. Du, J. F.; Meng, J.; Li, X. Y.; Zhu, B. E.; Gao, Y., Multiscale Atomistic Simulation of Metal Nanoparticles under Working Conditions. *Nanoscale Advances* **2019**, *1*, 2478-2484.

20. Tang, Y.; Asokan, C.; Xu, M.; Graham, G. W.; Pan, X.; Christopher, P.; Li, J.; Sautet, P., Rh Single Atoms on TiO₂ Dynamically Respond to Reaction Conditions by Adapting Their Site. *Nature Communications* **2019**, *10*, 4488.
21. Wang, Q.; Tichit, D.; Meunier, F.; Guesmi, H., Combined Drifts and DFT Study of CO Adsorption and Segregation Modes in Pt-Sn Nanoalloys. *The Journal of Physical Chemistry C* **2020**, *124*, 9979-9989.
22. Parkinson, G. S.; Novotny, Z.; Argentero, G.; Schmid, M.; Pavelec, J.; Kosak, R.; Blaha, P.; Diebold, U., Carbon Monoxide-Induced Adatom Sintering in a Pd-Fe₃O₄ Model Catalyst. *Nature Materials* **2013**, *12*, 724-728.
23. Liu, L. C.; Corma, A., Evolution of Isolated Atoms and Clusters in Catalysis. *Trends in Chemistry* **2020**, *2*, 383-400.
24. Dhifallah, M.; Dhoub, A.; Aldulaijan, S.; F, D. I. R.; Guesmi, H., First-Principles Study of Au-Cu Alloy Surface Changes Induced by Gas Adsorption of CO, No, or O₂. *The Journal of Chemical Physics* **2016**, *145*, 024701.
25. Juarez, F.; Soldano, G.; Santos, E.; Guesmi, H.; Tielens, F.; Mineva, T., Interaction of Hydrogen with Au Modified by Pd and Rh in View of Electrochemical Applications. *Computation* **2016**, *4*.
26. Oğuz, I. C.; Mineva, T.; Creuze, J.; Guesmi, H., Equilibrium Au-Pd(100) Surface Structures under CO Pressure: Energetic Stabilities and Phase Diagrams. *The Journal of Physical Chemistry C* **2018**, *122*, 18922-18932.
27. Liu, S.; Zhao, Z.-J.; Yang, C.; Zha, S.; Neyman, K. M.; Studt, F.; Gong, J., Adsorption Preference Determines Segregation Direction: A Shortcut to More Realistic Surface Models of Alloy Catalysts. *ACS Catalysis* **2019**, *9*, 5011-5018.
28. Rao, K. K.; Do, Q. K.; Pham, K.; Maiti, D.; Grabow, L. C., Extendable Machine Learning Model for the Stability of Single Atom Alloys. *Topics in Catalysis* **2020**, *63*, 728-741.
29. Tyson, W. R.; Miller, W. A., Surface Free-Energies of Solid Metals - Estimation from Liquid Surface-Tension Measurements. *Surface Science* **1977**, *62*, 267-276.
30. Tran, R.; Xu, Z.; Radhakrishnan, B.; Winston, D.; Sun, W.; Persson, K. A.; Ong, S. P., Surface Energies of Elemental Crystals. *Scientific Data* **2016**, *3*, 160080.
31. Lucci, F. R.; Liu, J.; Marcinkowski, M. D.; Yang, M.; Allard, L. F.; Flytzani-Stephanopoulos, M.; Sykes, E. C., Selective Hydrogenation of 1,3-Butadiene on Platinum-Copper Alloys at the Single-Atom Limit. *Nature Communications* **2015**, *6*, 8550.
32. Simonovis, J. P.; Hunt, A.; Senanayake, S. D.; Waluyo, I., Subtle and Reversible Interactions of Ambient Pressure H₂ with Pt/Cu(111) Single-Atom Alloy Surfaces. *Surface Science* **2019**, *679*, 207-213.
33. Liu, J.; Lucci, F. R.; Yang, M.; Lee, S.; Marcinkowski, M. D.; Therrien, A. J.; Williams, C. T.; Sykes, E. C.; Flytzani-Stephanopoulos, M., Tackling CO Poisoning with Single-Atom Alloy Catalysts. *Journal of the American Chemical Society* **2016**, *138*, 6396-6399.
34. Marcinkowski, M. D.; Liu, J.; Murphy, C. J.; Liriano, M. L.; Wasio, N. A.; Lucci, F. R.; Flytzani-Stephanopoulos, M.; Sykes, E. C. H., Selective Formic Acid Dehydrogenation on Pt-Cu Single-Atom Alloys. *ACS Catalysis* **2017**, *7*, 413-420.
35. Marcinkowski, M. D.; Darby, M. T.; Liu, J.; Wimble, J. M.; Lucci, F. R.; Lee, S.; Michaelides, A.; Flytzani-Stephanopoulos, M.; Stamatakis, M.; Sykes, E. C. H., Pt/Cu Single-Atom Alloys as Coke-Resistant Catalysts for Efficient C-H Activation. *Nature Chemistry* **2018**, *10*, 325-332.
36. Sun, G., et al., Breaking the Scaling Relationship Via Thermally Stable Pt/Cu Single Atom Alloys for Catalytic Dehydrogenation. *Nature Communications* **2018**, *9*, 4454.

37. Peng, Y., et al., Pt Single Atoms Embedded in the Surface of Ni Nanocrystals as Highly Active Catalysts for Selective Hydrogenation of Nitro Compounds. *Nano Letters* **2018**, *18*, 3785-3791.
38. Zhang, L., et al., Pt/Pd Single-Atom Alloys as Highly Active Electrochemical Catalysts and the Origin of Enhanced Activity. *ACS Catalysis* **2019**, *9*, 9350-9358.
39. Jiang, K.; Liu, B.; Luo, M.; Ning, S.; Peng, M.; Zhao, Y.; Lu, Y. R.; Chan, T. S.; De Groot, F. M. F.; Tan, Y., Single Platinum Atoms Embedded in Nanoporous Cobalt Selenide as Electrocatalyst for Accelerating Hydrogen Evolution Reaction. *Nature Communications* **2019**, *10*, 1743.
40. Shu, J.; Bongondo, B. E. W.; Grandjean, B. P. A.; Adnot, A.; Kaliaguine, S., Surface Segregation of Pd-Ag Membranes Upon Hydrogen Permeation. *Surface Science* **1993**, *291*, 129-138.
41. Christoffersen, E.; Stoltze, P.; Nørskov, J. K., Monte Carlo Simulations of Adsorption-Induced Segregation. *Surface Science* **2002**, *505*, 200-214.
42. González, S.; Neyman, K. M.; Shaikhutdinov, S.; Freund, H.-J.; Illas, F., On the Promoting Role of Ag in Selective Hydrogenation Reactions over Pd–Ag Bimetallic Catalysts: A Theoretical Study. *The Journal of Physical Chemistry C* **2007**, *111*, 6852-6856.
43. Guesmi, H., Theoretical Insights on the Effect of Reactive Gas on the Chemical Ordering of Gold-Based Alloys. *Gold Bulletin* **2013**, *46*, 213-219.
44. Zhu, B.; Creuze, J.; Mottet, C.; Legrand, B.; Guesmi, H., CO Adsorption-Induced Surface Segregation and Formation of Pd Chains on AuPd(100) Alloy: Density Functional Theory Based Ising Model and Monte Carlo Simulations. *The Journal of Physical Chemistry C* **2016**, *120*, 350-359.
45. Jones, L. C.; Buras, Z.; Gordon, M. J., Partial Hydrogenation of C₂H₂ on Ag-Doped Pt Nanoparticles. *The Journal of Physical Chemistry C* **2012**, *116*, 12982-12988.
46. Liu, C. W.; Wei, Y. C.; Wang, K. W., Promotion of Ceria-Modified Pt-Au/C Cathode Catalysts for Oxygen Reduction Reaction by H₂-Induced Surface Segregation. *Chemical Communications* **2010**, *46*, 2483-2485.
47. Kittel, C.; McEuen, P.; John, W.; Sons, *Introduction to Solid State Physics*, 2015.
48. Sansa, M.; Dhouib, A.; Guesmi, H., Density Functional Theory Study of CO-Induced Segregation in Gold-Based Alloys. *The Journal of Chemical Physics* **2014**, *141*, 064709.
49. Gould, A. L.; Heard, C. J.; Logsdail, A. J.; Catlow, C. R., Segregation Effects on the Properties of (AuAg)₁(4)(7). *Physical Chemistry Chemical Physics* **2014**, *16*, 21049-21061.
50. Williams, F. L.; Nelson, G. C., Surface Composition of Pt/Rh Alloys. *Applications of Surface Science* **1979**, *3*, 409-415.
51. Van Delft, F. C. M. J. M.; Van Langeveld, A. D.; Nieuwenhuys, B. E., The Temperature Dependence of the Surface Composition of Pt–Rh Alloys. *Surface Science* **1987**, *189-190*, 1129-1134.

Summary and General Conclusions

This thesis manuscript reports a part of my research work that I performed during the last three years. The focus is the description and the prediction of the surface active sites of TMC formed by NPs evolving under reactive conditions. Indeed, thanks to the experimental developments of characterization and observation methods we know that many NP catalysts undergo drastic morphological and symmetry transformations during reactions. These structural changes may affect their catalytic properties (activity and selectivity) and their lifetime. However, in spite of the great progress of these experimental techniques, the identification of the active working sites at the atomic-level and the understanding of the elementary mechanisms occurring on these sites are still missing for many catalytic systems. Nowadays, thanks to the powerful development of computational resources, theoretical methods, and more particularly DFT, stands as the key technic for elucidating the surface state of materials and their physico-chemical properties. However, DFT is a zero-temperature method where investigations are generally performed on “static” crystal or surface models with minimum number of molecular adsorbates. By consequence, although important for a general understanding, this approach alone cannot accurately predict the catalytic systems at working pressure and temperature.

During my thesis, I tried to apply theoretical approaches that go beyond the 0 K temperature and very low pressure. The choice was always dictated by the targeted properties and an interplay between accuracy and limitation of the method has to be taken into account. Thus, firstly, I studied the morphological changes of Pt and Au NP catalysts under varied hydrogen pressure and temperature and I performed two different approaches. For Pt-NPs larger than 5 nm, MSR model was applied, by combining DFT with thermodynamics to calculate the evolution of interfacial energy as a function of T and P . Then geometric construction of the Pt-NPs was obtained using Wulff construction. I learned this method thanks to a visiting program

Summary and General Conclusions

in Shanghai (Cai Yuanpei) that allowed me to spend several weeks in the group of Gao and Zhu who developed this model. The results of MSR provide equilibrium Pt-NP shapes for a large range of temperature and hydrogen pressure and show shape evolutions that concord well with the experimentally observed ones (Paper under preparation). Then, to study the dynamic changes of small-sized Pt-NPs, we performed AIMD simulations of TOh Pt-NP of 201 atoms (~1.8 nm) covered by hydrogen and we followed the configurational trajectory of the system at $T = 500$ K for simulation time up to 30-ps. The results show that the chemisorbed hydrogen has no effect on the morphology of small Pt-NPs. Surprisingly, contrasting results were found for Au, which is known to have endothermic interactions with hydrogen. Indeed, our AIMD study, with simulation time up to 60-ps, of TOh Au-NP of 201 atoms covered by atomic hydrogen, reveals that Au-NP undergoes drastic morphological and symmetry changes. The AIMD results at 300 and 500 K show that hydrogenated gold surface atoms stabilize in several ordered “Au-H-Au” crowned lines sliding around a highly distorted core (Paper under review for publication in journal “Small”). This revealed NP structure is far from the conventional model Au-NP catalyst often used in heterogeneous catalysis (well faceted NPs with ridged structure) to study the reactivity as in hydrogenation catalytic reactions. Furthermore, these results confirm ETEM observations performed by our collaborators from the laboratory MPQ of the University Paris Diderot and open the way for deep investigations of the reactivity of these “more realistic” surface active sites to accurately understand the reaction mechanisms occurring over hydrogenated gold nanocatalysts.

Secondly, I investigated the chemical ordering changes occurring in Pt alloy catalysts under hydrogen media by calculating the evolution of environmental segregation energies as a function of temperature and pressure. I focused on the two diluted states of selected alloyed systems, the Pt as a single-atom diluted in 8 selected transition metal (M) surfaces ($M = \text{Cu}, \text{Ag}, \text{Au}, \text{Ni}, \text{Pd}, \text{Co}, \text{Rh}, \text{Ir}$) and Pt as a host surface of M single-atoms. These results (published

Summary and General Conclusions

in the journal of App. Surf. Sci.) showed complex segregation behavior in presence of reactive gas where the simplistic picture in which the response to adsorbates is that the more reactive alloy component (i.e., the one interacting strongly with the adsorbates) segregates to the surface, may induce erroneous interpretations. The reality is that the chemistry of diluted single-atom Pt is completely different from what is known from the extended surfaces and from clusters and nanoparticles modeled under vacuum.

Finally, besides this detailed work in collaboration with the groups of Shanghai and Paris, I also get the chance to collaborate with other scientists from France and from Europe working on alloy Pt systems. With Dr. Frederic Meunier, expert of the *in situ* IR spectroscopy from Lyon, I performed DFT calculations of PtSn NPs to study the segregation signature of Sn in presence of CO (results published in J. Phys. Chem C). In addition, I spent two weeks in Brussel in the lab of Pr. Frederik Tielens, where I studied the interaction of NO and the dissociation reaction on Pt alloy NPs (Paper submitted to ACS catal.). The results detailed in the published articles are attached in the end of this manuscript.

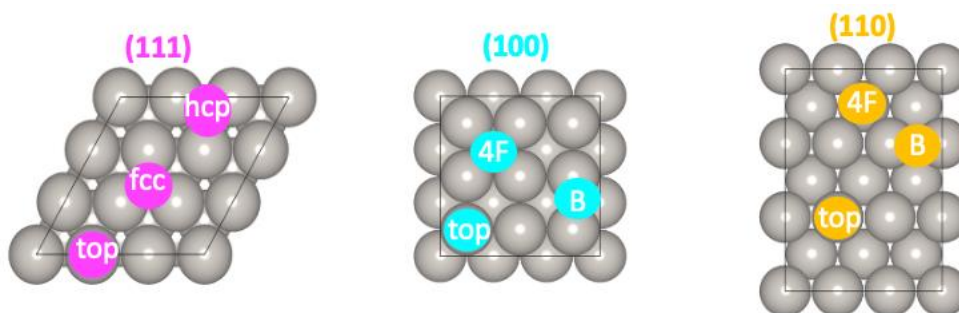
Supporting Information

SI-Chapter III. Modeling Pt nanoparticles under hydrogen media

SI-III.1 Adsorption energies of hydrogen on different adsorption sites of Pt surfaces

The **Table SI-III.1** presents the DFT calculated hydrogen adsorption energies on different possible adsorption sites denoted as: (i) “top”, when one atomic hydrogen is adsorbed on the Pt surface, (ii) “B”, when H is bridging between two surface Pt atoms, (iii) “4F”, when H is adsorbed on the four-fold hollow site of Pt surface, (iv) “fcc”, when H is adsorbed on the four-fold hollow site of Pt surface, (v) “hcp”, when H is on the hcp hollow site of Pt surface. The most stable adsorption sites (in red) of each Pt surface orientation are selected to couple with the MSR model (see section 2 in **Chapter 3** for reference).

Table SI-III.1I. Adsorption energies calculated on different sites of Pt (111), (100) and (110) surfaces. The most stable adsorption site of respective Pt facets are marked in red.



Pt surface	top	B	4F	fcc	hcp
(111)	-0.68	-	-	-0.70	-0.65
(100)	-0.63	-0.84	-0.59	-	-
(110)	-0.73	-0.76	-	-	-

SI-III.2 Fitted entropy profile of gas-phase hydrogen (H₂) as a function of temperature.

In the MSR model, to describe the hydrogen adsorption behaviors on the NP surface, the Fowler-Guggenheim adsorption isotherm is applied (see section 5 in Chapter II for reference), wherein the temperature-dependent hydrogen gas entropy at 1 atmosphere pressure are extracted from the NIST-JANAF Thermochemical Tables database [1] and fitted in **Figure SI-III.1** in the temperature range between 0 and 1200 K.

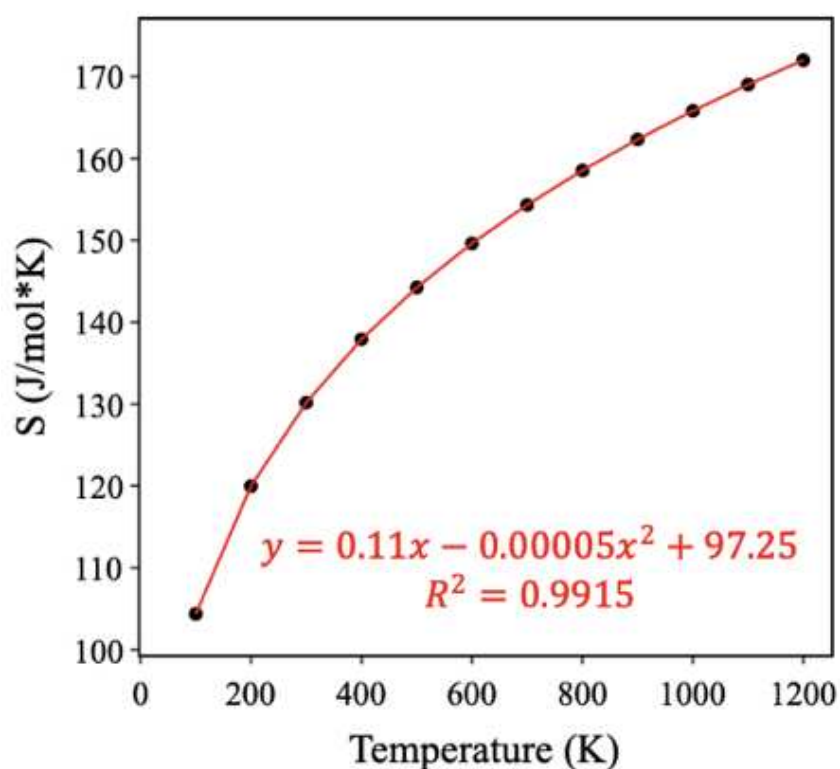


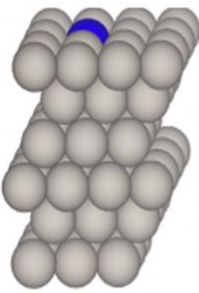
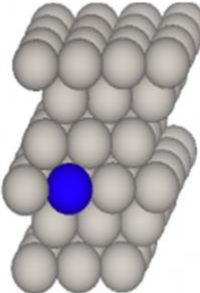
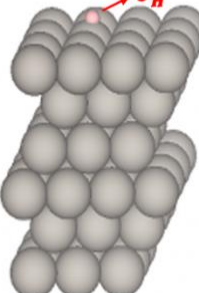
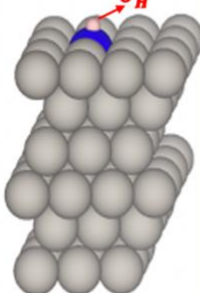
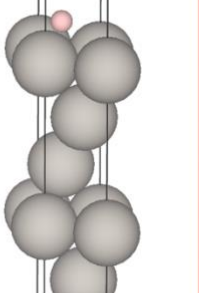



Figure SI-III.1 Fitted entropy of gas-phase hydrogen (H₂) as a function of temperature. The fitted data is obtained from the NIST-JANAF Thermochemical Tables database [1].

SI-Chapter V. Modeling Pt based alloys under hydrogen media: from single atom to host surface

SI-V.1 List of all DFT calculated data applied in environmental surface segregation model

The **Table SI-V.1** contains all the DFT calculated parameters needed to predict the environmental surface segregation of single-atom diluted in host surface. The E_{seg} is the segregation energy (energy difference between E_{surf}^{single} and E_{bulk}^{single}) of the single-atom in vacuum; BE^{single} (E_{bulk}^{single}) is the binding energy with one adsorbed hydrogen atom on the single-atom (host atom site) site, respectively; zw is the lateral interaction (w) where z is the number of nearest neighbors of an adsorption site on the surface: 6 for (1 1 1), 4 for (1 0 0) and 2 for (1 1 0).

Table SI-V.1. DFT calculated segregation energies under vacuum E_{seg} , binding energies of one adsorbed hydrogen on the single-atom BE^{dilute} , and on the pure host-surface BE^{host} , and the lateral interaction w of H on the host-surface.

3×3 Unit Cells				1×1 Unit Cells
E_{surf}^{single}	E_{bulk}^{single}	BE^{host}	BE^{single}	$E_{ads c(1\times1)}$
				
 Single-atom	 Host (M) atom	 Adsorbates (H) atom		
Single-atom/Host	$E_{seg}(eV)$	$BE^{single}(eV)$	$BE^{host}(eV)$	$zw(meV)$

Single-atom Pt dilute in host-M surfaces

Supporting Information

Pt/Cu(111)	-0.06	-0.26	-0.17	-62
Pt/Ag(111)	0.27	-0.28	0	0
Pt/Au(111)	0.29	-0.34	0	0
Pt/Ni(111)	-0.45	-0.30	-0.53	-6.4
Pt/Pd(111)	0.06	-0.49	-0.57	-110
Pt/Co(0001)	-0.63	-0.19	-0.49	0
Pt/Rh(111)	-0.32	-0.32	-0.50	-67
Pt/Ir(111)	-0.53	-0.32	-0.43	-89
Pt/Cu(100)	0.13	-0.24	-0.19	-230
Pt/Ag(100)	0.42	-0.30	0	0
Pt/Au(100)	0.42	-0.33	0	0
Pt/Ni(100)	-0.31	-0.33	-0.50	0
Pt/Pd(100)	0.16	-0.47	-0.48	-3.6
Pt/Rh(100)	-0.32	-0.38	-0.52	-47
Pt/Ir(100)	-0.73	-0.33	-0.66	0
Pt/Cu(110)	0.16	-0.31	-0.17	-47
Pt/Ag(110)	0.47	-0.35	0	0
Pt/Au(110)	0.46	-0.39	0	0
Pt/Ni(110)	-0.35	-0.30	-0.35	0
Pt/Pd(110)	0.24	-0.59	-0.45	-68

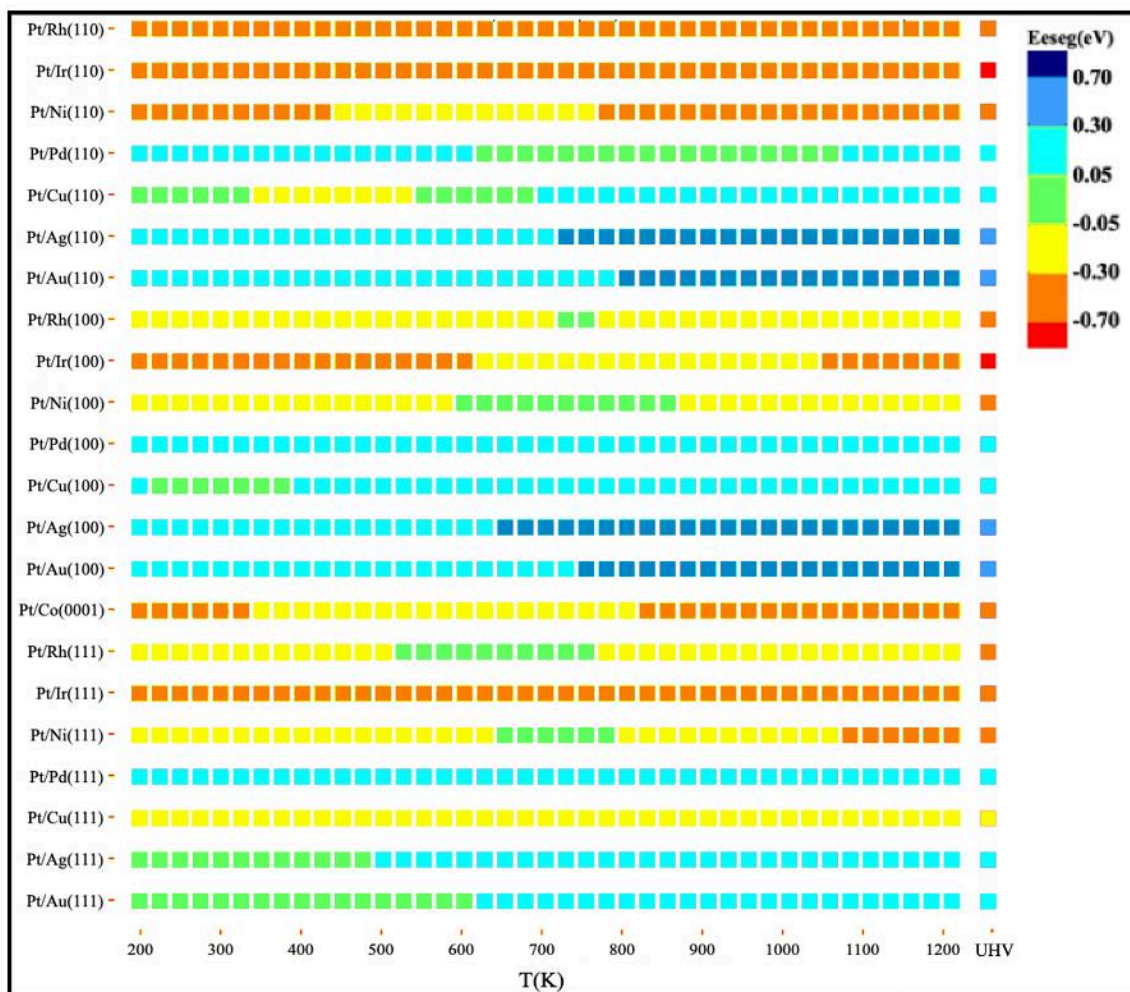
Pt/Rh(110)	-0.32	-0.46	-0.42	0
Pt/Ir(110)	-0.76	-0.43	-0.55	0
Single-atom M dilute in host-Pt surfaces				
Cu/Pt(111)	0.42	0	-0.70	-130
Ag/Pt(111)	-0.33	0	-0.70	-130
Au/Pt(111)	-0.56	0	-0.70	-130
Ni/Pt(111)	0.53	-0.070	-0.70	-130
Pd/Pt(111)	0.049	-0.16	-0.70	-130
Co/Pt(111)	0.63	0	-0.70	-130
Rh/Pt(111)	0.43	-0.43	-0.70	-130
Ir/Pt(111)	0.47	-0.79	-0.70	-130
Cu/Pt(100)	0.21	0	-0.84	-63
Ag/Pt(100)	-0.66	0	-0.84	-63
Au/Pt(100)	-0.74	0	-0.84	-63
Ni/Pt(100)	0.35	-0.049	-0.84	-63
Pd/Pt(100)	-0.12	-0.078	-0.84	-63
Co/Pt(100)	1.011	-0.49	-0.84	-63
Rh/Pt(100)	0.36	-0.37	-0.84	-63
Ir/Pt(100)	0.51	-0.81	-0.84	-63
Cu/Pt(110)	-0.24	0	-0.76	-5.1

Ag/Pt(110)	-0.89	0	-0.76	-5.1
Au/Pt(110)	-0.79	-0.013	-0.76	-5.1
Ni/Pt(110)	-0.060	-0.021	-0.76	-5.1
Pd/Pt(110)	-0.20	-0.13	-0.76	-5.1
Co/Pt(110)	0.058	0	-0.76	-5.1
Rh/Pt(110)	0.26	-0.38	-0.76	-5.1
Ir/Pt(110)	0.51	-0.83	-0.76	-5.1

SI-V.2 Scatters graphs of the segregation trend under fixed pressures (10^4 Pa and 100 Pa) for dilute-Pt/M bimetallic alloys

The **Figure SI-V.1** presents the evolution of predicted environmental segregation energy (E_{eseg}) of single-atom Pt in different host M surfaces as a function of temperature under hydrogen pressures 10^4 Pa and 100 Pa. Their corresponding segregation energies under vacuum E_{eeg} are also included for comparison. The calculated E_{eseg} values are color-coded to represent different degrees of surface- or bulk-segregation trends of single-atom Pt (see section 2 in **Chapter 5** for reference).

(A)

 $P = 10^4 \text{ Pa}$ 

(B)

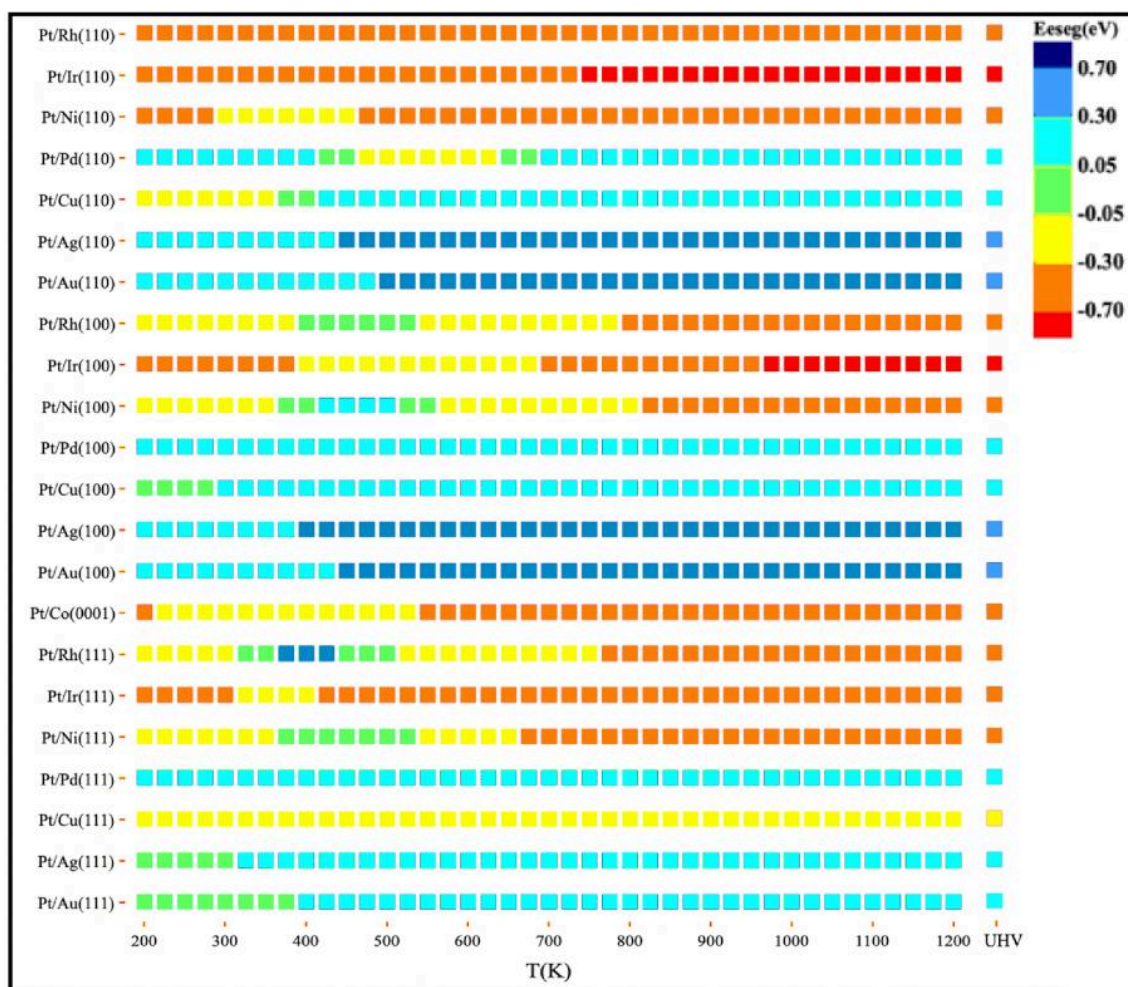
P = 100 Pa

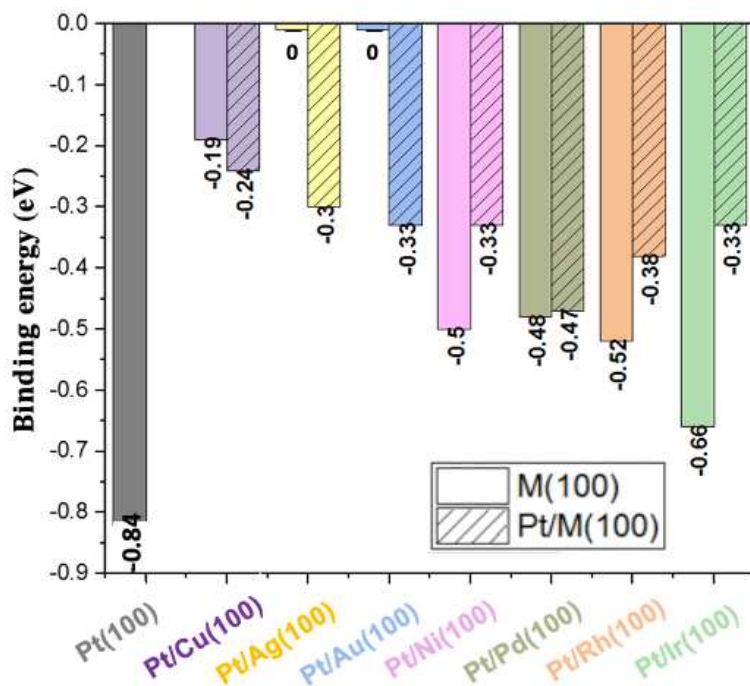
Figure SI-V.1 Environmental segregation trends of dilute-Pt in host-M surfaces as function of temperature at given hydrogen pressure. (A) at 10^4 Pa (B) at 100 Pa. The calculated environmental segregation energy values are color-coded and compared with their corresponding segregation energy under vacuum (UHV).

SI-V.3 Binding energies of hydrogen on pure host metallic (1 0 0) and (1 1 0) surfaces (without single-atom Pt) and on single-atom Pt anchored in these surfaces (dilute-Pt/M bimetallic alloys).

The **Figure SI-V.2** contains the DFT calculated binding energies of hydrogen on pure host metallic (1 1 0) and (1 0 0) surfaces (free from single-atom sites) and on single-atom Pt

anchored of these surfaces. The binding energy of hydrogen atom on pure Pt(1 1 0) and Pt(1 0 0) surfaces are added for valuable comparison.

(A)



(B)

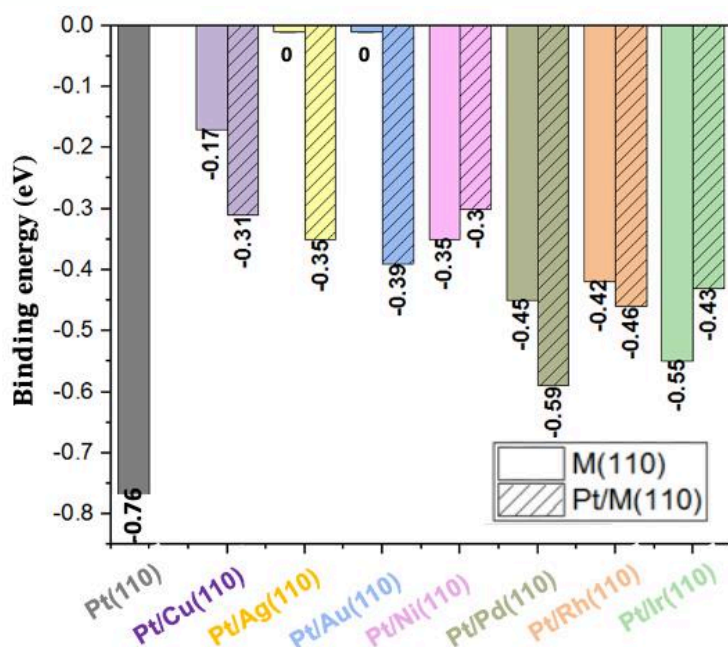


Figure SI-V.2 Binding energy comparison between pure M host-surfaces BE^{host} and single-atom Pt dilutes in M host-surfaces BE^{single} . (A) on M(1 0 0) orientation. (B) on M(1 1 0) orientation. For comparison, the binding energies of hydrogen on pure Pt (1 0 0) and Pt (1 1 0) surfaces are indicated.

SI-V.4 Environmental segregation and hydrogen coverage evolution profile as function of hydrogen pressure at 300 K (dilute-Pt/Cu(1 1 0) bimetallic alloys).

The **Figure SI-V.3** shows the evolutions of E_{eseg} of single-Pt in Cu(1 1 0) as a function of hydrogen pressure with temperature fixed to 300 K. This figure helps in understanding the non-monotonic E_{eseg} evolution behavior of Pt in Cu(1 1 0) due to the competition between the hydrogen coverage on host and on Pt-single sites (see section 3 in **Chapter 5** for reference).

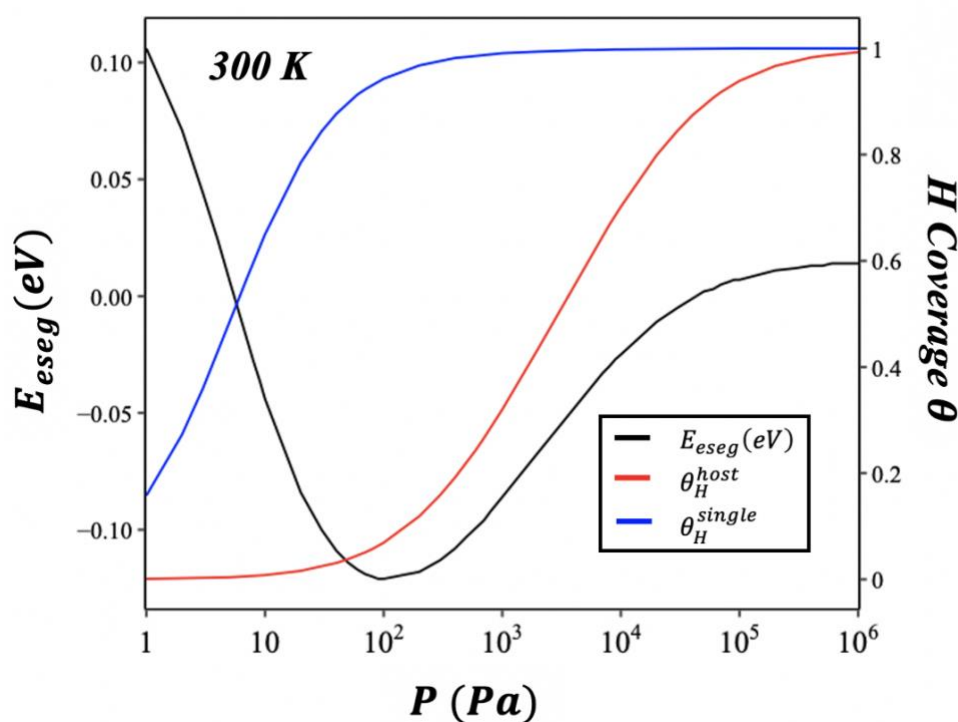


Figure SI-V.3 Environmental segregation E_{eseg} and hydrogen coverage profiles as function of hydrogen pressure at 300 K (dilute-Pt/Cu(1 1 0) bimetallic alloy). Environmental segregation energy of Pt (black line), hydrogen coverage on Cu host site (red line), hydrogen coverage on single-Pt site (blue line).

SI-V.5 *d*-band center analysis for dilute-Pt/M (1 1 1) bimetallic alloys.

Table SI-V.2. Calculated *d*-band centers from Local Density of States of single-atom Pt and neighboring atom from the host surface for all considered (1 1 1) surfaces. The *d*-band center of Pt from Pt(1 1 1) surface is indicated for comparison.

dilute-Pt/M(111) bimetallic alloys (SAAs)	<i>d</i> -band center (eV)
5d_Pt in {Pt(111)}	-1.838
5d_Pt in {Cu(111)}	-1.967
3d_Cu in {Cu(111)}	-2.275
5d_Pt in {Ag(111)}	-1.794
4d_Ag in {Ag(111)}	-3.801
5d_Pt in {Au(111)}	-1.847
5d_Au in {Au(111)}	-3.165
5d_Pt in {Ni(111)}	-2.413
3d_Ni in {Ni(111)}	-1.439
5d_Pt in {Pd(111)}	-1.962
4d_Pd in {Pd(111)}	-1.497
5d_Pt in {Co(0001)}	-2.842
3d_Co in {Co(0001)}	-2.094
5d_Pt in {Rh(111)}	-2.580
4d_Rh in {Rh(111)}	-1.595
5d_Pt in {Ir(111)}	-2.738
5d_Ir in {Ir(111)}	-2.113

SI-V.6 *d*-band center analysis for dilute-M/Pt(1 1 1) bimetallic alloys.

Table SI-V.3. Calculated *d*-band centers from Local Density of States of single-atom M and neighboring Pt-atom for all considered M/Pt(111) surfaces. The *d*-band center of Pt from Pt(111) surface is indicated for comparison.

dilute-M/Pt(111) bimetallic alloys	<i>d</i> -band center (eV)
5d_Pt in {Pt(111)}	-1.838
5d_Pt in {Cu/Pt(111)}	-1.698
3d_Cu in {Cu/Pt(111)}	-2.394
5d_Pt in {Ag/Pt(111)}	-1.709
4d_Ag in {Ag/Pt(111)}	-3.939
5d_Pt in {Au/Pt(111)}	-1.714
5d_Au in {Au/Pt(111)}	-3.782
5d_Pt in {Ni/Pt(111)}	-1.746
3d_Ni in {Ni/Pt(111)}	-1.003
5d_Pt in {Pd/Pt(111)}	-1.773
4d_Pd in {Pd/Pt(111)}	-2.059
5d_Pt in {Co/Pt(111)}	-1.775
3d_Co in {Co/Pt(111)}	-1.943
5d_Pt in {Rh/Pt(111)}	-1.762
4d_Rh in {Rh/Pt(111)}	-1.295
5d_Pt in {Ir/Pt(111)}	-1.729
5d_Ir in {Ir/Pt(111)}	-1.431

SI-V.7 Hydrogen binding energy comparisons for dilute-M/Pt(1 0 0) and dilute-M/Pt(1 1 0) bimetallic alloys.

In Table SI-V.4 and Table SI-V.5 are depicted the binding energies of hydrogen interacting with single-M atoms anchored in Pt(1 0 0) and Pt(1 1 0) host surfaces, respectively.

Additionally, to evaluate how single-M atoms effect their neighboring Pt atoms, the hydrogen binding energies on the neighboring Pt (with M free from hydrogen) are also calculated in **Figure SI-V.4** and **Figure SI-V.5**). Binding energies of atomic hydrogen on pure Pt and M(1 0 0)/M(1 1 0) surfaces are also included for comparisons.

The analysis of the two other surface orientations of Pt (1 0 0) and (1 1 0) shows that the “H-Pt” binding energies are all weakened (around 0.2 eV) when single-atoms M diluted into Pt(1 0 0) surface, whereas the hydrogen binding affinity to the Pt are all more or less increased when M diluted in Pt(1 1 0) surfaces, with one exception concerning Ir, for which the H-Pt binding is slightly reduced (only 0.05 eV). Based on the above comparisons, despite different effects of single-atoms M on the “H-Pt” bindings, they all (except Co) remain in a close energetic level to its “H-Pt” binding on the pure host Pt surfaces.

Table SI-V.4 Hydrogen binding energy comparison between single-atom M sites that anchoring in Pt-host surfaces Pt(1 0 0) and neighboring Pt-site of M with M free from hydrogen. Pure Pt-host surfaces are added as reference. Unfavorable (endothermic) binding energies are noted as red color to facilitate the comparisons.

		Pt(1 0 0)	
Pure Pt-host		-0.84	
Single-atom M		M/Pt(1 0 0)	
		H on M	H on Pt
Coinage group	Cu	0.36	-0.65
	Ag	0.70	-0.65
	Au	0.01	-0.62
		H on M	H on Pt
Nickel group	Ni	-0.05	-0.63
	Pd	-0.08	-0.64
		H on M	H on Pt
Cobalt group	Co	-0.49	-0.63
	Rh	-0.37	-0.72
	Ir	-0.81	-0.64

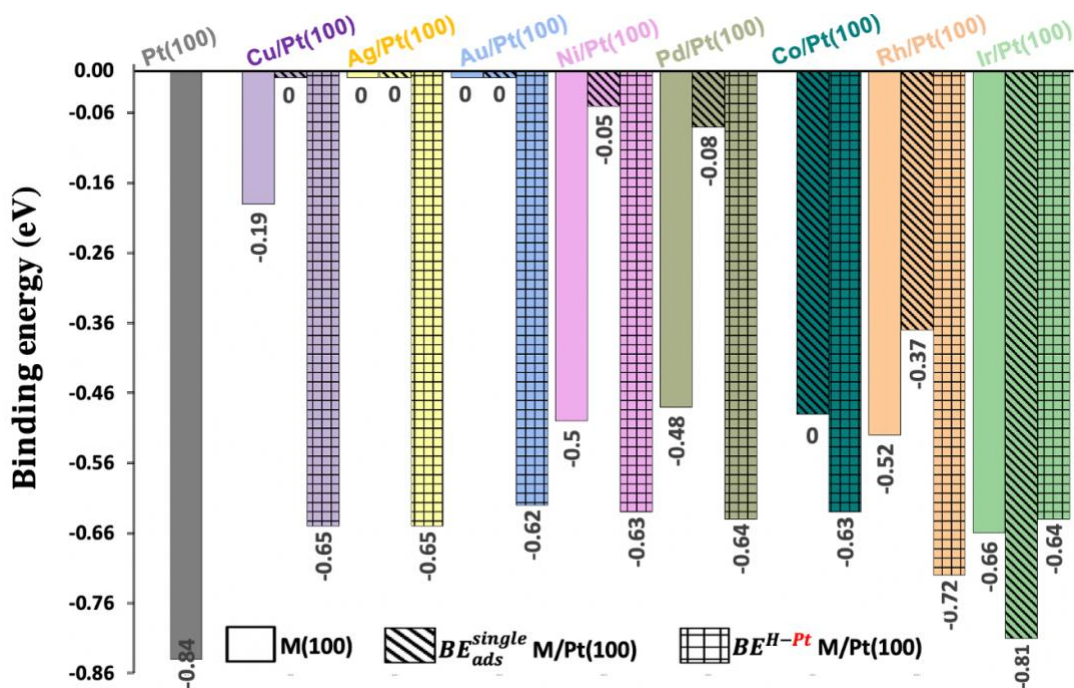


Figure SI-V.4 Hydrogen binding energy on single-atom M anchored in Pt-host surfaces Pt(1 0 0) (BE_{ads}^{single} , histograms filled with diagonal lines) and on the neighboring Pt-site of M (with M free of hydrogen) (BE^{H-Pt} , histograms filled in cubic-grills). The binding energy of hydrogen atom on Pure Pt(1 0 0) and M(1 0 0) surfaces are added for comparison. Unfavorable (endothermic) binding energy values are fixed at 0 eV.

Table SI-V.5 Hydrogen binding energy comparison between single-atom M sites that anchoring in Pt-host surfaces Pt(1 1 0) and neighboring Pt-site of M with M free from hydrogen. Pure Pt-host surfaces are added as reference. Unfavorable (endothermic) binding energies are noted as red color to facilitate the comparisons.

		Pt(1 1 0)	
Pure Pt-host		-0.76	
Single-atom M		M/Pt(1 1 0)	
		H on M	H on Pt
Coinage group	Cu	0.41	-0.80
	Ag	0.79	-0.82
	Au	-0.01	-0.79
		H on M	H on Pt
Nickel group	Ni	-0.02	-0.78
	Pd	-0.13	-0.78
		H on M	H on Pt
Cobalt group	Co	0.14	-0.77
	Rh	-0.38	-0.83
	Ir	-0.83	-0.71

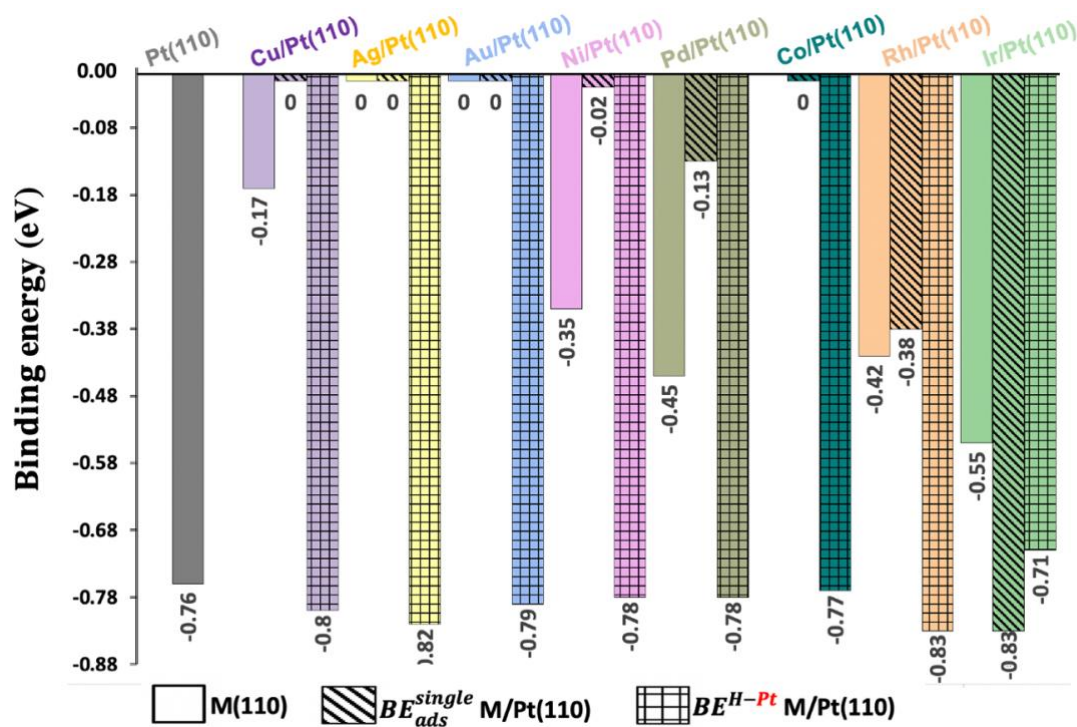


Figure SI-V.5 Hydrogen binding energy on single-atom M anchored in Pt-host surfaces Pt(1 1 0) (BE_{ads}^{single} , histograms filled with diagonal lines) and on the neighboring Pt-site of M (with M free of hydrogen) (BE^{H-Pt} , histograms filled in cubic-grills). The binding energy of hydrogen atom on Pure Pt(1 1 0) and M(1 1 0) surfaces are added for comparison. Unfavorable (endothermic) binding energy values are fixed at 0 eV.

Reference

1. Chase, M. W.; Davies, C. A.; R., D. J.; Frurip, D. J.; McDonald, R. A.; Syverud, A. N., Nist-Janaf Thermochemical Tables. In <https://janaf.nist.gov/>, 1999.

List of Publication

1. **Q. WANG**, B. Zhu, F. Tielens, D. Tichit, H. Guesmi, Mapping Surface Segregation of Single-Atom Pt dispersed in M Surfaces (M = Cu, Ag, Au, Ni, Pd, Co, Rh and Ir) under Hydrogen Pressure at Various Temperatures, *Applied Surface Science*, 548, 149217 (2021)
2. A. Nassereddine, **Q. WANG** (co-first authorship), D. Loffreda, C. Ricolleau, D. Alloyeau, C. Louis, L. Delannoy, J. Nelayah and H. Guesmi, Revealing Size Dependent Structural Transitions in Supported Gold Nanoparticles in Hydrogen at Atmospheric Pressure, *Small*, (under review).
3. **Q. WANG**, B. Zhu, F. Tielens, D. Tichit and H. Guesmi, Screening the Dynamics of Shape and Surface Composition Evolution of Pt-Based Nanoalloys Under Hydrogen Pressure, (under preparation)

Paper not included in this thesis:

1. **Q. WANG**, D. Tichit, F. Meunier, H. Guesmi, Combined DRIFTS and DFT Study of CO Adsorption and Segregation Modes in Pt-Sn Nanoalloys, *The Journal of Physical Chemistry C*, 124 (18), 9979-9989 (2020)
2. J. Vekeman, **Q. WANG**, X. Deraet, D. Bazin, F. De Proft, H. Guesmi and F. Tielens, Synergistic Catalytic Effects in the Activity of Nano-Transition-Metal Clusters P12M (M = Ir, Ru or Rh) for DeNO_x Catalysts in Vacuum and an Amorphous Silica Pore, *ACS Catalysis*, (submitted).

Abstract

Under working conditions, catalysts formed by transition metal nanoparticles (NPs) undergo dynamic changes in response to the reactive gas environment. These structural, chemical ordering and/or morphological transformations may affect their catalytic properties. This thesis focuses on the development of multi-scaled approaches based on density functional theory calculations (DFT). Two issues were addressed: (i) the morphological changes of Pt- and Au-NPs under varied hydrogen pressure (P) and temperature (T) and (ii) the chemical ordering changes occurring in Pt-based alloys under hydrogen pressure. The results reveal, in the atomic scale, the complexity of the changes induced by the adsorbates.

Key words

Effect of the gas environment, transition metal, nanoparticles, catalysts, gold, platinum, DFT, thermodynamics, ab-initio molecular dynamics, interface energy, segregation energy.

Résumé

Dans les conditions de travail, les catalyseurs formés par des nanoparticules (NP) de métaux de transition, subissent des changements en réponse au gaz réactif environnant. Ces transformations de structure, d'ordre chimique et/ou de forme, affecteraient leurs propriétés catalytiques. Les travaux de cette thèse se consacrent sur le développement d'approches multi-échelles basées sur des calculs issus de la théorie de la fonctionnelle de la densité (DFT). Deux problématiques sont abordées : (i) les changements morphologiques et structuraux subis par les NP de platine et d'or sous température (T) et pression d'hydrogène (P) variables et (ii) les changements d'ordre chimique dans les alliages à base de Pt ayant lieu en présence d'hydrogène. Les résultats révèlent, à l'échelle atomique, la complexité des changements induits par les adsorbats.

Mots Clés

Effet du gaz environnant, métaux de transition, nanoparticules, catalyseurs, or, platine, DFT, thermodynamique, dynamique moléculaire ab-initio, énergie d'interface, énergie de ségrégation.